

**PROGRESS TOWARDS LEFT-HANDED ELECTROMAGNETIC
WAVES IN RARE-EARTH DOPED CRYSTALS**

by

Nicholas Riley Brewer

A dissertation submitted in partial fulfillment of
the requirements for the degree of

Doctor of Philosophy

(Physics)

at the

UNIVERSITY OF WISCONSIN–MADISON

2017

Date of final oral examination: July 7, 2017

The dissertation is approved by the following members of the Final Oral Committee:

Deniz D. Yavuz, Professor, Physics

James E. Lawler, Professor, Physics

Mark Saffman, Professor, Physics

Thad G. Walker, Professor, Physics

John C. Wright, Professor, Chemistry

© Copyright by Nicholas Riley Brewer 2017

All Rights Reserved

Dedicated to my parents and wife.

ACKNOWLEDGMENTS

Most importantly, I would like to thank Deniz Yavuz for his tremendous support throughout my time here. Deniz has been the superlative of advisors, with seemingly infinite patience and unending knowledge.

I would like to also thank Mark Saffman and Jim Lawler, for the experience I gained during the short periods I spent working in their labs. Thanks also to Betsy Den Hartog, who I worked with extensively in Jim Lawler's group, and especially Mike Wood. The short time I spent as his officemate was definitely memorable.

I have had the great fortune to work with excellent grad students throughout my time here. When I joined Yavuz Lab, I was lucky to have Josh Weber, Zach Simmons, and Jared Miles to show me the ropes. Josh taught me how to threshold test my first laser and align my first fiber, and has since been a great friend, softball teammate, and officemate. I had fun building up the experiment with Zach Simmons, and am excited to see the progress Zach Buckholtz makes in the next years. David Gold and Ben Lemberger have made for an interesting office environment and I have enjoyed working with them along with the other current members of Yavuz Lab: Eli Mueller, Josh Karpel, and Dipto Das

Many aspects of this research were only made possible by the help I received from other people in the department. Joe Sylvester, Steve Schumacher, and Sara Yaeger have been invaluable resources in the machine shop, Billy Gates was helpful in the electronics shop, and Chad Seys has been a champion IT guy. I would also like to thank Ann Austin, for dealing with all purchases extraordinarily quickly and efficiently, and Aimee and Renee Lefkow, for handling any and all administrative tasks.

I was a teaching assistant for several semesters and have enjoyed every minute of it. Jim Reardon has been an excellent supervisor; he is always willing to discuss questions and concerns and a conversation with him is never a dull one. I would also like to thank in particular Yibin Pan, Jeff Schmidt, Dan Thurs, and Peter Timbie for the experience I gained teaching with you. It is interesting and enlightening to see the techniques and strategies used by different professors.

I would like to thank my advisor from UW-Eau Claire, Jin Huang, for making sure I was well prepared for grad school. I would like also like to thank my high school teachers Jim Schultz and Jeff Crumbaugh, whose classes in biology, chemistry, and physics I remember well and were where I first considered a career in science.

The single biggest reason I have achieved what I have so far is the unwavering support of my parents, Tom and Nancy Brewer, not only throughout my time in Madison, but throughout my life. From a young age, they have instilled in me the value of education and the wonder of science, which has now culminated in me receiving a PhD. To this day, my parents are my most valuable resource, providing invaluable advice and offering support in every possible way.

Finally I'd like to thank Alyssa, I couldn't imagine a better wife and friend. It's been fun going through grad school together, from first arriving in Madison to finally writing our theses. Throughout the periods of high stress and low stress, she has been amazingly supportive and has made grad school so much more enjoyable. I'm excited to embark on our journey into the real world together.

TABLE OF CONTENTS

	Page
LIST OF FIGURES	vi
Abstract	ix
1 Negative Index of Refraction	4
1.1 Negative Index Materials	4
1.2 Challenges to Creating a Left-Handed Material	8
1.3 Applications of Negative Index Materials	10
1.3.1 Perfect Lens	10
1.3.2 Invisibility	12
2 Magnetic Response of $\text{Eu}^{3+}:\text{Y}_2\text{SiO}_5$ Crystal	13
2.1 Magnetic Response	13
2.2 $\text{Eu}^{3+}:\text{Y}_2\text{SiO}_5$ Crystal	15
2.3 Spectroscopy	16
2.4 Inhomogeneous and Homogeneous broadening of the ${}^7F_0 \rightarrow {}^5D_1$ Transition	22
2.5 Hyperfine Splitting of the 5D_1 Level	24
2.6 Magnetic Dipole Moment Calculation	25
2.7 Verification of ${}^7F_0 \rightarrow {}^5D_1$ Magnetic Character	28
3 Left-Handed Waves in a Material with External Polarization and Magnetization . .	30
3.1 External Polarization and Magnetization	30
3.2 Simulations	32
3.3 Implementation in an Atomic System	36
4 Experimental Setup	40
4.1 Laser Overview	40
4.2 Second Harmonic Generation	42
4.2.1 Phase Matching	42
4.2.2 Single Pass Results	45
4.3 Cavities	48

	Page
4.3.1 Linear Cavities	50
4.3.2 Ring Cavities	52
4.3.3 Impedance Matching and SHG Cavity Enhancement	55
4.3.4 Mode Matching	57
4.4 Cryostat	58
5 Rabi Flopping on a Magnetic Dipole Transition	59
5.1 Rabi Flopping	59
5.2 Procedure	60
5.3 Magnetic Dipole Moment	64
5.4 Simulations	65
5.5 Magnetization, Susceptibility, and Comments on Negative Index	69
5.5.1 Magnetization	69
5.5.2 Susceptibility	71
5.5.3 Left-Handed Waves	73
6 Future Improvements and Experiments	75
6.1 Spectral Hole Burning	75
6.2 Inhomogeneous Linewidth Suppression	80
6.2.1 Simulations	82
6.3 Electromagnetically Induced Transparency	85
7 Conclusion	87
REFERENCES	90
APPENDICES	
Appendix A: Second Harmonic Generation	96
Appendix B: Error Analysis	100
Appendix C: Numerically solving differential equations using a 4th order Runge-Kutta Method	104
Appendix D: Self-Heterodyne Method for Determining Laser Linewidth	109

LIST OF FIGURES

Figure	Page
1.1 <i>Permittivity and Permeability Phasors</i>	5
1.2 <i>Right-Handed Wave</i>	6
1.3 <i>Left-Handed Wave</i>	7
1.4 <i>Negative Refraction</i>	8
1.5 <i>Perfect Lens</i>	11
2.1 <i>Liquid Nitrogen Chamber</i>	17
2.2 <i>UV Diode Fluorescence Setup</i>	18
2.3 <i>Grating Spectrometer Spectrum Analysis</i>	19
2.4 <i>2D Eu^{3+} Spectrum</i>	20
2.5 <i>1D Eu^{3+} Spectrum</i>	21
2.6 <i>Fluorescence from 527.5 nm Excitation</i>	22
2.7 <i>Level Diagram</i>	23
2.8 <i>Inhomogeneous Linewidth</i>	24
2.9 <i>Fluorescence Decay</i>	25
2.10 <i>Magnetic Dipole Verification</i>	29
3.1 <i>Driven Left-Handed Wave</i>	32
3.2 <i>Left-Handed Wave Simulation With Initial Fields</i>	34

Figure	Page
3.3 <i>Left-Handed Wave Simulation With No Initial Fields</i>	35
3.4 <i>Refraction out of Externally Polarized and Magnetized Material</i>	37
3.5 <i>Generating \mathbf{M} and \mathbf{P} in an Atomic System</i>	38
4.1 <i>Laser Setup</i>	41
4.2 <i>Phase Matching</i>	43
4.3 <i>Quasi-Phase Matching</i>	45
4.4 <i>Expected Single Pass Efficiency</i>	46
4.5 <i>Measured Single Pass Efficiency</i>	47
4.6 <i>Temperature Dependence</i>	48
4.7 <i>Ray Matrices</i>	49
4.8 <i>Linear Cavity</i>	51
4.9 <i>Ring Cavity</i>	54
4.10 <i>Waists of Stable Ring Cavities</i>	54
4.11 <i>Ring Cavity Dimensions</i>	55
4.12 <i>Optimal Input Coupler Transmission</i>	56
5.1 <i>Alignment Scheme</i>	62
5.2 <i>Pulse Sequence</i>	63
5.3 <i>Rabi Oscillation Data</i>	64
5.4 <i>Rabi Flopping Simulation Energy Levels</i>	66
5.5 <i>Simulation Results</i>	69
5.6 <i>Susceptibility of Homogeneous Broadening</i>	71
5.7 <i>Magnetic Susceptibility</i>	72

Figure	Page
6.1 <i>Inhomogeneous Linewidth vs Homogeneous Linewidth</i>	75
6.2 <i>Simplified Spectral Hole Burning</i>	76
6.3 <i>All Possible Spectral Holes and Antiholes</i>	77
6.4 <i>Spectral Pit with Backburned Peak</i>	78
6.5 <i>Spectral Holes with Varying Burn Powers</i>	79
6.6 <i>Spectral Holes with Varying Burn Times</i>	79
6.7 <i>Backburned Peak Data</i>	80
6.8 <i>Inhomogeneous Linewidth Suppression Scheme Level Diagram</i>	81
6.9 <i>Suppression of Inhomogeneous Linewidth</i>	83
6.10 <i>Optimal Stark Laser Strength</i>	84
6.11 <i>Optimal k_S/k_P Ratio</i>	85
6.12 <i>EIT Laser Scheme</i>	86
B.1 <i>Photodiode Calibration Plot</i>	102
B.2 <i>Linearized Data</i>	102
D.1 <i>Self-Heterodyne Interferometer</i>	109
D.2 <i>Linewidth Measurements</i>	111

Abstract

Progress Towards Left-Handed Electromagnetic Waves in Rare-Earth Doped Crystals

Nicholas R. Brewer

Under the supervision of Professor Deniz D. Yavuz

At the University of Wisconsin - Madison

In 1968 Victor Veselago determined that a material with both a negative permittivity and negative permeability would have some extraordinary properties. The index of refraction of this material would be negative and light propagating inside would be ‘left-handed’. This research went relatively unnoticed until the year 2000 when John Pendry discovered that a lens with an index of refraction of $n = -1$ could, in principle, have infinite resolution. Since 2000, research into negative index materials has exploded. The challenging part of this research is to get a material to respond to magnetic fields at optical frequencies. Artificially created metamaterials are able to achieve this and have been the focus of most negative index research. The long term goal of our project is to produce left-handed light in an atomic system. In order to do this, an atomic transition needs to be utilized that is magnetic dipole in character. Pure magnetic dipole transitions in the optical regime are more rare and fundamentally much weaker than the electric dipole transitions typically used in atomic physics experiments. They can be found, however, in the complex atomic structure of rare-earth elements. The ${}^7F_0 \rightarrow {}^5D_1$ transition in europium doped yttrium orthosilicate ($\text{Eu}^{3+}:\text{Y}_2\text{SiO}_5$) has a wavelength of 527.5 nm and is a pure magnetic dipole transition. We measured its dipole moment to be $(0.063 \pm 0.005)\mu_B$ via Rabi oscillations, inferring a magnetization on the order of 10^{-2} A/m. Demonstrating this large magnetic response at an optical frequency is a major first step in realizing left-handed light in atomic systems.

Introduction

The velocity of transverse undulations in our hypothetical medium, calculated from the electro-magnetic experiments of MM. Kohlrausch and Weber, agrees so exactly with the velocity of light calculated from the optical experiments of M. Fizeau, that we can scarcely avoid the inference that light consists in the transverse undulations of the same medium which is the cause of electric and magnetic phenomena.

–James Clerk Maxwell

On Physical Lines of Force (1862)

Although light consists of both an oscillating electric- and magnetic-field, at visible wavelengths typically only the electric field is considered in atomic physics experiments. The reason for this is that the magnetic response of atoms is fundamentally weaker than the electric response. A very large magnetic dipole moment and a high density of atoms is needed in order to get an appreciable magnetic response. If this can be achieved, however, it is possible to create a negative index of refraction and left-handed light. The goal of this thesis is to show a strong response from a magnetic dipole transition at an optical frequency.

Negative index of refraction is the most interesting concept in all of science and I hope to convey that through this thesis. Negative index materials, the properties of left-handed light, and the experimental challenges involved are discussed in chapter 1. The momentum of light propagating inside a negative index material can point in the opposite direction of propagation resulting in bizarre effects like a reversed doppler shift and radiation ‘tension’ rather than radiation pressure. Applications of negative index materials include the possibility of constructing a ‘perfect lens’ with limitless resolution and also being able to create an invisibility cloak. Currently though, negative refraction has only been demonstrated in artificial metamaterials. Experiments have approached the optical region of the spectrum, but are limited by the scale that the so-called split ring resonators that comprise the metamaterials can be fabricated. In order to push negative index experiments to shorter and shorter wavelengths, it is necessary to use smaller and smaller resonators that interact

strongly with both the electric and magnetic fields of light. In the visible region of the spectrum, an obvious choice of resonator is an atom. There are many challenges with using atoms, however, the most notable being a lack of suitable magnetic dipole transitions.

It turns out that the open $4f$ electron shell of rare-earth elements is home to exotic atomic structure where magnetic dipole transitions at visible wavelengths can be found. Chapter 2 discusses why magnetic dipole transitions are weaker than comparable electric dipole transitions, introduces the ${}^7F_0 \rightarrow {}^5D_1$ transition in europium doped yttrium orthosilicate (YSO), and presents spectroscopy results. A three-meter grating spectrometer was used to identify the transition and the results were compared to what was found in the 1990s. The inhomogeneous and homogeneous linewidths were determined from scanning a weak probe beam over the transition and measuring the fluorescence decay, respectively. The electron levels in the $4f$ shell of europium deviate from pure LS coupling and can be expressed as a linear combination of pure LS states. These ‘mixing coefficients’ were calculated in the 1960s and can be used to predict the magnetic dipole moment of the ${}^7F_0 \rightarrow {}^5D_1$ transition. Lastly, the magnetic nature of this transition was confirmed by studying the intensity of fluorescence at different angles of incidence. It was found that the fluorescence intensity only varies with a change in magnetic field orientation, and not with a change in electric field orientation, confirming that the transition is interacting with the magnetic field of light.

Although creating a conventional negative index of refraction is still a monumental task, chapter 3 details a new scheme for creating left-handed light in an atomic system. It turns out that left-handed waves can be generated in a material if a separate magnetization and polarization drive the wave. The magnetization and polarization must have the correct phase relationship and amplitude ratio to create left handed light, but a negative permeability isn’t necessary. One dimensional simulations were carried out and the resulting electromagnetic waves are shown to be left-handed. Next refraction was simulated and it is shown that the wavevectors’ directions are consistent with refraction out of a negative index material. Next an idea of how this scheme could be implemented in europium is shown. A magnetization generated using the ${}^7F_0 \rightarrow {}^5D_1$ transition could be combined with a polarization created from the nonlinear response of the host crystal.

A detailed description of the experimental setup is given in chapter 4. The laser system, cryostat, and various other electronic components are discussed. An external cavity diode laser at a wavelength of 1055 nm is Pound-Drever-Hall locked to an ultra-low-expansion glass cavity. It is then amplified to several watts and frequency doubled using a bow-tie cavity with a periodically poled KTP nonlinear crystal inside. The resulting green light is sent through AOMs in order to precisely control the timing of the pulses shined on the YSO crystal. The YSO crystal is housed in a liquid helium cryostat in order to suppress phonon vibrations. All of the electronics (RF generators, oscilloscopes, cryostat temperature controller) are controlled via GPIB and serial cables with Matlab programs.

Once this experimental setup was built, Rabi flopping was observed for the first time on a magnetic dipole transition at an optical frequency. These results, accompanying simulations, and significance for future work are detailed in chapter 5. A strong Rabi beam of various lengths was shined into the YSO crystal and the transmission of a weak probe beam was detected with a photon counter. The transmission of the probe is seen to oscillate depending on the length of the Rabi beam. The frequency of the oscillation depends on the intensity of the Rabi beam and a frequency vs intensity plot can be fitted to determine the dipole moment of the transition. This dipole moment was then used to run simulations to infer the off-diagonal density matrix elements, which correspond to the amount of magnetization produced. It is found that with the magnetization produced in this experiment, hundreds of nanowatts of left-handed light could be produced using the scheme outlined in chapter 3.

Improvements and short term future experiments are discussed in chapter 6. A description of spectral hole burning is given and preliminary experiments are shown, including spectral hole width dependences on pulse length and power, and backburning a peak in order to produce a single class of ion. A possibility of narrowing the inhomogeneous linewidth is also discussed. This involves using the stark shift to compensate for the shifts in each atom's transition throughout the inhomogeneous wavelength. Finally, a brief description of electromagnetically induced transparency (EIT) is given. Performing EIT in the YSO crystal would allow future slow and stopped light experiments to take place.

Chapter 1

Negative Index of Refraction

1.1 Negative Index Materials

The permittivity, ϵ , and permeability, μ , of a material characterize how the material responds to electric fields and magnetic fields, are complex in the general case, and usually have positive real parts. In 1968 Veselago proposed a theoretical material in which the real parts of the permittivity and permeability would both be negative [1]. A material with $\epsilon < 0$ and $\mu < 0$ is referred to as either a left-handed material or a negative index material. The index of refraction of a material is given by $n = \sqrt{\epsilon\mu}$ and at first glance it seems that the negative signs cancel and have no consequence. By writing out the permittivity and permeability in complex notation, however, it becomes clear why the negative sign is used:

$$\epsilon = \epsilon_r e^{i\phi} \quad (1.1)$$

$$\mu = \mu_r e^{i\theta} \quad (1.2)$$

$$n = \sqrt{\epsilon_r \mu_r} e^{i(\phi+\theta)/2} . \quad (1.3)$$

Here it helps to draw out the phasors for ϵ and μ in the complex plane (see figure 1.1). From this it can be seen that if the real parts of ϵ and μ are negative, then

$$\frac{\pi}{2} < \frac{\phi + \theta}{2} < \pi \quad (1.4)$$

and when the real part of n is taken, it must be less than one:

$$\text{Re}[n] = \sqrt{\epsilon_r \mu_r} \cos \frac{\phi + \theta}{2} < 0 . \quad (1.5)$$

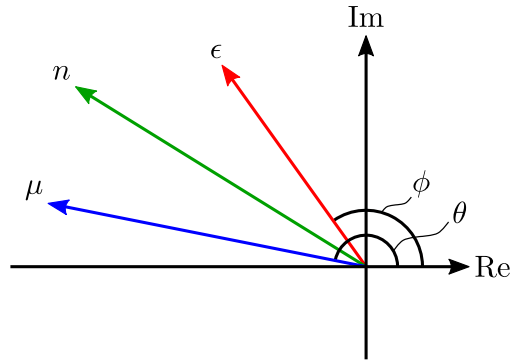


Figure 1.1: *Permittivity and Permeability Phasors*. Phasor diagram illustrating why the negative sign must be used when ϵ and μ have negative real parts. The imaginary part of ϵ or μ correspond to absorptions and, in the case of passive materials, must be positive.

In order to see the consequences of having a negative permittivity and permeability, Maxwell's equations, where ϵ and μ appear independently, must be used. The following outline of left-handed light will closely follow the arguments made by Veselago in ref [1]. Lets assume the plane wave solution in order to simplify the situation. The two curl Maxwell equations,

$$\nabla \times \mathbf{E} = -\frac{\partial \mathbf{B}}{\partial t} \quad (1.6a)$$

$$\nabla \times \mathbf{H} = \frac{\partial \mathbf{D}}{\partial t}, \quad (1.6b)$$

become for plane waves

$$\mathbf{k} \times \mathbf{E} = \mu\omega\mathbf{H} \quad (1.7a)$$

$$\mathbf{k} \times \mathbf{H} = -\epsilon\omega\mathbf{E}. \quad (1.7b)$$

From equations 1.7, the orientation between the electric field \mathbf{E} , magnetic field \mathbf{B} , and wavevector \mathbf{k} is

$$\hat{\mathbf{E}} \times \hat{\mathbf{H}} = \hat{\mathbf{k}} \quad (1.8)$$

and therefore the wave is described as right-handed. If the signs of ϵ and μ are switched, however,

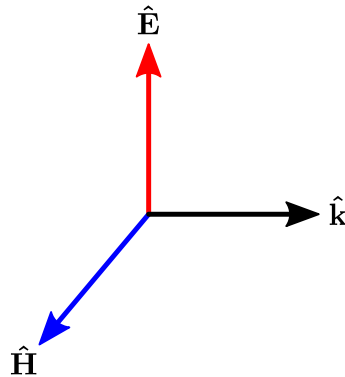


Figure 1.2: *Right-Handed Wave*. Relative directions of the electric field, magnetic field, and wavevector in a right-handed wave.

the equations become

$$\mathbf{k} \times \mathbf{E} = -\mu\omega\mathbf{H} \quad (1.9a)$$

$$\mathbf{k} \times \mathbf{H} = \epsilon\omega\mathbf{E} \quad (1.9b)$$

and therefore the electric field, magnetic field, and wavevector form a left-handed triad:

$$\hat{\mathbf{E}} \times \hat{\mathbf{H}} = -\hat{\mathbf{k}}. \quad (1.10)$$

From this we can see that the wavevector $\hat{\mathbf{k}}$, and therefore the momentum of the wave, points in the opposite direction as the energy flow defined by the Poynting vector, $\mathbf{S} = \mathbf{E} \times \mathbf{H}$. The fact that momentum and energy flow point in opposite directions cause light traveling in a left-handed medium to have some very strange and interesting properties.

One interesting property is that the Doppler shift is reversed; an object moving away from an observer will appear to be blue shifted instead of redshifted and vice versa. Another oddity is that the cone of Cherenkov radiation is emitted behind a moving charged particle instead of in front of it. Lastly, the radiation pressure an object feels in a left-handed medium is reversed resulting instead in a radiation ‘tension’.

Maybe the easiest way to observe that a material has a negative index is by looking at refraction into the negative index material. Negative refraction is one of the most apparent consequence of

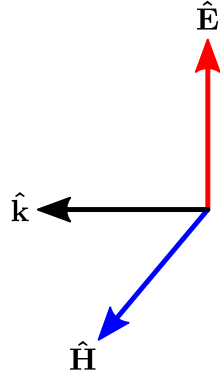


Figure 1.3: *Left-Handed Wave*. Relative directions of the electric field, magnetic field, and wavevector in a left-handed wave.

having a left-handed material. The reason for negative refraction can be seen by looking at the boundary conditions for electric and magnetic fields at the interface between two dielectrics:

$$E_{\parallel 1} = E_{\parallel 2} \quad (1.11a)$$

$$\epsilon_1 E_{\perp 1} = \epsilon_2 E_{\perp 2} \quad (1.11b)$$

$$H_{\parallel 1} = H_{\parallel 2} \quad (1.11c)$$

$$\mu_1 H_{\perp 1} = \mu_2 H_{\perp 2} . \quad (1.11d)$$

A left-handed medium will have a negative value of ϵ and μ , and therefore the signs of the electric field and magnetic field in the second and fourth boundary conditions in equation 1.11 will be flipped. This results in negative refraction as shown in figure 1.4. Snell's law, $n_1 \sin \theta_1 = n_2 \sin \theta_2$, can be used normally when dealing with negative index materials. If either index is negative, the negative sign must be included in calculations.

Fresnel coefficients are important and interesting to consider when dealing with refraction from one medium to another. For light that has a polarization perpendicular to the the plane of incidence, the transmission coefficient is [2]

$$\frac{E_t}{E_i} = \frac{2(n_i/\mu_i) \cos \theta_i}{(n_i/\mu_i) \cos \theta_i + (n_t/\mu_t) \sqrt{1 - (n_i^2/n_t^2) \sin^2 \theta_i}} \quad (1.12)$$

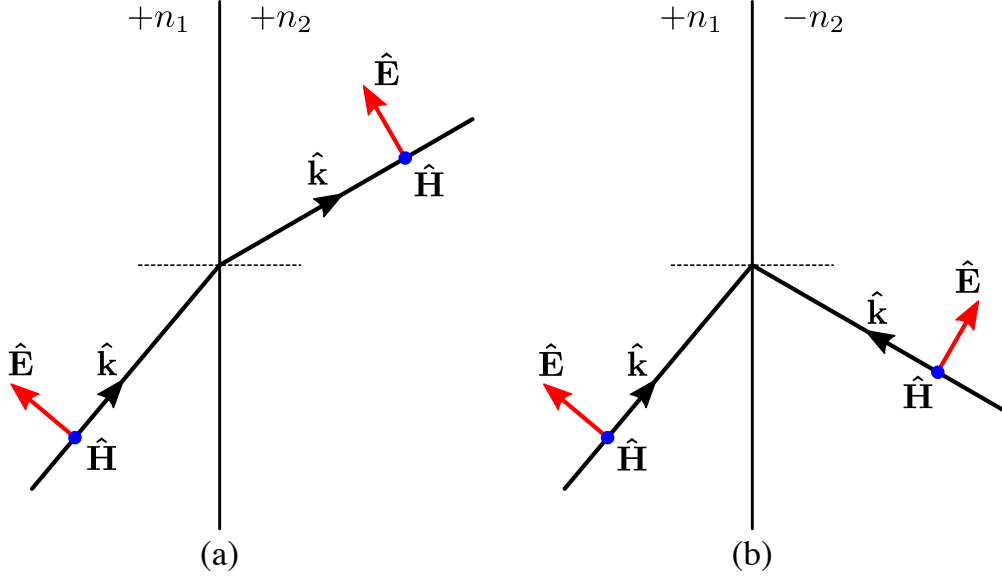


Figure 1.4: *Negative Refraction*. (a) Regular refraction from a positive index to a positive index. (b) Refraction from a positive index to a negative index.

and the reflection coefficient is

$$\frac{E_r}{E_i} = \frac{(n_i/\mu_i) \cos \theta_i - (n_t/\mu_t) \sqrt{1 - (n_i^2/n_t^2) \sin^2 \theta_i}}{(n_i/\mu_i) \cos \theta_i + (n_t/\mu_t) \sqrt{1 - (n_i^2/n_t^2) \sin^2 \theta_i}}. \quad (1.13)$$

These formulas are applicable to positive refraction but also negative refraction if the absolute value of n_i , n_t , ϵ_i , ϵ_t , μ_i , and μ_t are used. Ordinarily the permeabilities divide out because it is assumed that $\mu \approx \mu_0$. One remarkable thing is that when $\mu = -\mu_0$, the reflection coefficient goes to zero and all of the light is transmitted into the negative index medium.

1.2 Challenges to Creating a Left-Handed Material

One limitation to having a simultaneously negative permittivity and permeability is that there must be frequency dependence. One of the clearest arguments for this can be seen by looking at the energy density. For constant values of ϵ and μ the energy density is given by

$$u = \epsilon E^2 + \mu H^2, \quad (1.14)$$

where if ϵ and μ are negative the energy density will be negative. The more general equation for energy density is actually

$$u = \frac{\partial(\epsilon\omega)}{\partial\omega} E^2 + \frac{\partial(\mu\omega)}{\partial\omega} H^2, \quad (1.15)$$

which allows both ϵ and μ to be negative as long as the derivatives $\frac{\partial(\epsilon\omega)}{\partial\omega}$ and $\frac{\partial(\mu\omega)}{\partial\omega}$ remain positive [2].

It is not out of the ordinary for a material to have a negative permittivity. Metals, for example, experience a negative permittivity for frequencies lower than their plasma frequency [3]. A large magnetic response at optical frequencies, however, has not been observed naturally so far. The reason for this is that the magnetic response from atoms is fundamentally much weaker than the electric response. One way to compare these two is to look at the ratio of electric susceptibility to magnetic susceptibility. Susceptibility is a measure of how much a material is affected by the presence of an external electric/magnetic field. The quantum mechanical formulas for electric and magnetic susceptibility are:

$$\chi_E = \frac{N d_{ED}^2}{\epsilon_0 \hbar (\Delta\omega - i\frac{\Gamma}{2})} \quad (1.16)$$

$$\chi_M = \frac{N \mu_0 \mu_{MD}^2}{\hbar (\Delta\omega - i\frac{\Gamma}{2})}. \quad (1.17)$$

The ratio of electric to magnetic susceptibility is then:

$$\frac{\chi_E}{\chi_M} = \frac{d_{ED}^2}{\epsilon_0 \mu_0 \mu_{MD}^2} = \left(\frac{e a_0}{\mu_B / c} \right)^2 = \frac{4}{\alpha^2} \approx 10^5, \quad (1.18)$$

where e is the elementary charge, a_0 is the Bohr radius, μ_B is the Bohr magneton, c is the speed of light, and α is the fine structure constant ($\sim \frac{1}{137}$). This is explained further in chapter 2, but shows that all else being equal, it is 100,000 times easier to modify the electric susceptibility than the magnetic susceptibility. The susceptibilities are related to the permittivity and permeability by

$$\epsilon = 1 + \chi_E \quad (1.19a)$$

$$\mu = 1 + \chi_M. \quad (1.19b)$$

In free space $\chi_E = \chi_M = 0$, so $\epsilon = \mu = 1$ and $n = 1$. In a material the values of ϵ and μ are modified from their free space values by their respective susceptibilities. Therefore it is much

easier to modify the permittivity than the permeability because it is much easier to get a large value of χ_E .

In 1999 John Pendry proposed that a structure he called a split ring resonator could be used to create a large magnetic response [4]. This device has an inductance and capacitance that are coupled together so that an oscillating electric field would induce a magnetic field, therefore causing a large magnetic susceptibility to be created. These split ring resonators need to be fabricated small enough that their length scale is smaller than the wavelength of light intended to experience the large change in μ . These artificially created materials are called metamaterials and have become a large area of research over the last two decades. The challenge is to create split ring resonators on a smaller and smaller length scale so that ϵ and μ can be modified at higher and higher frequencies. On top of the challenge of creating a smaller split ring resonator, these devices are created out of metal and therefore are subject to Ohmic losses, i.e. the tiny currents flowing in the material are dissipated by the resistance of the metal.

An alternative approach to creating a material with a negative index would be to find an atom that has both a strong electric transition and magnetic transition at the same frequencies. Several schemes for producing a negative index in an atomic system have been proposed [5][6][7][8]. This is difficult for the same reason mentioned earlier: magnetic transitions are much weaker than electric transitions. This thesis will identify and show a coherent electromagnetic interaction with a magnetic dipole transition in the optical region of the spectrum.

1.3 Applications of Negative Index Materials

1.3.1 Perfect Lens

Veselago's paper didn't garner much attention until Pendry discovered in 2000 that a material with an index of $n = -1$ could produce a lens with unlimited resolution [9]. Veselago had predicted that a flat plate of material with $n = -1$ would act as an unconventional lens, as seen in figure 1.5. Just using Snell's law and geometric optics it is easy to see how an image can form in this situation.

Pendry had shown though that the situation was more remarkable than the geometric picture. He showed that a slab of negative index material could act as a 'perfect lens' and actually amplify

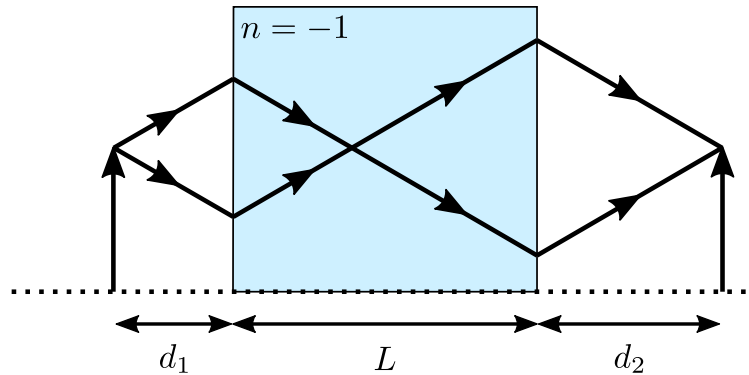


Figure 1.5: *Perfect Lens*. In order to image an object with a slab of negative index material, it must be the case that $L = d_1 + d_2$.

evanescent waves, therefore reproducing subwavelength features in the image. Since then there has been enormous growth in the field of negative index materials, mostly in the context of metamaterials. The first metamaterial experiments were done with microwaves using split ring resonators, as described in section 1.2 [10][11][12]. The use of split ring resonators has even begun to approach the optical regime of the spectrum, where a negative permeability has been achieved for 3000 nm light [13]. Negative refraction has been demonstrated at visible wavelengths of 660 nm and 780 nm in a bulk metamaterial consisting of silver nanowires, however, the phase velocity remained positive, meaning it was not a ‘left-handed’ material [14]. Additionally, only TM-polarized light experienced negative refraction, while the TE-polarized light experienced positive refraction.

The first experiments to demonstrate a superior lensing effect were done with a ‘transmission line’ lens, consisting of a series of capacitors and inductors, at 1.057 GHz [15]. Perfect lensing in the optical region of the spectrum has yet to be achieved. However a certain class of devices, dubbed a ‘poor man’s superlens’ by Pendry, has been able to demonstrate sub-diffraction-imaging in the near-field without relying on a negative index. In these experiments, surface plasmon excitation can recover evanescent waves and has been demonstrated by using thin layers of silver as a ‘superlens’ [16].

1.3.2 Invisibility

In 2006 Pendry and Leonhardt independently published papers that described a way to construct an invisibility cloak using what is now called ‘transformation optics’ [17][18]. In some cases a negative index is needed to achieve cloaking. Since 2006 there have been several demonstrations of cloaking in the microwave and optical domains. The first demonstration was a 2D cloak of a copper cylinder using microwaves at 8.5 GHz [19]. The cloak, a structure consisting cylindrical arrays of split ring resonators, significantly decreased backscatter and forward scatter, although absorption caused imperfect concealment. At optical frequencies, a ‘carpet cloak’ has been demonstrated for 1400 - 1800 nm light by drilling sub-wavelength holes in a silicon wafer in order to modify the effective index of refraction [20]. This technique allows for broadband cloaking because resonant elements are not employed, however, losses arise from technical limitations of fabrication.

Chapter 2

Magnetic Response of $\text{Eu}^{3+}:\text{Y}_2\text{SiO}_5$ Crystal

2.1 Magnetic Response

What sets the goal of this thesis apart from the majority of research focused on negative index materials, is that our plan is to create a negative index of refraction in an atomic system. In order to achieve this, as stated in the previous chapter, an atomic transition with a strong, pure, magnetic dipole moment is needed. Because of this, it is instructive and interesting to look at the difference between electric and magnetic dipole transitions quantum mechanically. This discussion will follow closely with the discussion provided in Woodgate [21].

When the perturbation $H' = \frac{e}{m} \mathbf{A} \cdot \mathbf{p}$ is used and after the rotating wave approximation is applied, the transition rate is found to have a dependence on the square of the matrix element,

$$\left| \langle j | \frac{e}{m} \hat{\mathbf{e}} \cdot \mathbf{p} e^{i\mathbf{k}\cdot\mathbf{r}} | i \rangle \right|^2, \quad (2.1)$$

where $\hat{\mathbf{e}}$ is the polarization direction and \mathbf{p} is the momentum of the electron. This matrix element determines selection rules and can be expanded in order to determine the contribution of each electromagnetic multipole. The spatial scale of the electromagnetic wave is given by the exponential in eq 2.1 and can be expanded as

$$e^{i\mathbf{k}\cdot\mathbf{r}} = 1 + i\mathbf{k} \cdot \mathbf{r} + \dots \quad (2.2)$$

If the amplitude of light is approximately constant over the size of the atom, all terms but the first term can be thrown out. Along with this, if the polarization is along the x -component of motion equation 2.1 simplifies to

$$\left| \langle j | \frac{e}{m} p_x | i \rangle \right|^2, \quad (2.3)$$

where $p = m\dot{x}$ and the following can be used:

$$\langle j|m\dot{x}|i\rangle = \frac{im}{\hbar}\langle j|H_0x - xH_0|i\rangle = im\frac{E_j - E_i}{\hbar}\langle j|x|i\rangle. \quad (2.4)$$

Finally by using $\omega_{ji} = \frac{E_j - E_i}{\hbar}$ and plugging this into equation 2.3, what is left is

$$|i\omega_{ji}\langle j|ex|i\rangle|^2 = \omega_{ji}^2 e^2 |\langle j|x|i\rangle|^2. \quad (2.5)$$

Equation 2.5 is proportional to the electric dipole transition strength and will be used later to compare to the magnetic contribution.

The second term in the exponential expansion (equation 2.2) is needed to describe magnetic dipole radiation. In this case it will be assumed that \mathbf{k} is in the x -direction and \mathbf{p} is in the y -direction. If only this second term is used, equation 2.1 turns into

$$\left| \langle j | \frac{e}{m} p_y (i k_x x) | i \rangle \right|^2, \quad (2.6)$$

where $k_x = \frac{\omega_{ji}}{c}$. Because p_y and x commute, equation 2.6 can be written as

$$\frac{\omega_{ji}^2}{c^2} \left| \langle j | \frac{e}{m} x p_y | i \rangle \right|^2 \quad (2.7)$$

and $x p_y$ can be rewritten as

$$x p_y = \frac{1}{2}(x p_y - p_x y) + \frac{1}{2}(x p_y + p_x y) \quad (2.8)$$

$$x p_y = \frac{1}{2}\hbar l_z + \frac{1}{2}m(x\dot{y} + \dot{x}y). \quad (2.9)$$

If only the first term of equation 2.9 is plugged into equation 2.7 the result is

$$\frac{\omega_{ji}^2}{c^2} \left| \langle j | \frac{e\hbar}{2m} l_z | i \rangle \right|^2, \quad (2.10)$$

where $\frac{e\hbar}{2m} l_z$ is the z component of the magnetic dipole moment of the orbital part of the atom. Because of this, this contribution from the second term in equation 2.2 is referred to as the magnetic dipole moment of the transition. The quantity $\frac{e\hbar}{2m}$ is the Bohr magneton, μ_B and is the atomic unit of magnetic dipole transition strength. In section 2.6, the dipole moment is calculated using

equation 2.10 with an a spin term added in. The second term of equation 2.9 results in the electric quadrupole moment, but will not be further described here.

The integrals that need to be evaluated in equations 2.5 and 2.10 correspond to how overlapped the ground and excited state wavefunctions are. In order to make an accurate comparison between electric and magnetic dipole transitions, it should be assumed that these integrals evaluate to the same value and each transition has the same frequency ω . The ratio of the electric dipole transition strength to magnetic dipole transition strength is then

$$\begin{aligned} \frac{\text{Electric Dipole Transition Strength}}{\text{Magnetic Dipole Transition Strength}} &= \frac{\omega_{ji}^2 e^2 |\langle j|x|i\rangle|^2}{\frac{\omega_{ji}^2}{c^2} |\langle j|\frac{e\hbar}{2m} l_z|i\rangle|^2} \\ &= \frac{e^2 a_0^2}{\mu_B^2 / c^2} \\ &= \frac{4}{\alpha^2}. \end{aligned} \quad (2.11)$$

This quantum mechanical discussion is a more in depth explanation of the origin of the dipole moment values mentioned earlier in equation 1.18.

2.2 $\text{Eu}^{3+}:\text{Y}_2\text{SiO}_5$ Crystal

Other than being purely magnetic, there are several other qualities that guided the search for a suitable transition and atomic system. Even a magnetic dipole transition that is on the order of a Bohr magneton will be 100,000 times weaker than any equivalent electric dipole transition, so it is necessary to have a high density in order to get a strong response. Another requirement is a relatively narrow homogeneous linewidth. The reason for this is that the wider the homogeneous linewidth, the more laser power is needed to observe Rabi oscillations. Lastly, the inhomogeneous broadening should be as narrow as possible so that the effective density isn't too low. In the ideal case there would be no inhomogeneous broadening and the laser would be exactly resonant with every atom in its path.

Considering all the requirements listed above, a rare-earth doped crystal was determined to be a great system to work in for several reasons. First and most importantly, the open $4f$ electron

configuration provides an exotic environment home to elaborate atomic structure, consequently giving rise to some magnetic dipole transitions in the optical region of the spectrum. Spectroscopic studies of the intensity and polarization of fluorescence of rare-earth elements have been conducted many decades ago and several magnetic dipole transitions were identified [22][23][24]. In 1993 Shen and Kachu performed a detailed spectroscopic study on a magnetic dipole transition that will be the focus of most of this thesis: the ${}^7F_0 \rightarrow {}^5D_1$ transition in europium doped yttrium orthosilicate ($\text{Eu}^{3+}:\text{Y}_2\text{SiO}_5$) [25]. In rare-earth elements, the $5s$ and $5p$ filled shells are spatially more spread out than the $4f$ shell [26]. This helps shield the $4f$ electrons from the environment. The nuclei in yttrium orthosilicate (YSO) have small or zero magnetic moments therefore not contributing to homogeneous broadening [27]. Because the atoms are embedded in a crystal, there is no doppler broadening or atomic diffusion. There is however strain broadening that is caused by each atom experiencing a slightly different electric field in the crystal. As shown later, this inhomogeneous broadening was measured to be 1.6 GHz at 4.5 K. A doped crystal also provides a higher density than an ultracold cloud or hot vapor. YSO is also a well known host crystal; many experiments have been done on the ${}^7F_0 \rightarrow {}^5D_0$ forced electric dipole transition in YSO to find a good host for quantum memory experiments [28][29]. Fortunately for us, in the process of building and performing this experiment, another group had shown that the ${}^7F_0 \rightarrow {}^5D_1$ transition in europium is excited purely by the magnetic field of an incident laser (although a different host crystal was used) [30]. Because this is such a critical aspect of the experiment, even with this recent result, we conducted our own experiment to verify the magnetic nature of this transition, outlined in section 2.7.

2.3 Spectroscopy

After the ${}^7F_0 \rightarrow {}^5D_1$ transition in Eu:YSO was identified as a good candidate for possible negative index experiments, a crystal was purchased from Scientific Materials located in Bozeman, Montana and preliminary spectroscopy experiments were done.

The first attempt at measuring the ${}^7F_0 \rightarrow {}^5D_1$ transition involved trying to broaden a mode locked laser with a photonic crystal fiber. The idea was to broaden the spectrum of the laser into the visible, shine it through the crystal, and use an optical spectrum analyzer to see absorption

around 527.5 nm to pinpoint what wavelength the transition was at. The photonic crystal fiber proved very difficult to work with and no absorption around 527.5 nm was definitively seen.

The next idea was to try a fluorescence experiment similar to reference [23]. A UV LED was used to excite the europium ions up to higher states. The resulting fluorescence was sent through a small grating spectrometer. Again the line of interest was never observed. Most rare-earth doped crystal experiments take place at cryogenic temperatures to freeze out phonon modes that broaden the transitions. As a first attempt at this, a small vacuum chamber (figure 2.1 and 2.2) was built with the capability of freezing the crystal to liquid nitrogen temperatures.



Figure 2.1: *Liquid Nitrogen Chamber*. This chamber was used to cool the crystal to liquid nitrogen temperatures and to do the initial spectroscopic measurements on our YSO crystal. A roughing pump was hooked up to the thin pipe with the KF flange and liquid nitrogen was poured into the larger diameter pipe on the top. The viewport provided optical axis to the crystal.

After a few attempts with the small grating spectrometer, more alternatives were sought out. Mike Wood, a grad student in Jim Lawler's group, had built a 3 meter echelle grating spectrometer in order to measure branching fractions in iron-group elements by observing fluorescence from

glow discharges [31]. Mike generously offered to help out and in the end the ${}^7F_0 \rightarrow {}^5D_1$ line was successfully observed. Right as this experiment was carried out, Shen's paper titled ${}^7F_0 \rightarrow {}^5D_1$ *Transition in $\text{Eu}^{3+}:\text{Y}_2\text{SiO}_5$* was serendipitously discovered.

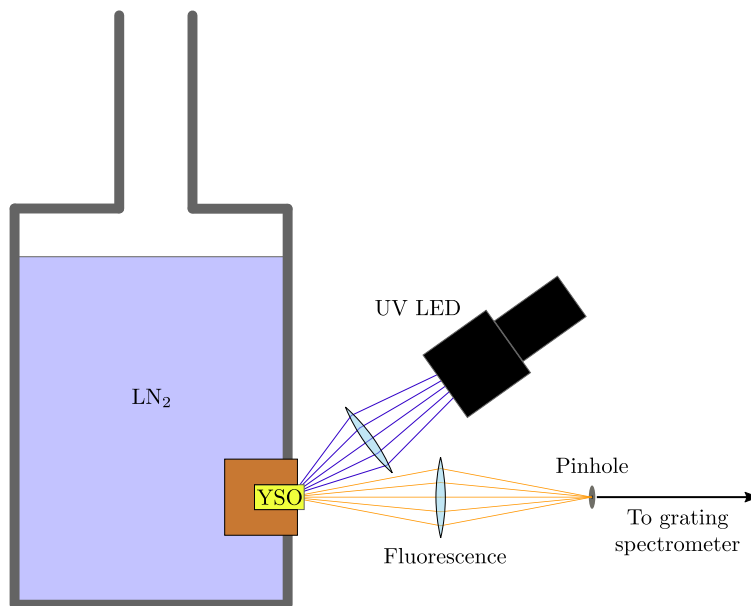


Figure 2.2: *UV Diode Fluorescence Setup*. Setup to collect the fluorescence from the Eu:YSO crystal. The crystal was held in a copper mount that was in contact with a liquid nitrogen reservoir. The whole thing was placed in the vacuum can shown in figure 2.1. The UV LED was shined on the crystal off axis and the fluorescence was captured with a lens, focused through a pinhole, and sent to a spectrometer.

A more complete description of how Mike's spectrometer works can be found in references [31] and [32], but a brief description will be provided here. The purpose of the echelle grating is to observe higher diffraction orders in order to gain more resolution. A consequence of this though is that the orders overlap each other. For this reason, a prism is used separate the orders in the orthogonal direction. The 2D spectrum is recorded on a CCD.

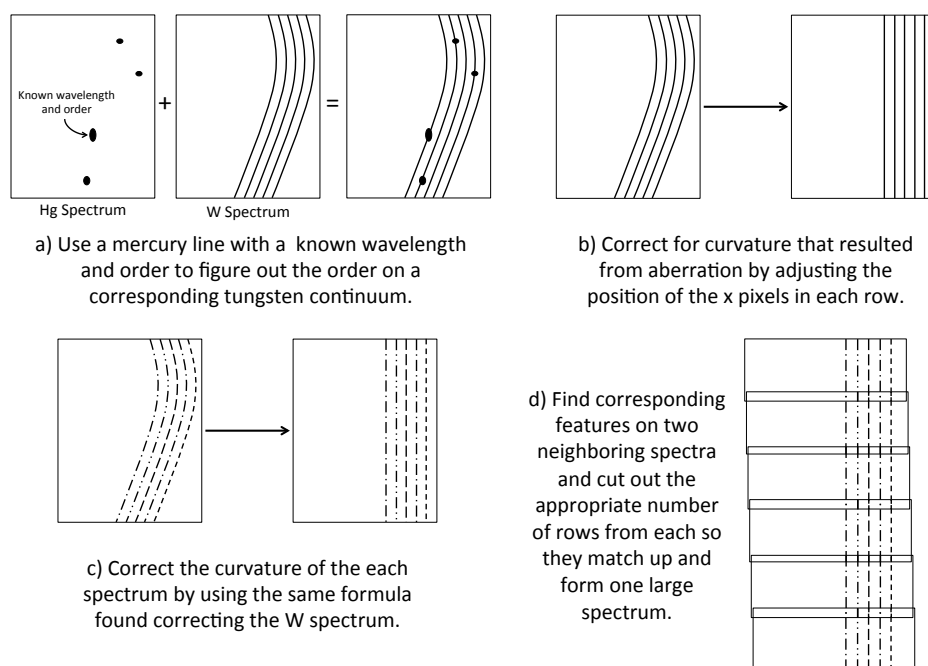


Figure 2.3: *Grating Spectrometer Spectrum Analysis*. Three spectra needed to be taken to properly analyze the raw CCD data: a mercury lamp spectrum, a tungsten lamp spectrum, and the spectrum for the actual YSO crystal. Mike used a mercury lamp to calibrate his data and could identify the wavelength and order number of a certain green mercury line. The tungsten lamp's spectrum is a continuum in the visible region and can be used to correct aberrations. (a) The mercury and tungsten spectra were overlaid. Because the order of the mercury reference line was known, every order in the tungsten continuum could be identified. (b) Next the curvature was corrected by following one order over the range of y -pixels and plotting how far off the center the order was compared to the center y -pixel. An empirical fit was made to this plot and the best fit equation was used to adjust the x -position of every row. Because the grating order is much longer than the CCD frame, six frames had to be taken to capture an entire order. (c) The curvature correction was done to each of the six frames. (d) After all of the spectra were straightened out, they were stitched together into one long spectrum by finding a line that occurred in the region of overlap between adjacent frames. Excess rows of one of the frames were cut out so that the frames matched up to form a continuous spectrum.

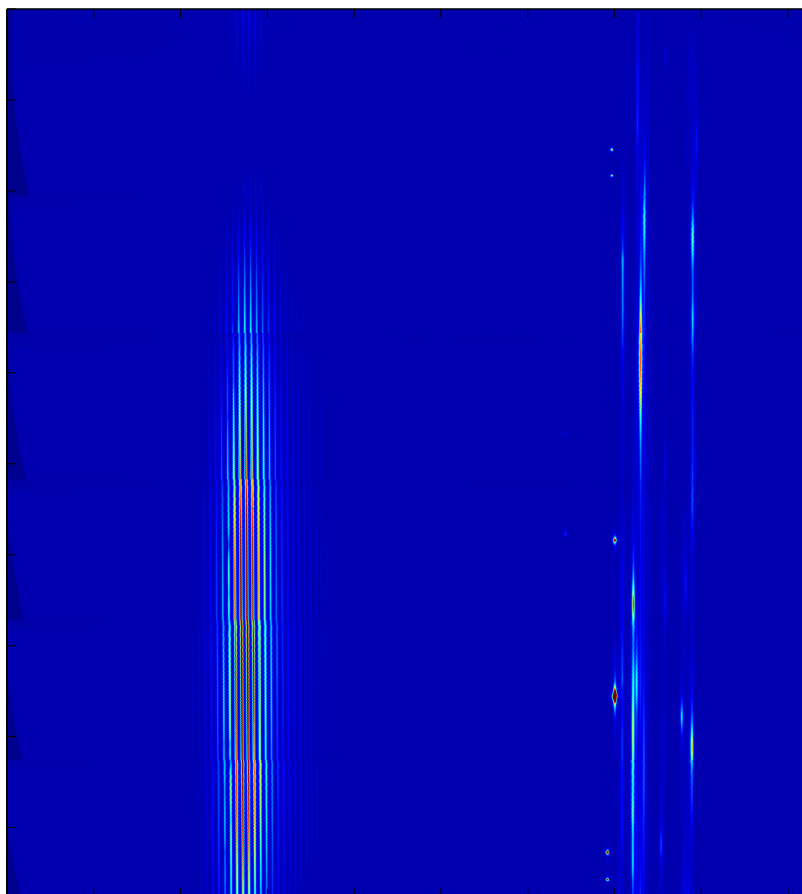


Figure 2.4: $2D Eu^{3+}$ Spectrum. Final 2D spectrum after being processed in Matlab. The continuum on the left is the UV light used to pump the crystal. The grouping of lines on the right half of the spectrum are the visible lines from the europium ions. The x dimension corresponds to grating order, each vertical strip being a different order. The y dimension corresponds to wavelength.

Considerable work had to be done in Matlab to manipulate the raw data into something useable. Both programs we wrote and Mike wrote were used in analyzing the data. An overview of how the raw data was processed is shown in figure 2.3 and the processed 2D europium spectrum is shown in figure 2.4.

The purpose of using the spectrometer was to see the ${}^7F_0 \rightarrow {}^5D_1$ transition. After the final 2D spectrum was constructed, the wavelength of any given x - and y -pixel could be determined.

Because the wavelength of each pixel is known, it was possible to make a one dimensional plot of intensity vs wavelength (figure 2.5).

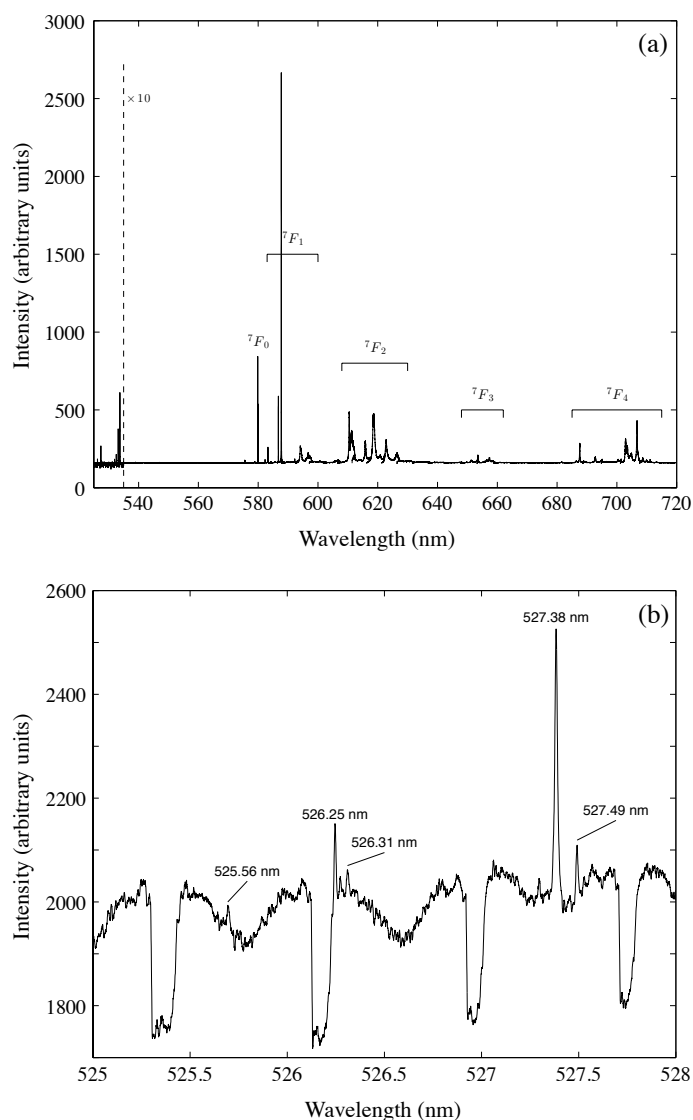


Figure 2.5: $1D \text{Eu}^{3+}$ Spectrum. (a) Complete 1D spectrum from created from the 2D spectrum (figure 2.4) over all wavelengths. (b) Just the ${}^7F_0 \rightarrow {}^5D_1$ magnetic dipole transition. All of the labeled wavelengths are part of the same transition. There are two inequivalent crystal sites and three M_J levels for each. Only five of these six possible transitions were able to be resolved.

Figure 2.5 can be compared to what is found by Shen and Kachru [25]. A few things are noteworthy. First, there is no fluorescence at all from 540 nm to 560 nm in figure 2.5(a), whereas there is a large portion of intense fluorescence in Shen’s data, which is taken at 8 K. Another thing is that the peaks of the ${}^7F_0 \rightarrow {}^5D_1$ transition in our paper are shifted by 0.15 nm compared to what Shen reports. The spacings between different stark levels and sites, however, are the same. Our suspicion is that there is a systematic error in our data.

2.4 Inhomogeneous and Homogeneous broadening of the ${}^7F_0 \rightarrow {}^5D_1$ Transition

When laser light with a wavelength of 527.5 nm is shined on the cryogenically cooled crystal, the fluorescence is orange, as seen in figure 2.6. This can be explained by looking at the level diagram for ‘site 2’ in Eu:YSO, shown in figure 2.7. The atoms in the 5D_1 level quickly decay via phonon processes down to the 5D_0 level, which in turn optically decay to the 7F manifold. Any atoms in the 7F manifold quickly decay to the 7F_0 level via phonon processes (see ref [33] for more details).



Figure 2.6: *Fluorescence from 527.5 nm Excitation.* Fluorescence from shining 527.5 nm laser through the crystal while it is cooled to liquid helium temperatures. In this picture the green laser is traveling from left to right. As the beam gets further into the crystal the profile tapers off as a result of absorption.

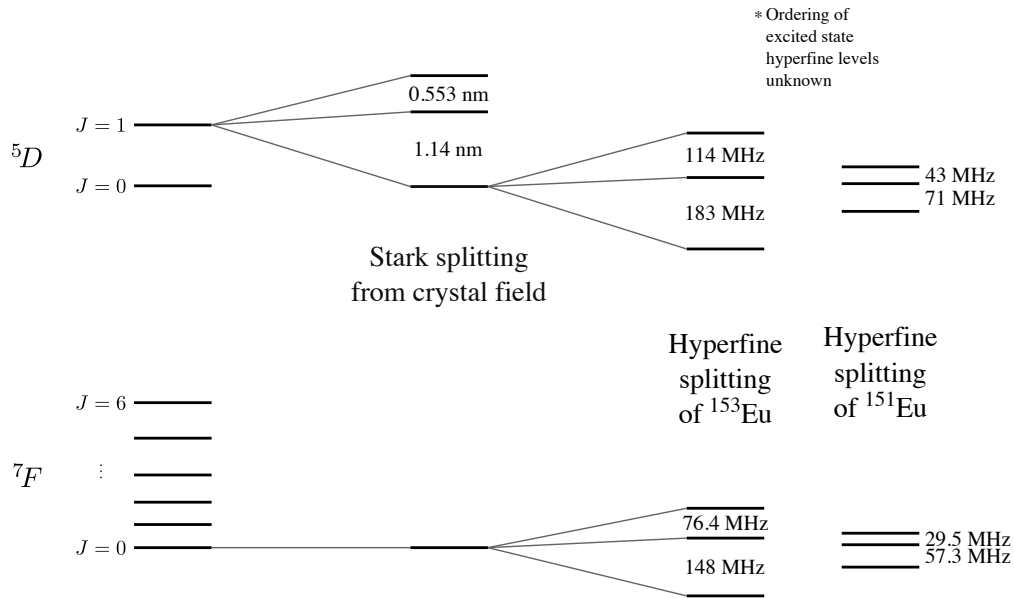


Figure 2.7: *Level Diagram*. Levels of Eu^{3+} in site 2 of Y_2SiO_5 . The levels of site 1 are shifted to a up by 0.104 nm.

Once the laser system described in chapter 4 was built, it was determined that the wavelength of the ${}^7F_0 \rightarrow {}^5D_1$ transitions did in fact match what Shen and Kachru had measured, meaning that our data from figure 2.5 was systematically shifted by about 0.15 nm. When a weak probe beam is scanned over the transition, an inhomogeneous linewidth of 1.6 GHz is seen (figure 2.8). In order to determine the homogeneous linewidth, a lifetime measurement can be made. Both the lifetime, T_1 , and dephasing time, T_2 , need to be taken into account to calculate the homogeneous linewidth of the transition. In order to measure the lifetime, a very short pulse of green light was shined on the laser and the orange fluorescence was measured in time. This data is shown in figure 2.9. Because the dominant decay from the 5D_1 level is through phonon decay to the 5D_0 level, the risetime of this orange fluorescence corresponds to the lifetime of the 5D_1 level. The slow decay of the orange fluorescence is directly measuring the lifetime of the 5D_0 level. A fit to the data in figure 2.9 gives a risetime of $33 \mu\text{s}$ and an exponential decay of 1.6 ms. If the 5D_1 is assumed to be predominantly lifetime broadened, the linewidth of the transition would be

$$\frac{1}{\tau} = \frac{1}{33 \mu\text{s}} = 2\pi \cdot 4.8 \text{ kHz} . \quad (2.12)$$

Shen measures the dephasing time to be $T_2 = 56 \mu\text{s}$, which would contribute to the homogeneous line:

$$\frac{1}{\tau} = \frac{1}{33 \mu\text{s}} + \frac{1}{2 \cdot 56 \mu\text{s}} = 2\pi \cdot 6.2 \text{ kHz} . \quad (2.13)$$

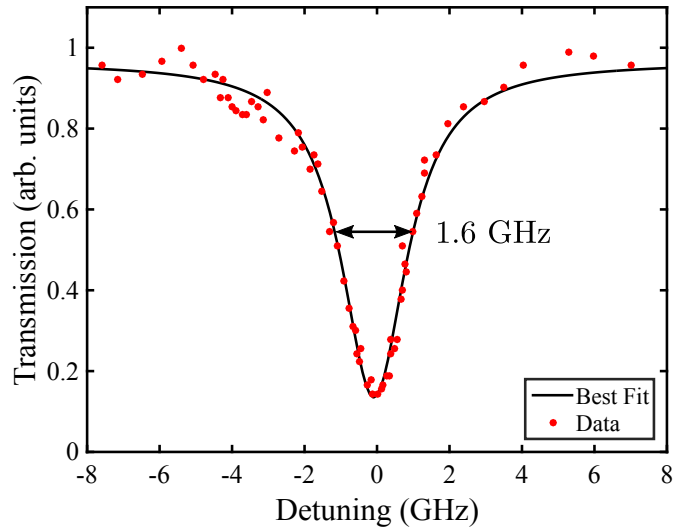


Figure 2.8: *Inhomogeneous Linewidth*. Inhomogeneous linewidth between the 7F_0 level and the lower M_J level of the 5D_1 level. The transmission at the center of the line is 14%. The inhomogeneous line is actually Lorentzian and not gaussian, as mentioned in [34] and explained in [35] and [36].

2.5 Hyperfine Splitting of the 5D_1 Level

On top of the stark splittings from the crystal field, there is also hyperfine structure that isn't resolved in the data shown in figure 2.5. The natural abundance of europium is 52.2% Eu-153 and 47.8% Eu-151. Ideally the experiment would be done in an isotopically pure sample so that there is no confusion over the levels that the laser is interacting with and also because of the fact that the effective density would be twice as large. Both isotopes have a nuclear spin of $5/2$. In this system the interaction between the crystal field and the europium ion is much stronger than the interaction between the nuclear magnetic moment and electron magnetic moment. Therefore, instead of using

the basis $|J, I, F, M_F\rangle$, the good quantum numbers are $|J, M_J, I, M_I\rangle$. Because of this, the M_J level is broken up into three M_I levels: $\pm|\frac{5}{2}\rangle, \pm|\frac{3}{2}\rangle, \pm|\frac{1}{2}\rangle$.

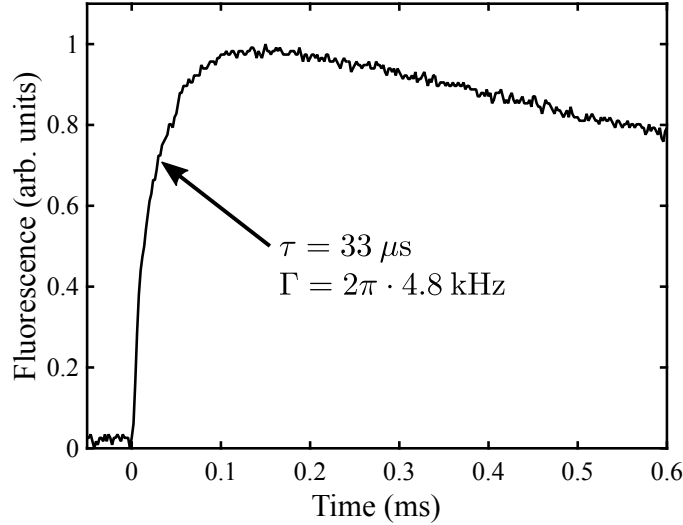


Figure 2.9: *Fluorescence Decay*. The homogeneous linewidth between the 7F_0 level and the lower M_J level of the 5D_1 level can be determined by looking at the fluorescence in time. The rise in fluorescence corresponds to phonon decay to the 5D_0 level. The slower exponential decay corresponds to radiative decay from the 5D_0 level.

The hyperfine structure of both Eu-153 and Eu-151 is shown in figure 2.7. Since the hyperfine splittings are on the order of tens to hundreds of megahertz and the inhomogeneous linewidth is on the order of a gigahertz, the hyperfine structure is not resolvable unless spectral hole burning techniques are used (discussed in chapter 6).

2.6 Magnetic Dipole Moment Calculation

The levels of the open $4f^6$ electron configuration deviate the pure LS states because the electrons are in the intermediate coupling regime. The relevant levels in europium, for example are:

$${}^7F_0 = 0.9680|{}^7F_0\rangle + 0.0016|{}^5D_0\rangle + 0.1659|{}^5D'_0\rangle - 0.1815|{}^5D''_0\rangle \quad (2.14)$$

$${}^5D_1 = -0.2096|{}^7F_1\rangle - 0.2066|{}^5D_1\rangle + 0.7162|{}^5D'_1\rangle - 0.5561|{}^5D''_1\rangle. \quad (2.15)$$

These mixing coefficients are calculated in reference [37] and also explained more in [38]. The primes (' and ') indicated seniority number, which arise from the fact that there are multiple ways to add the electrons together to get a single LS term (the 5D_0 and 5D_1 levels in this case).

In order to calculate the magnetic dipole moment of the ${}^7F_0 \rightarrow {}^5D_1$ transition, the magnetic dipole operator must be used:

$$\hat{\mu} = -\mu_B \sum_i l_i + g s_i, \quad (2.16)$$

where $g \approx 2$ and is the electron g -factor. The sum is over all of the participating electrons and becomes

$$\begin{aligned} \hat{\mu} &= -\mu_B(L + gS) \\ \hat{\mu} &= -\mu_B(J + (g - 1)S), \end{aligned} \quad (2.17)$$

where $J = L + S$ is used in the second line. The magnetic dipole moment can be calculated by evaluating

$$\begin{aligned} \mu &= -\mu_B \langle {}^7F_0 | (J + (g - 1)S) | {}^5D_1 \rangle \\ \mu &= -\mu_B \langle {}^7F_0 | (J + S) | {}^5D_1 \rangle. \end{aligned} \quad (2.18)$$

To use equation 2.18 to calculate the dipole moment of the transition, first the reduced matrix element must be found and then the Wigner-Eckart theorem must be employed. The fact that there are no radial integrals simplifies the math and the reduced matrix elements can be “easily evaluated” [39] using

$$\begin{aligned} \langle LSJ || J + S || L'S'J' \rangle &= \delta_{LSJ,L'S'J'} \sqrt{[J(J + 1)(2J + 1)]} \\ &\quad + \delta_{LS,L'S'} (-1)^{L+S+J+1} \sqrt{(2J + 1)(2J' + 1)} \\ &\quad \times \begin{Bmatrix} L & S & J \\ 1 & J' & S \end{Bmatrix} \sqrt{[S(S + 1)(2S + 1)]}, \end{aligned} \quad (2.19)$$

where L , S , and J are the quantum numbers of the ground state and L' , S' , and J' are the quantum numbers of the excited state. In the LS basis, the magnetic dipole selection rules are $\Delta J = 0, \pm 1$ except $J = 0 \rightarrow J = 0$ and if $\Delta S = 0$, then $\Delta L = 0$. Only levels with the same

seniority number have a nonzero matrix element. The value of the of the reduced matrix element for the ${}^7F_0 \rightarrow {}^5D_1$ transition is

$$\begin{aligned}
\langle {}^7F_0 || J + S || {}^5D_1 \rangle &= (0.9680)(-0.2096) \langle {}^7F_0 || J + S || {}^7F_1 \rangle \\
&+ (0.0016)(-0.2066) \langle {}^5D_0 || J + S || {}^5D_1 \rangle \\
&+ (0.1659)(0.7162) \langle {}^5D'_0 || J + S || {}^5D'_1 \rangle \\
&+ (-0.1815)(-0.5561) \langle {}^5D''_0 || J + S || {}^5D''_1 \rangle \\
\langle {}^7F_0 || J + S || {}^5D_1 \rangle &= -0.1654.
\end{aligned} \tag{2.20}$$

This calculation is also done in reference [40] and agrees with what is shown here. After the reduced matrix element is determined, the matrix element of the transition can be calculated using the Wigner-Eckart theorem [39]:

$$\langle \alpha J M_J | T_q^{(k)} | \alpha' J' M'_J \rangle = (-1)^{J-M_J} \begin{pmatrix} J & k & J' \\ -M_J & q & M'_J \end{pmatrix} \langle \alpha J || T^{(k)} || \alpha' J' \rangle, \tag{2.21}$$

where k is the rank of the tensor operator, q is the orientation of the coordinate system, M and M' are the magnetic quantum number of the ground and excited states, respectively, and α and α' are all other non-angular momentum quantum numbers of the ground and excited states, respectively. The Wigner-Eckart theorem, in words, says that the matrix element of a tensor operator is found by multiplying something that that only depends on the angular momentum orientation (the 3-j symbol) with something that describes what is physically going on independent of orientation (the reduced matrix element).

In this case $k = 1$ because the magnetic dipole operator is a vector (a rank 1 tensor), linearly polarized light is used corresponding to $q = 0$, and the magnetic quantum number of each level is $M_J = M'_J = 0$. Using the Wigner-Eckart theorem, the matrix element of the ${}^7F_0 \rightarrow {}^5D_1$ transition

can be found:

$$\begin{aligned}
\mu &= -\mu_{\text{B}} \langle {}^7F_0 | (J + S) | {}^5D_1 \rangle \\
&= -\mu_{\text{B}} (-1)^{J-M_J} \begin{pmatrix} J & k & J' \\ -M_J & q & M'_J \end{pmatrix} \langle {}^7F_0 || T^{(k)} || {}^5D_1 \rangle \\
&= -\mu_{\text{B}} (-1)^{0-0} \begin{pmatrix} 0 & 1 & 1 \\ 0 & 0 & 0 \end{pmatrix} \langle {}^7F_0 || J + S || {}^5D_1 \rangle \\
&= -\mu_{\text{B}} \left(-\frac{1}{\sqrt{3}} \right) (-0.1654) \\
&= -0.0955\mu_{\text{B}} .
\end{aligned} \tag{2.22}$$

This is therefore the dipole moment that should be measured when a Rabi flopping experiment is performed on the ${}^7F_0 \rightarrow {}^5D_1$ transition. Chapter 5 will detail the experiment and compare this calculated dipole moment with what was experimentally found.

2.7 Verification of ${}^7F_0 \rightarrow {}^5D_1$ Magnetic Character

It was recently definitively shown that the ${}^7F_0 \rightarrow {}^5D_1$ transition in Eu^{3+} was excited via a magnetic field [30]. This experiment, however, was carried out using $\text{Eu}:\text{Y}_2\text{O}_3$ nanoparticles. Our experiment takes place in a different host crystal, so we would like to independently confirm this. Our crystal is macroscopic and it isn't possible to use the same method used in [30] involving tightly focusing azimuthally polarized light. Instead the dependence of fluorescence on angle of incidence was measured. This experiment depends on the fact that the crystal is anisotropic and has some preferred direction. If light incident on the crystal is polarized in the way shown in the upper left diagram of figure 2.10, and the crystal is rotated around the axis as indicated, the orientation of the magnetic field changes with respect to the optical axes, while the electric field orientation remains unchanged. For the configuration shown in the upper right of figure 2.10 just the opposite occurs; the electric field orientation with respect to the optical axes changes and the magnetic field orientation remains constant. During the experiment the fluorescence is monitored along an orthogonal direction to the plane of incidence.

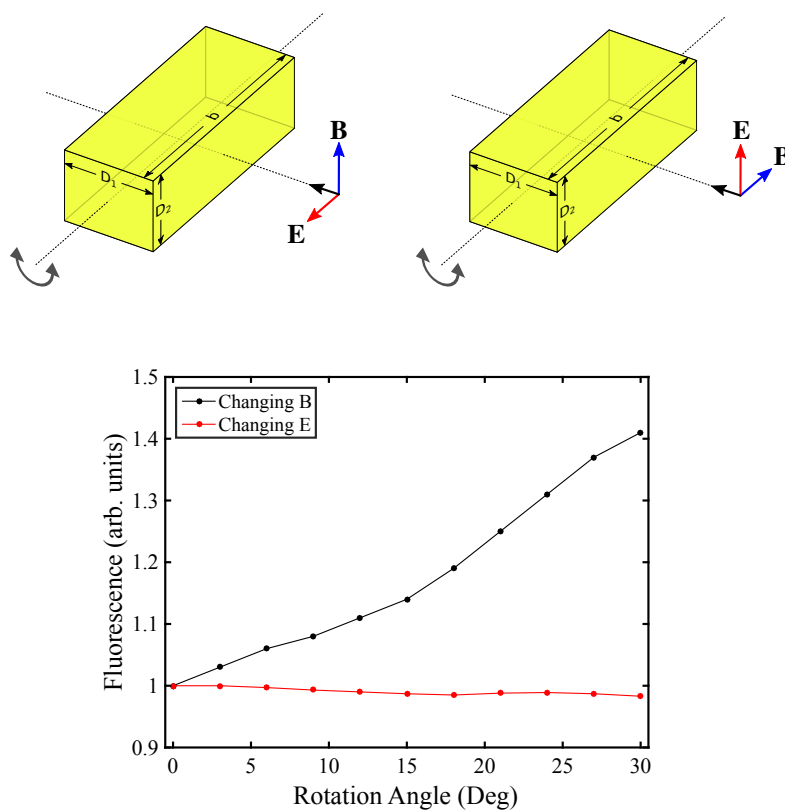


Figure 2.10: *Magnetic Dipole Verification*. The crystal orientation and light polarization in the upper left corresponds to the B -field orientation changing direction with respect to the crystal axes and the upper right corresponds to the E -field orientation changing direction with respect to the crystal axes. The fluorescence data is shown in the plot. The black line shows how the fluorescence changes with changing B -field and the red line shows how the fluorescence changes with changing E -field.

It was found that when the magnetic field orientation changes with respect to the optical axes there is a large change in fluorescence, and when the electric field changes with respect to the crystal axes, there is a negligible change in fluorescence. This experiment was carried out for every combination of crystal orientation, rotation angle, and laser polarization and similar results were found. This suggests that the magnetic field of light is responsible for the excitation, meaning the ${}^7F_0 \rightarrow {}^5D_1$ transition is, in fact, a magnetic dipole transition.

Chapter 3

Left-Handed Waves in a Material with External Polarization and Magnetization

3.1 External Polarization and Magnetization

Most of the research done on left-handed materials depends on the material having a permittivity and permeability with a certain frequency response for which the incident wave has simultaneously negative values for both. This is difficult to achieve in atomic systems for reasons described in chapters 1 and 2: the magnetic dipole moment of a transition is fundamentally many orders of magnitude smaller than the electric dipole moment of the transition and consequently, a large density of magnetic oscillators are needed to compensate for the lack of response.

As an alternative to these conventional methods for producing a negative index material, our group proposed a new scheme for generating left-handed waves in a material [41]. This new scheme basically involves combining two separate driving fields, via a magnetization and polarization, in a way such that left-handed waves are created. To illustrate this, it is necessary to rewrite equations 1.7 instead as

$$\mathbf{k} \times \mathbf{E} = \mu_0 \omega (\mathbf{H} + \mathbf{M}_{\text{ext}}) \quad (3.1a)$$

$$\mathbf{k} \times \mathbf{H} = -\omega (\epsilon \mathbf{E} + \mathbf{P}_{\text{ext}}). \quad (3.1b)$$

The subscript “ext” is there to emphasize that the polarization \mathbf{P} and magnetization \mathbf{M} are produced from separate external fields distinguished from the incident field that we wish to make left-handed. Let’s assume that an incident wave exists with fields \mathbf{E}_0 and \mathbf{H}_0 . The material has some permittivity ϵ but it’s assumed any induced magnetization does not substantially modify the

permeability, so $\mu = \mu_0$. The goal is to flip the signs on the righthand side of equations 3.1 and mimic a material that has $\epsilon = -\epsilon_0$ and $\mu = -\mu_0$. In order for this to be the case, the following must occur:

$$\epsilon \mathbf{E}_0 + \mathbf{P}_{\text{ext}} = -\epsilon_0 \mathbf{E}_0 \quad (3.2a)$$

$$\mathbf{P}_{\text{ext}} = -\epsilon \mathbf{E}_0 - \epsilon_0 \mathbf{E}_0 \quad (3.2b)$$

$$\mathbf{P}_{\text{ext}} = -\epsilon_0 \mathbf{E}_0 (n^2 + 1) \quad (3.2c)$$

and

$$\mathbf{H}_0 + \mathbf{M}_{\text{ext}} = -\mathbf{H}_0 \quad (3.3a)$$

$$\mathbf{M}_{\text{ext}} = -2\mathbf{H}_0. \quad (3.3b)$$

where in equations 3.2, $\epsilon = \epsilon_0 n^2$ is used. When these conditions for \mathbf{P} and \mathbf{M} are plugged into equations 3.1, the result is

$$\mathbf{k} \times \mathbf{E} = -\mu_0 \omega \mathbf{H} \quad (3.4a)$$

$$\mathbf{k} \times \mathbf{H} = \epsilon_0 \omega \mathbf{E}, \quad (3.4b)$$

which is equivalent to equations 1.7 in the case that $\mu = -\mu_0$ and $\epsilon = -\epsilon_0$. In this case the \mathbf{E} , \mathbf{H} , and \mathbf{k} vectors form a left-handed triad just like described in section 1.1. The relative orientations of each field are shown in figure 3.1. Another important thing to consider is the ratio between the magnitude of polarization and magnetization:

$$\begin{aligned} \frac{\mathbf{P}_{\text{ext}}}{\mathbf{M}_{\text{ext}}} &= \frac{-\epsilon_0 \mathbf{E}_0 (n^2 + 1)}{-2\mathbf{H}_0} \\ &= \frac{\epsilon_0}{2} (n^2 + 1) \sqrt{\frac{\mu_0}{\epsilon_0}} \frac{1}{n} \\ &= \frac{(n^2 + 1)}{2cn}, \end{aligned} \quad (3.5)$$

where the fact that $\frac{E_0}{H_0} = \sqrt{\frac{\mu}{\epsilon}} = \sqrt{\frac{\mu_0}{\epsilon_0 n^2}}$ in a material is used.

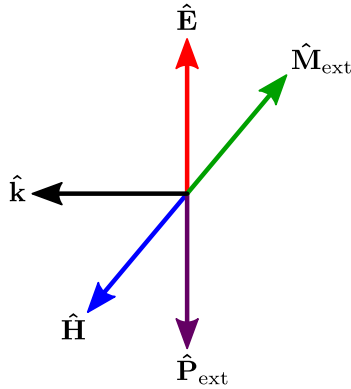


Figure 3.1: *Driven Left-Handed Wave*. Directions of the \mathbf{E} , \mathbf{H} , \mathbf{P} , \mathbf{M} , and \mathbf{k} vectors in our proposed scheme for creating left-handed waves.

3.2 Simulations

Maxwell's equations (equations 3.6) were simulated using finite difference methods very similar to the ones described in reference [42]. This method numerically solves Maxwell's equations using no approximations.

$$\nabla \times \mathbf{E} = -\frac{\partial \mathbf{B}}{\partial t} \quad (3.6a)$$

$$\nabla \times \mathbf{B} = \mu_0 \mathbf{J} + \mu_0 \epsilon_0 \frac{\partial \mathbf{E}}{\partial t} \quad (3.6b)$$

$$\nabla \cdot \mathbf{E} = \frac{\rho}{\epsilon_0} \quad (3.6c)$$

$$\nabla \cdot \mathbf{B} = 0. \quad (3.6d)$$

When the wave is traveling through a material, it is also true that

$$\mathbf{D} = \epsilon_0 \mathbf{E} + \mathbf{P} \quad (3.7a)$$

$$\mathbf{B} = \mu_0 (\mathbf{H} + \mathbf{M}), \quad (3.7b)$$

where \mathbf{P} is the polarization and \mathbf{M} is the magnetization. With these definitions and no source terms ($\rho = \mathbf{J} = 0$), the curl Maxwell equations become:

$$\nabla \times \mathbf{E} = -\frac{\partial \mathbf{B}}{\partial t} \quad (3.8a)$$

$$\nabla \times \mathbf{H} = \frac{\partial \mathbf{D}}{\partial t}. \quad (3.8b)$$

These equations written out explicitly are:

$$-\frac{\partial B_x}{\partial t} = \frac{\partial E_z}{\partial y} - \frac{\partial E_y}{\partial z} \quad (3.9a)$$

$$\frac{\partial B_y}{\partial t} = \frac{\partial E_z}{\partial x} - \frac{\partial E_x}{\partial z} \quad (3.9b)$$

$$-\frac{\partial B_z}{\partial t} = \frac{\partial E_y}{\partial x} - \frac{\partial E_x}{\partial y} \quad (3.9c)$$

$$\frac{\partial D_x}{\partial t} = \frac{\partial H_z}{\partial y} - \frac{\partial H_y}{\partial z} \quad (3.9d)$$

$$-\frac{\partial D_y}{\partial t} = \frac{\partial H_z}{\partial x} - \frac{\partial H_x}{\partial z} \quad (3.9e)$$

$$\frac{\partial D_z}{\partial t} = \frac{\partial H_y}{\partial x} - \frac{\partial H_x}{\partial y}. \quad (3.9f)$$

These simulations only include transverse electric (TE) waves. This means that $E_x = E_y = 0$ so there is only an electric field perpendicular to the plane of incidence. Also $H_z = 0$, so there is only a magnetic field in the plane of incidence. With these conditions only the following equations from 3.9 remain:

$$\frac{\partial B_x}{\partial t} = -\frac{\partial E_z}{\partial y} \quad (3.10a)$$

$$\frac{\partial B_y}{\partial t} = \frac{\partial E_z}{\partial x} \quad (3.10b)$$

$$\frac{\partial D_z}{\partial t} = \frac{\partial H_y}{\partial x} - \frac{\partial H_x}{\partial y} \quad (3.10c)$$

In order to solve these numerically, Matlab's gradient function was used on the spatial part and a Runge-Kutta method was used on the time part (see appendix C).

Two interesting cases that were explored are shown in figures 3.2 and 3.3. The first is the case of inducing \mathbf{P}_{ext} and \mathbf{M}_{ext} when the incident electromagnetic field is present in the initial conditions. The wave that propagates is left-handed since $(\hat{\mathbf{E}} \times \hat{\mathbf{H}} = -\hat{\mathbf{k}})$. In each case the direction of \mathbf{P} and \mathbf{M} are shown in the lower right. The quantity that is graphed is the total electric field, i.e. any initial electric field plus the electric field created by the polarization and magnetization. An oscillating polarization and/or magnetization will in other cases produce an electromagnetic wave (that is the basis of second harmonic generation, sum frequency generation, etc). With the proper amplitude and phase though, discussed in section 3.1, the polarization and magnetization act to create a region that is left-handed where electromagnetic waves propagate such that $\hat{\mathbf{E}} \times \hat{\mathbf{H}} = -\hat{\mathbf{k}}$.

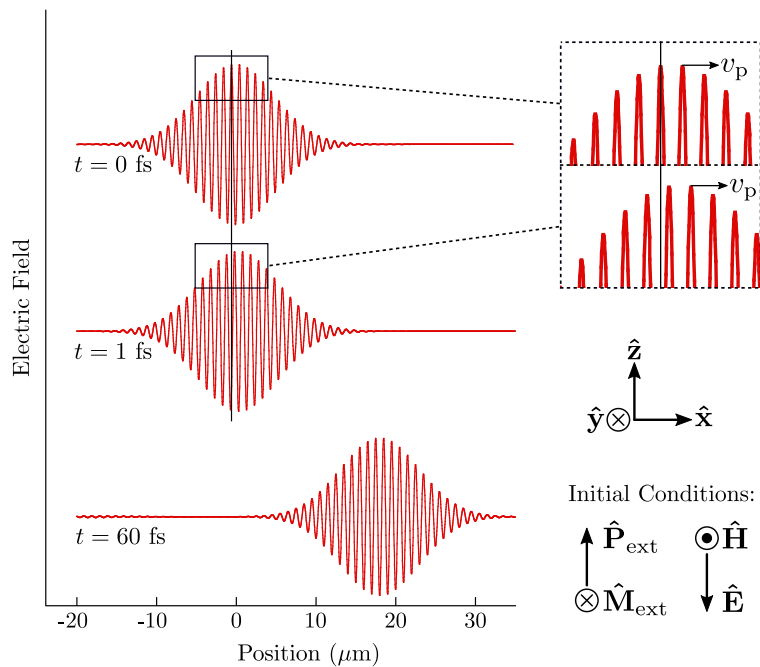


Figure 3.2: *Left-Handed Wave Simulation With Initial Fields*. When the external polarization and magnetization have the correct amplitude and phase relation to an existing electromagnetic wave, the wave becomes left handed and propagates as shown. The plots show the value of the electric field at 0, 1, and 60 femtoseconds. Between 0 and 1 femtosecond it can be seen that the phase advances to the left, as shown in the dashed boxes. The direction of the phase velocity and the wave vector $\hat{\mathbf{k}}$ point in the same direction. Since $\hat{\mathbf{E}} \times \hat{\mathbf{H}}$ points in the opposite direction of $\hat{\mathbf{k}}$, the propagating wave is left-handed.

An interesting thing to note is that in conventional left-handed waves the group velocity and phase velocity point in opposite directions (although not always [43]). The flow of power still points in the direction of $\hat{\mathbf{E}} \times \hat{\mathbf{H}}$ while the momentum points in the opposite direction ($\hat{\mathbf{E}} \times \hat{\mathbf{H}} = -\hat{\mathbf{k}}$). In the simulations shown, the polarization and magnetization are external and effectively create a packet of left-handed material that travels through space. The electromagnetic wave inside this packet of polarization and magnetization is then left-handed.

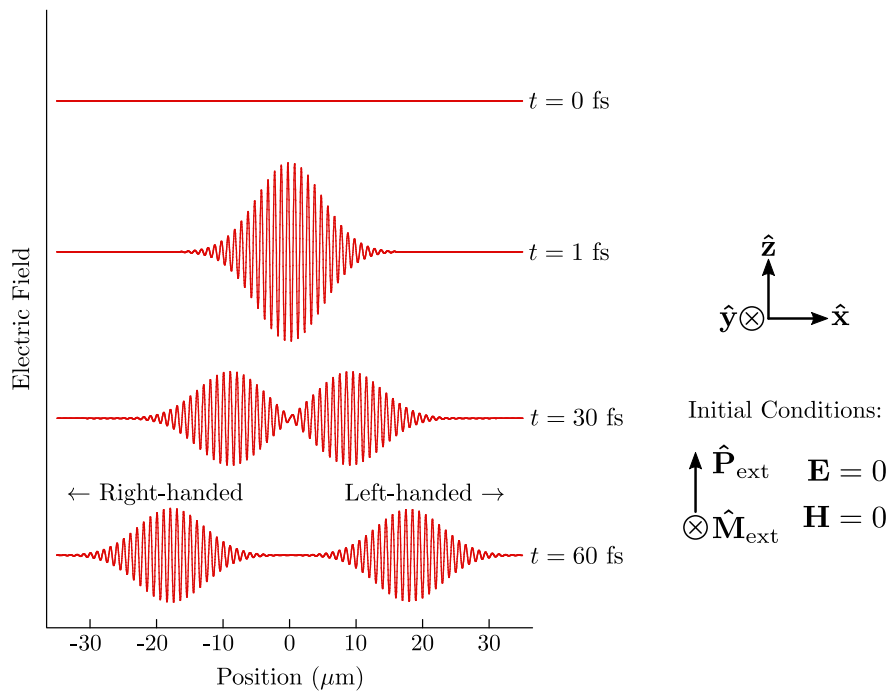


Figure 3.3: *Left-Handed Wave Simulation With No Initial Fields*. If an external polarization and magnetization with the correct phases and amplitude exist in a region where there initially is no electric or magnetic field both a right- and left-handed wave are created and propagate as shown. The two waves propagate in opposite directions in such a way that they cancel each other out at $t = 0$.

In the second case, shown in figure 3.3, no electric or magnetic fields are present initially. The polarization and magnetization then create both a right- and left-handed wave that propagate in opposite directions. The two waves travel in such a way that at time $t = 0$ they cancel each other out to satisfy the initial conditions. The right handed wave that is traveling to the left in figure

3.3 is a self sustaining wave that is traveling through free space (as opposed to any region that is polarized or magnetized).

After the case of one dimensional wave propagation the next most interesting thing to explore is refraction at an interface between a region of free space and a material that is able to be polarized and magnetized. It is important to understand the direction of the wave vector on either side of the interface as illustrated in figure 1.4. When refracting from a positive to a negative index material, or vice versa, the wave vector switches directions. As seen in figure 1.4b, both wave vectors point toward the interface. In the time reversed case all wave vectors would change direction and figure 1.4b would have both wave vectors pointing away from the interface.

Figure 3.4 shows this second case. The region on the right is a material that is able to be polarized and magnetized and the region on the left is free space. The pulse of polarization and magnetization are denoted by the dashed circle. These simulations were again created by solving Maxwell's equations with no approximations and enforcing the boundary conditions (equation 1.11). The polarization and magnetization were defined functions for every point in time, as opposed to having an electric and magnetic field create a polarization and magnetization.

The 2D plots are showing the electric field at four different moments in time. The polarization and magnetization could be caused by one or multiple lasers. As this laser pulse enters the right region of the graph, a polarization and magnetization is set up with the conditions stated at the end of section 3.1 so that a left-handed wave propagates inside the region where the polarization and magnetization exist. The pulse that emerges in the free space region is not a reflection because there is no incident field per se. It is actually a refracted pulse that results from the left-handed wave interacting with the boundary.

3.3 Implementation in an Atomic System

In order to implement this scheme in an atomic system it is still necessary to use a magnetic dipole transition in order to be able to manipulate a magnetization. The advantage to the idea described in this chapter is that there is no density requirement to achieve left-handed waves.

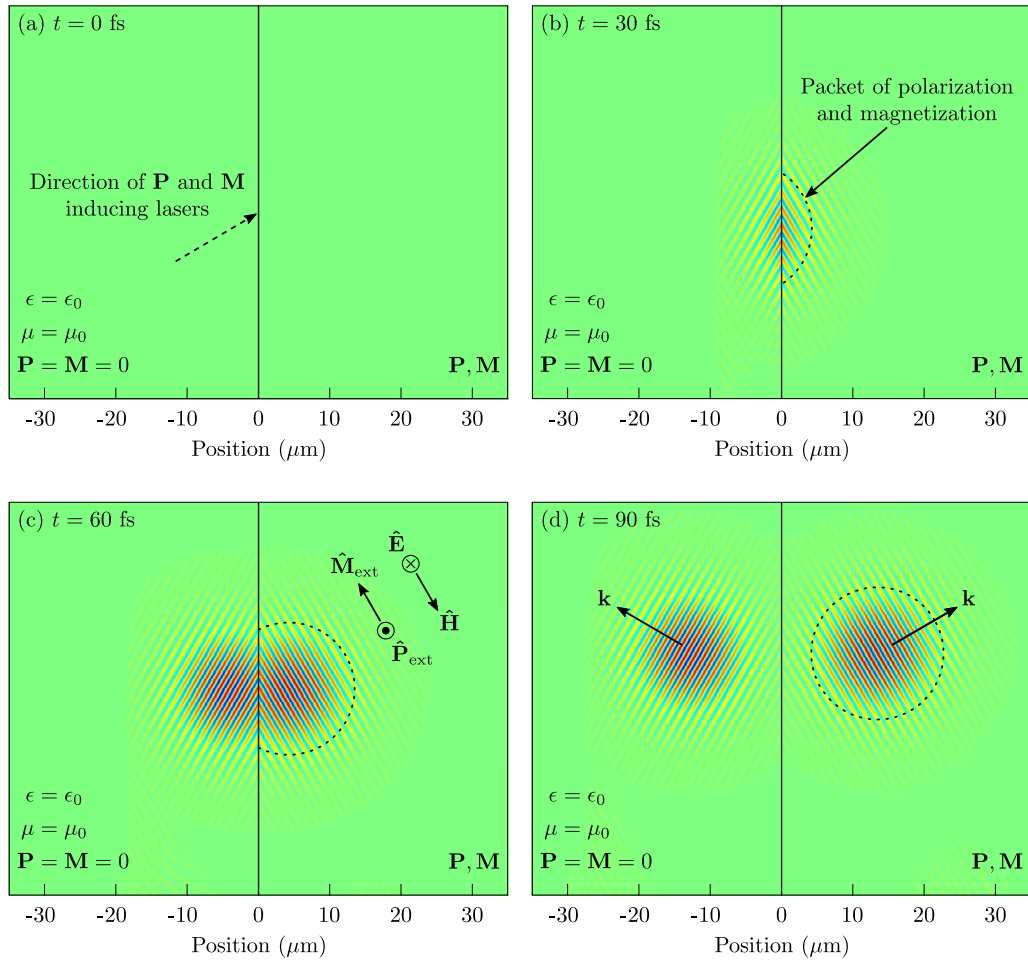


Figure 3.4: *Refraction out of Externally Polarized and Magnetized Material.* (a) The direction of an incoming EM field that will polarize and magnetize the right region. (b) As the right hand region becomes polarized and magnetized, a left-handed wave is created. The false-color wave shown is the electric field of the EM wave that is created by the polarization and magnetization. The dashed line outlines where the polarization and magnetization exist. (c) The direction of the polarization, magnetization, electric, and magnetic field are shown. A right-handed wave, as a result of refraction, emerges into the region of free space. (d) The wavevector of both the right-handed and left-handed wave are shown. The directions of the wavevector are consistent with the directions expected from an EM wave traveling from a left-handed material and refracting into free space.

Whereas in typical negative index experiments it is necessary to modify χ_M by large enough amounts to cause the permeability to be negative (see equation 1.19), in the scheme proposed here it is only necessary to have a polarization and magnetization with the correct phase and ratio. It is still advantageous to have a large magnetic dipole moment and high density, but only because having a larger magnetization will allow for a higher intensity of left-handed waves.

By using the ${}^7F_0 \rightarrow {}^5D_1$ transition in europium that is detailed in chapter 2, a macroscopic magnetization should be able to be produced. The next step will be producing a polarization that can be used in combination with the magnetization to drive a left-handed wave.

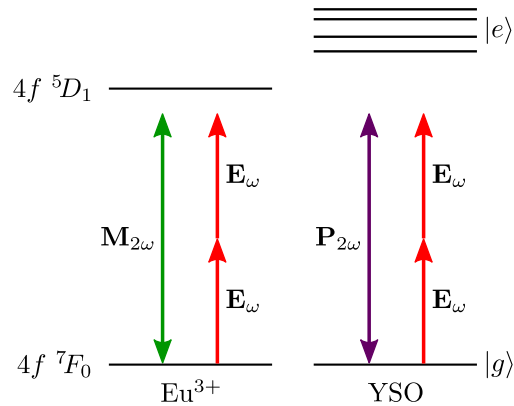


Figure 3.5: *Generating M and P in an Atomic System.* Scheme for inducing a polarization and magnetization in the Eu:YSO crystal. The idea is to use a two photon process to excite a second order magnetization in the europium and use a nonlinearity in the YSO host crystal to produce a second order polarization. This method will eliminate any confusion over the driving fields and the left-handed light that is produced because one will be 1055 nm light and the other will be 527.5 nm light.

One concern is that if the M and P fields are produced by the 527.5 nm laser, it will be difficult to distinguish from the small amount of left-handed light that will also be at that wavelength. To solve this problem, one idea is to use a second order magnetization and polarization so that the driving fields are infrared lasers at 1055 nm and the left-handed light that is produced is green 527.5 nm light. The basic idea for the scheme is shown in figure 3.5. The ${}^7F_0 \rightarrow {}^5D_1$ transition

will produce the magnetization and a nonlinearity in the host crystal will produce the polarization. One catch is that YSO belongs to the C_{2h} crystal class. For this class of crystal it turns out that all elements of the second-order susceptibility tensor vanish, so second harmonic generation is not possible [44]. Luckily there may be a way around this. There is a technique called electric field induced second harmonic generation (EFISH) that uses the third order nonlinearity to produce a second harmonic beam [45][46]. In short, while a second-order susceptibility allows two fields with frequencies ω_1 and ω_2 to produce a polarization (and therefore an electric field) with frequencies $2\omega_1$, $2\omega_2$, $(\omega_1 - \omega_2)$, $(\omega_1 + \omega_2)$, or $(\omega = 0)$, a third-order susceptibility allows three fields with frequencies ω_1 , ω_2 , and ω_3 to produce a polarization with every combination of frequencies involving ω_1 , ω_2 , and ω_3 , including $(\omega_1 + \omega_2 + \omega_3)$. If one of the electric fields is DC, that means that one frequency is zero, say $\omega_1 = 0$. Now the resulting polarization will have a frequency of $(0 + \omega_2 + \omega_3)$ and will behave like sum frequency generation. The hope is that the third-order susceptibility of the host crystal can be exploited to generate a polarization at a wavelength of 527.5 nm to combine with the magnetization the ${}^7F_0 \rightarrow {}^5D_1$ transition produces.

Chapter 4

Experimental Setup

4.1 Laser Overview

The wavelength of the ${}^7F_0 \rightarrow {}^5D_1$ transition in europium is 527.5 nm. A large part of this project was putting together a laser with the right wavelength. In short, what was settled on was using a 1055 nm external cavity diode laser amplified by a NuFern 10 W fiber amplifier. The amplified infrared laser was then frequency doubled using a ring cavity with a periodically poled KTP (PPKTP) crystal inside. The laser setup is shown in figure 4.1.

The external cavity diode laser (ECDL) is set up in the Littrow configuration [47]. The beam is first sent through an isolator to reduce feedback from back reflections and then broken up into three paths using the beamsplitters BS1 and BS2. One path is sent through an EOM and then aligned to an ultra-low expansion (ULE) glass cavity. The ULE cavity is housed in a vacuum chamber that is maintained by an ion pump around 5×10^{-8} torr. The EOM produces frequency side bands on the laser and the Pound-Drever-Hall (PDH) locking scheme is used to lock the ECDL to the ULE cavity [48]. The locking circuit sends high frequency feedback to the laser diode current and low frequency feedback to the piezo that controls the ECDL cavity length. By locking to the ULE cavity the linewidth of the laser is narrowed from ~ 300 kHz to ~ 50 kHz. Information on measuring the linewidth is found in appendix D. The circuitry of our specific lock box is detailed in reference [33]. The transmitted beam through BS2 is coupled to a fiber with the purpose of characterizing the beam via a wavemeter, optical spectrum analyzer, or self-heterodyne interferometer to measure the linewidth. The reflected beam from BS2 is used to seed a 10 Watt

fiber amplifier. The fiber amplifier output is coupled to a ring cavity that is used to frequency double the laser to the appropriate wavelength.

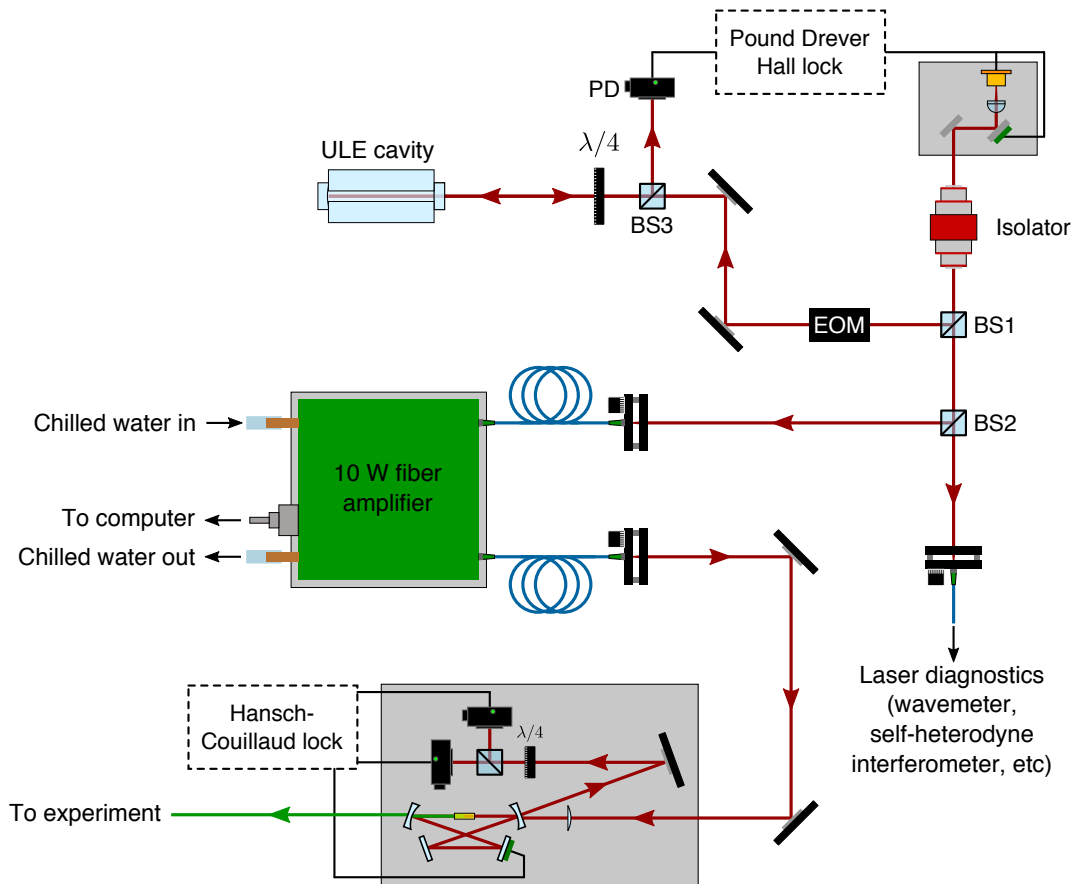


Figure 4.1: *Laser Setup.*

The ring cavity is locked to the laser via the Hansch-Couillaud locking technique [49][50]. In this case the cavity is kept resonant with the laser by feeding back to a piezo on one of the cavity mirrors. Neutral density filters need to be used on the reflected signal so the locking photodiodes don't saturate. For higher input powers, more attenuation is needed. More detailed information about our specific Hansch-Couillaud circuit design can be found in [33]. Around 1.5 W of 527.5 nm light is generated from 6 W of 1055 nm light. Thermal effects seem to affect the lock's stability if more than 6.5 W of 1055 nm light is input. In order to combat this, the waist inside the crystal was loosened from the optimal Boyd-Kleinman waist of $25.4 \mu\text{m}$ to $50.2 \mu\text{m}$. No parts of this system

need regular maintenance, other than routine realignment. The ion pump on the ULE cavity's vacuum chamber needs to be turned on after any power outages. The chamber can maintain high vacuum for presumably a few days, the ion pump was always able to be turned on again after any power outages without having to rough it back down with the turbo pump. The laser diode has gone bad and been replaced a couple times. Symptoms included no narrowing of linewidth when locked and frequency side lobes when viewed on the optical spectrum analyzer.

4.2 Second Harmonic Generation

Second harmonic generation (SHG) is a popular way to achieve appreciable amounts of laser power at wavelengths that are otherwise inaccessible. Diode lasers and fiber amplifiers are available at a wavelength of 1055 nm, which works out in our favor because it is half of the frequency of the ${}^7F_0 \rightarrow {}^5D_1$ transition (527.5 nm) in europium.

The mathematical details of SHG starting with Maxwell's equations can be found in appendix A. The final result, the coupled amplitude equations, are:

$$\frac{dA_1}{dz} = \frac{2i\omega_1^2 d_{\text{eff}}}{k_1 c^2} A_2 A_1^* e^{-i\Delta k z} \quad (4.1a)$$

$$\frac{dA_2}{dz} = \frac{i\omega_2^2 d_{\text{eff}}}{k_2 c^2} A_1^2 e^{i\Delta k z}, \quad (4.1b)$$

where ω is the angular frequency of light, d_{eff} is the nonlinear coefficient that quantifies how much nonlinear response should be expected, k is the wavevector, A is the amplitude of the electric field, and the wave vector mismatch, Δk , is

$$\Delta k = 2k_1 - k_2. \quad (4.2)$$

4.2.1 Phase Matching

An important aspect of employing SHG is proper phase matching. Phase matching occurs when $\Delta k = 2k_1 - k_2 = 0$ and consequently allows the maximum amount of second harmonic light to be generated. The physical picture of this is shown in figure 4.2. When an electromagnetic wave with frequency ω_1 propagates through a material with a speed v_1 , a polarization is generated that also

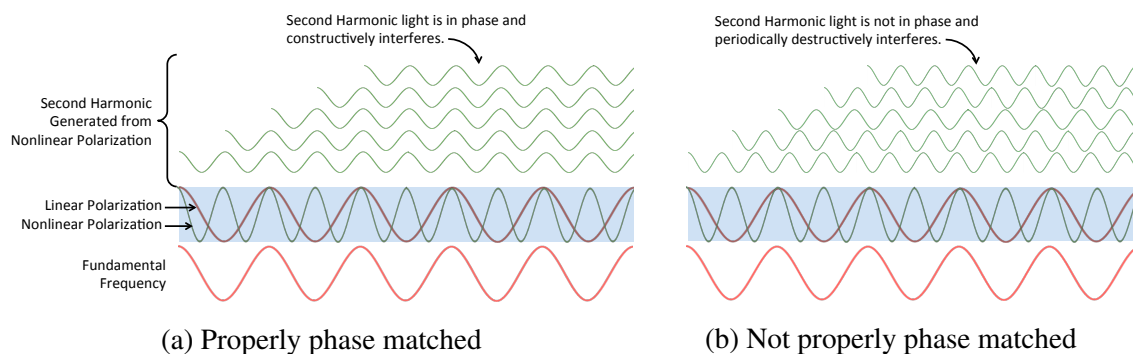


Figure 4.2: *Phase Matching*. Physical interpretation of phase matching

oscillates at frequency ω_1 and travels with a speed v_1 . This polarization in turn creates an oscillating electric field which is exactly in phase with the original field that created the polarization and, assuming no losses, the intensity of the wave remains constant. When a medium has a nonlinear response, however, it is possible that a polarization at a different frequency is also created. In the case of SHG, a polarization is created that oscillates at $2\omega_1$ and travels with speed v_1 . This second order polarization generates an electric field oscillating at frequency $2\omega_1$ but because the speed of light in a material varies with wavelength, the speed of the second harmonic light is $v_2 (\neq v_1)$. The second order polarization then travels at the speed of the fundamental wave and drifts in and out of phase with the second harmonic light that it generates. This causes the second harmonic light's electric field amplitude to oscillate over the length of the nonlinear medium due to interference (figure 4.2b). The length of crystal that it takes for the electric field amplitude to go from zero to a maximum value is called the coherence length, see figure 4.3. Perfect phase matching occurs when the second harmonic wave travels at the same speed as the fundamental wave and the electric field amplitude of the second harmonic wave only increases along the length of the crystal.

One way to achieve phase matching is to exploit the birefringence of a crystal. This is done by tuning the temperature of the crystal and/or shining the fundamental beam in at the correct angle such that the fundamental wave and second harmonic wave see the same index of refraction. Another way to get efficient SHG is to use what is called quasi-phase matching. This involves 'periodically poling' the crystal so that the crystal axes flip direction periodically and instead of

beginning to destructively interfere, the field amplitude grows further. Quasi-phase matching is illustrated in figure 4.3. In our case, PPKTP was chosen as the nonlinear crystal due to its high nonlinear coefficient, d_{eff} , and low absorption at the fundamental and second harmonic frequencies.

The poling period, Λ is calculated using

$$\Lambda = \frac{2\pi}{k_1 + k_2 - k_3}, \quad (4.3)$$

where, for SHG, $k_1 = k_2$ and is the wavevector for the fundamental beam and k_3 is the wavevector for the second harmonic beam. Since $k_i = \frac{2\pi n_i}{\lambda_i}$ the poling period can be rewritten as

$$\Lambda = \frac{1}{2n_\omega/\lambda_\omega - n_{2\omega}/\lambda_{2\omega}}. \quad (4.4)$$

The index of refraction of KTP that Raicol referred me to was from Fan, et al [51]:

$$n_z^2 = A + \frac{B}{1 - \frac{C}{\lambda}} - D\lambda^2 \quad (4.5)$$

where

$$A = 2.25411$$

$$B = 1.06543$$

$$C = 0.05486$$

$$D = 0.02140$$

and λ is the vacuum wavelength in microns. In order to have the option to see at least four of the six peaks that the 5D_1 level is split into (due to inequivalent crystal sites and stark splitting, see chapter 2), the PPKTP crystal was actually poled so that at room temperature it was phase matched at 1053 nm. This allowed us to see the middle stark level. The lowest stark level can then be addressed by heating up the crystal (see figure 4.6 below). Using $\lambda_\omega = 1053$ nm, $\lambda_{2\omega} = 526.5$ nm, and equation 4.5, the poling length of the PPKTP crystal should be

$$\Lambda = 8.7 \mu\text{m}. \quad (4.6)$$

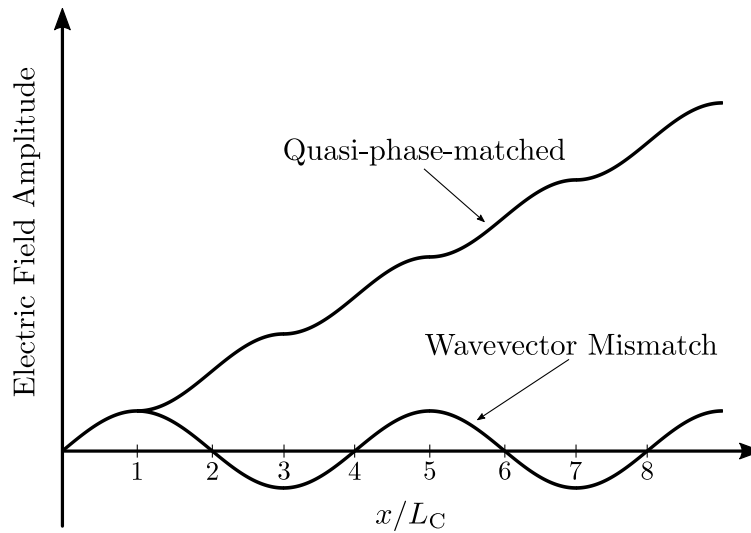


Figure 4.3: *Quasi-Phase Matching*. Illustration of what is gained by quasi-phase matching. The vertical axis is the electric field amplitude of the second harmonic wave. The horizontal axis is the distance along the crystal in multiples of the coherence length, L_C . If a wavevector mismatch is present, the electric field amplitude of the second harmonic will oscillate as shown and no appreciable field will be generated. If the crystal is periodically poled and quasi-phase matching is employed, every time the field amplitude would begin to decrease, the change in crystal axis causes the electric field in the next half period to invert.

4.2.2 Single Pass Results

For a well phase matched crystal, SHG becomes more efficient with increasing fundamental intensity. A laser beam can be focused tightly to increase intensity. A tighter focus causes more efficient SHG, but over an increasingly small area. If the focus is loosened there will be less efficient generation over a larger area. For a gaussian beam there is an optimal focus that depends on the wavelength of the fundamental beam and the length of the crystal, this is called the Boyd-Kleinman focus [52]. In order to get the most efficient generation the beam waist at the center of the crystal

should be

$$w_0 = \sqrt{\frac{\lambda L}{2\pi n_c(2.84)}}, \quad (4.7)$$

where λ is the wavelength of the fundamental beam, n_c is the index of refraction of the crystal, and L is the length of the crystal. In our setup $\lambda = 1055$ nm, $n_c = 1.83$, and $L = 2$ cm. For these parameters the optimal waist at the center of the crystal is $25.4 \mu\text{m}$.

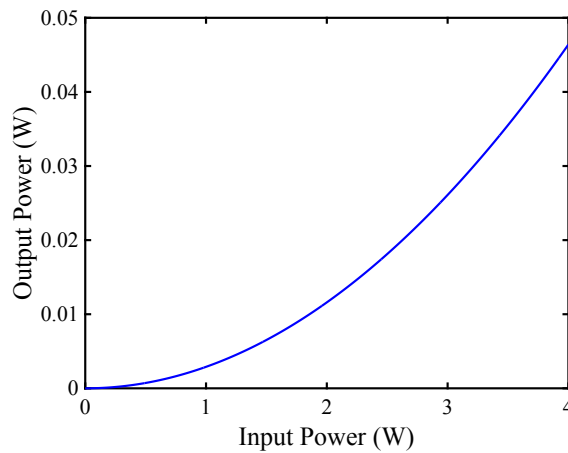


Figure 4.4: *Expected Single Pass Efficiency.* Expected power after a single pass for a 2 cm PPKTP crystal

There are analytic solutions to equations 4.1 for certain situations, but for the purpose of the experiment they were solved numerically using a 4th order Runge-Kutta method described in appendix C. Equations 4.1 assume plane waves, so in order to approximate a gaussian beam several simulations were run sampling over a gaussian profile. Figure 4.4 shows the expected single pass efficiency for up to 4 W of fundamental power. Even for 4 W of input power, only a little over 0.045 W of second harmonic power is generated if everything goes perfectly. This corresponds to a single pass efficiency of $E_{\text{NL}} = \frac{P_{\text{out}}}{P_{\text{in}}^2} = 0.0029$. This isn't sufficient power for any experiment. In order to increase the efficiency of the process, as discussed later in this chapter, the crystal was placed in an optical cavity.

A lot of useful things can be learned, however, using the single pass set up. The single pass efficiency data is shown in figure 4.5. The single pass efficiency was found to be $E_{NL} = 0.0027$, only 7% off from the simulated value.

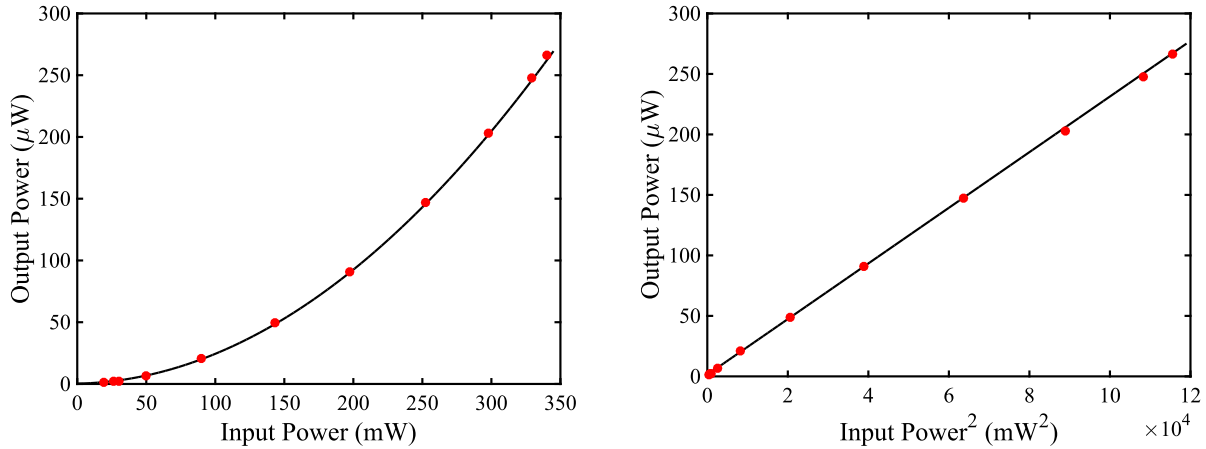


Figure 4.5: *Measured Single Pass Efficiency*. Output power vs input power for a single pass through the crystal. The single pass efficiency, $E_{NL} = \frac{P_{out}}{P_{in}^2}$, is found from the slope of a P_{out} vs P_{in}^2 graph. In this case $E_{NL} = 0.0027$.

Another useful thing to know is the temperature bandwidth and how the optimal temperature changes with wavelength. These results can be seen in figure 4.6. From the data in figure 4.6, the temperature bandwidth is 2.4 °C and the temperature tuning coefficient is 0.0591 nm/°C. Using these two numbers, the wavelength bandwidth at a given temperature can be calculated:

$$\Delta\lambda = 2.4\text{ °C} \times 0.0591 \frac{\text{nm}}{\text{°C}} = 0.142 \text{ nm} \quad (4.8)$$

These numbers can be compared to other references as a gauge for what should be expected. Ref [53] reports a temperature bandwidth of 3 °C for a PPKTP that is 19 mm long. Alex Skliar from Raicol Crystals reported in an email that they measured the temperature tuning to be 0.053 nm/°C for SHG at 1064 nm. Lastly, the wavelength bandwidth of the crystal can be calculated using [54]:

$$\Delta\lambda = \frac{0.4429\lambda_\omega}{L} \left| \frac{n_{2\omega} - n_\omega}{\lambda_\omega} + \frac{\partial n_\omega}{\partial \lambda} - \frac{1}{2} \frac{\partial n_{2\omega}}{\partial \lambda} \right|^{-1} \quad (4.9)$$

where n_ω and $n_{2\omega}$ are calculated using equation 4.5. Matlab was used to numerically find the wavelength bandwidth according to these equations and the result for a fundamental wavelength

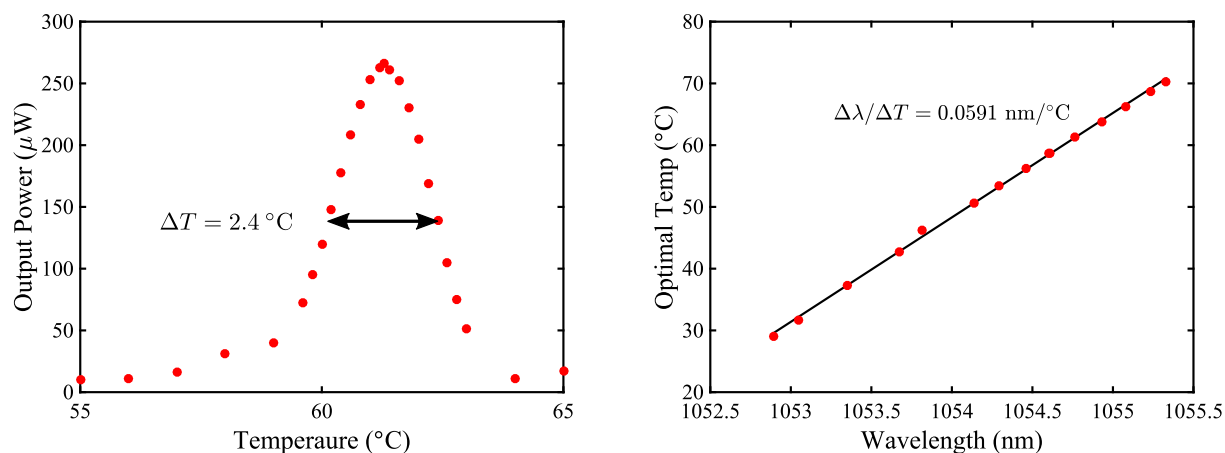


Figure 4.6: *Temperature Dependence*. Temperature bandwidth measurement taken at 1055 nm and optimal temperature's dependence on wavelength.

of 1055 nm is:

$$\Delta\lambda = 0.129 \text{ nm}. \quad (4.10)$$

The following table summarizes the results between the measured values and the expected values:

	Measured	Expected
Single Pass Efficiency	.0027 W^{-1}	.0029 W^{-1}
Temperature Bandwidth	2.4 $^{\circ}\text{C}$	3 $^{\circ}\text{C}$
Wavelength Bandwidth	0.142 nm	0.129 nm
Temperature Tuning Coefficient	0.0591 $\frac{\text{nm}}{^{\circ}\text{C}}$	0.053 $\frac{\text{nm}}{^{\circ}\text{C}}$ (@1064 nm)

Lastly, Raicol's website claims absorption coefficients of $\alpha < 50 \text{ ppm cm}^{-1}$, which would give a loss of 0.01% due to absorption. The total measured loss was 2%, which includes absorption in the crystal and reflections off the faces.

4.3 Cavities

In order to get better SHG efficiency, the crystal can be placed in an optical cavity that is resonant with the fundamental wavelength. This essentially recycles the power of the fundamental

beam that wasn't converted into second harmonic light and sends it through again. Efficiencies exceeding 70% have been reported for cavity-enhanced SHG [55][56][57]. Before discussing this cavity enhancement, it is important to understand the design of optical cavities in general.

In the ray approximation it is most efficient to predict the path of the beam using ray matrices [58]. For a given initial height off the optical axis, x_0 , and angle from the horizontal, θ_0 , the final height and angle can be calculated by multiplying the vector $\begin{pmatrix} x_0 \\ \theta_0 \end{pmatrix}$ by the appropriate set of matrices that describe the optical system the beam is propagating through. These ray matrices are shown in figure 4.7. The elements of a ray matrix are typically labeled $\begin{pmatrix} A & B \\ C & D \end{pmatrix}$.

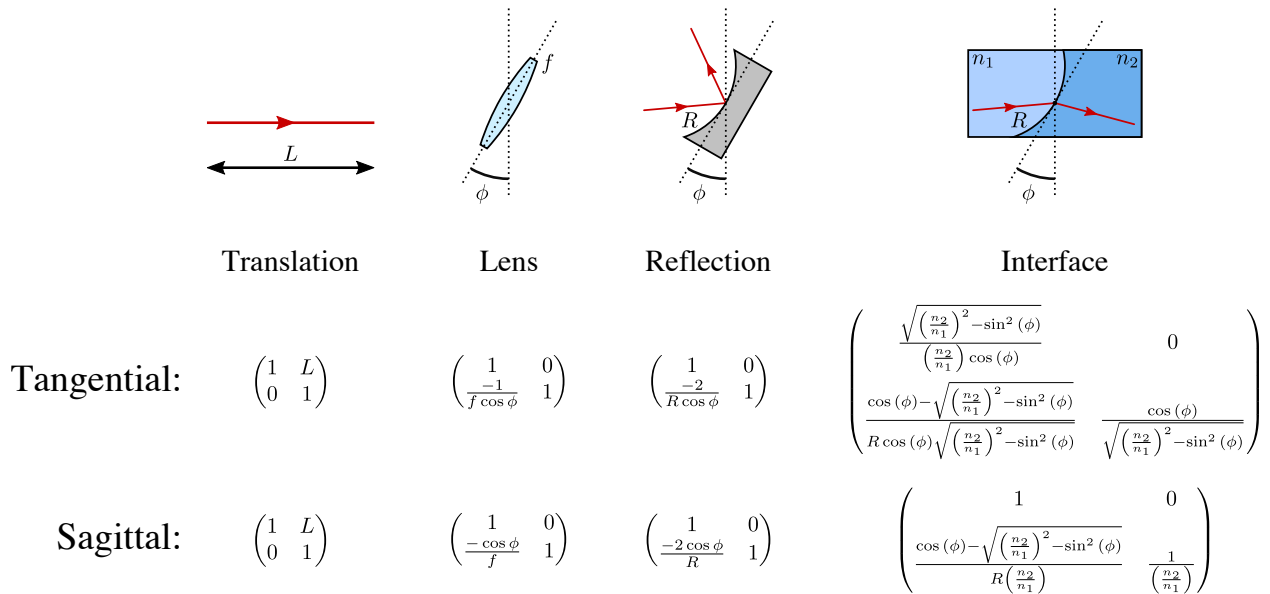


Figure 4.7: *Ray Matrices*. Ray matrices from ref [59]

The ray matrix method can also be used to predict the evolution of the ‘complex radius of curvature’ parameter, q , of a gaussian beam. It is instructional to work through the details of a linear cavity because the solutions can be cleanly written symbolically. The ray matrix of a ring cavity is more complex and in our case was calculated using Matlab.

4.3.1 Linear Cavities

The propagation rule for gaussian beams is

$$q_2 = \frac{Aq_1 + B}{Cq_1 + D}, \quad (4.11)$$

where the gaussian beam parameter q can be thought of as a ‘complex radius of curvature’ and is defined as

$$\frac{1}{q} = \frac{1}{R} + i \frac{\lambda}{\pi n w^2}, \quad (4.12)$$

where R is the radius of curvature of the wavefront, λ is the wavelength of light, n is the index of refraction, and w is called the spot size and is the $1/e^2$ radius of the beam intensity. It is also useful to know how R and w change with position along the axis of gaussian beam:

$$R = z \left[1 + \left(\frac{\pi w_0^2}{\lambda z} \right)^2 \right] \quad (4.13)$$

$$w^2 = w_0^2 \left[1 + \left(\frac{\lambda z}{\pi w_0^2} \right)^2 \right], \quad (4.14)$$

where w_0 is called the beam waist and is the point where the spot size is the smallest, and z is the position with respect to the reference point along the beam (equations 4.13 and 4.14 assume $z = 0$ is at a waist).

In order for light to resonate in a cavity, the beam must overlap itself on consecutive round trips. At any point along the path the spot size and radius of curvature must match, this means that after one round trip $q_1 = q_2$ and equation 4.11 can be rewritten as

$$q = \frac{Aq + B}{Cq + D}. \quad (4.15)$$

The fact that $AD - CB = 1$ (because ray matrices must be unitary) can be used to eliminate C . Equation 4.15 can then be solved for $1/q$:

$$\frac{1}{q} = \frac{D - A}{2B} \pm \frac{i}{2B} \sqrt{4 - (A + D)^2}. \quad (4.16)$$

The real and imaginary parts of this equation can be matched to the general formula for the complex radius of curvature (equation 4.12):

$$\frac{1}{R} = \frac{D - A}{2B} \quad \rightarrow \quad R = \frac{2B}{D - A} \quad (4.17)$$

$$i \frac{\lambda}{\pi n w^2} = \frac{i}{2B} \sqrt{4 - (A + D)^2} \quad \rightarrow \quad w^2 = \pm \frac{2\lambda}{\pi n} \frac{B}{\sqrt{4 - (A + D)^2}}. \quad (4.18)$$

In order for the cavity to resonate, a waist must form somewhere so that each consecutive trip doesn't continue to diverge indefinitely. This imposes two requirements on the ray matrix elements. The first is that $A = D$ if the starting and end point of the ray matrix is at a waist, because at a waist the radius of curvature is infinite. The second is that $|A + D| \leq 2$. If this were not the case, the square root in equation 4.18 would have a negative sign under it, consequently causing the second term in $1/q$ to become real. Using these two restrictions, the cavity waist can be found using

$$w_0^2 = \pm \frac{\lambda}{\pi n} \frac{B}{\sqrt{1 - A^2}}. \quad (4.19)$$

Now that the relation between the waist, wavefront radius of curvature, and ray matrix elements are known, the ray matrix of the cavity needs to be constructed. To do this, the ray matrix must

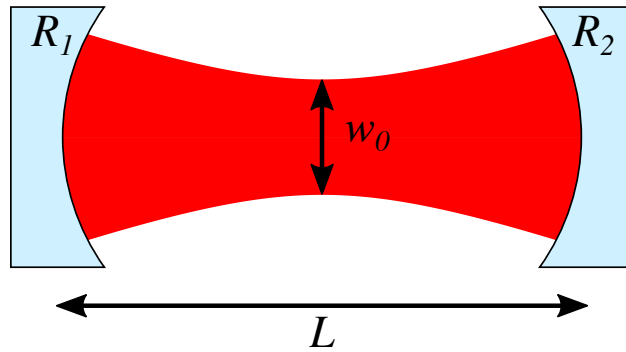


Figure 4.8: *Linear Cavity.*

begin being constructed at the center of the cavity where the waist is formed:

$$M = \begin{pmatrix} 1 & \frac{L}{2} \\ 0 & 1 \end{pmatrix} \begin{pmatrix} 1 & 0 \\ -\frac{2}{R_2} & 1 \end{pmatrix} \begin{pmatrix} 1 & L \\ 0 & 1 \end{pmatrix} \begin{pmatrix} 1 & 0 \\ -\frac{2}{R_1} & 1 \end{pmatrix} \begin{pmatrix} 1 & \frac{L}{2} \\ 0 & 1 \end{pmatrix}. \quad (4.20)$$

When these matrices are multiplied out, the result is

$$M = \begin{pmatrix} 1 + \frac{2L^2 - L(3R_2 + R_1)}{R_1R_2} & 2L + \frac{-R_2L^2 + L^3 - \frac{3}{2}L^2R_1 - \frac{1}{2}L^2R_2}{R_1R_2} \\ \frac{4L - 2(R_1 + R_2)}{R_1R_2} & 1 + \frac{2L^2 - L(3R_1 + R_2)}{R_1R_2} \end{pmatrix}, \quad (4.21)$$

where R_1 and R_2 are the reflectances of the mirrors and L is the length of the cavity, as shown in figure 4.8. Since $A = D$ in equation 4.21, the initial and final q parameters must be at a waist, due to the discussion above. The condition that $|A + B| \leq 2$ can be used to find determine whether or not a cavity will stable:

$$-1 < \frac{L^2 - LR_1 - LR_2}{R_1R_2} < 0. \quad (4.22)$$

If the values of L , R_1 , and R_2 satisfy this condition, it is possible to have a stable cavity. For a good discussion of different types of cavity geometries, see reference [58]. Since not all cavities are symmetric, it might be the case that the waist is not in the center. In this case, the same ray matrices multiplied together in equation 4.20 can be used, except they begin at a distance Δ from the center of the cavity:

$$M = \begin{pmatrix} 1 & \frac{L}{2} + \Delta \\ 0 & 1 \end{pmatrix} \begin{pmatrix} 1 & 0 \\ -\frac{2}{R_2} & 1 \end{pmatrix} \begin{pmatrix} 1 & L \\ 0 & 1 \end{pmatrix} \begin{pmatrix} 1 & 0 \\ -\frac{2}{R_1} & 1 \end{pmatrix} \begin{pmatrix} 1 & \frac{L}{2} - \Delta \\ 0 & 1 \end{pmatrix}. \quad (4.23)$$

When these matrices are multiplied out, the position of the waist can be found by setting $A = D$ and solving for Δ . The solution is:

$$\Delta = \frac{L(R_2 - R_1)}{2(2L - R_1 - R_2)}. \quad (4.24)$$

4.3.2 Ring Cavities

The analysis above can be extended to a cavity of any geometry. If a linear cavity is used for SHG, a standing wave is set up inside the cavity and therefore in the nonlinear crystal. The fact that the nonlinear crystal is only saturated at the antinodes of this standing wave is called spatial

hole burning and is detrimental to the SHG efficiency. In a ring cavity, no standing wave is present and the crystal is uniformly saturated. Linear cavities are also more susceptible to thermal effects compared to ring cavities due to the fact that the beam passes through the crystal twice every round trip [60]. The ring cavity layout used in the experiment is shown in figure 4.9.

The ray matrix for this cavity can be found by multiplying out the following matrices, starting at the center of the crystal:

$$\begin{aligned}
M &= M_{\text{Trans}} \left(\frac{L_c}{2}, n_c \right) && \text{(Left half of crystal)} \\
&\times M_{\text{Inter}}(n_{\text{air}}, n_c, R = \infty, \phi = 0) && \text{(Left crystal surface)} \\
&\times M_{\text{Trans}} \left(\frac{(L_1 - L_c)}{2}, n_{\text{air}} \right) && \text{(Between crystal and left curved mirror)} \\
&\times M_{\text{Refl}} \left(R, \frac{\phi}{2} \right) && \text{(Left curved mirror)} \\
&\times M_{\text{Trans}} (L_{\text{tot}} - L_1, n_{\text{air}}) && \text{(Path length between curved mirrors)} \\
&\times M_{\text{Refl}} \left(R, \frac{\phi}{2} \right) && \text{(Right curved mirror)} \\
&\times M_{\text{Trans}} \left(\frac{(L_1 - L_c)}{2}, n_{\text{air}} \right) && \text{(Between crystal and right curved mirror)} \\
&\times M_{\text{Inter}}(n_c, n_{\text{air}}, R = \infty, \phi = 0) && \text{(Right crystal surface)} \\
&\times M_{\text{Trans}} \left(\frac{L_c}{2}, n_c \right) && \text{(Right half of crystal)}. \quad (4.25)
\end{aligned}$$

For our cavity the total length is $L = 35$ cm, the folding angle was $\phi = 20^\circ$, the crystal length is $L_c = 2$ cm, the index of refraction of the PPKTP crystal is $n_c = 1.8306$, the two curved mirrors have radius of curvature $R = 75$ mm, and the wavelength of light being doubled is $\lambda = 1055$ nm.

A Matlab program was written that varied the curved mirror distance L_1 while keeping the folding angle and total cavity length fixed. If the stability condition $A = D$ was satisfied, the waist at the center of the crystal and between the plane mirrors was calculated. Figure 4.10 shows a plot of beam waist vs the curved mirror separation for both the waist between the curved mirrors and

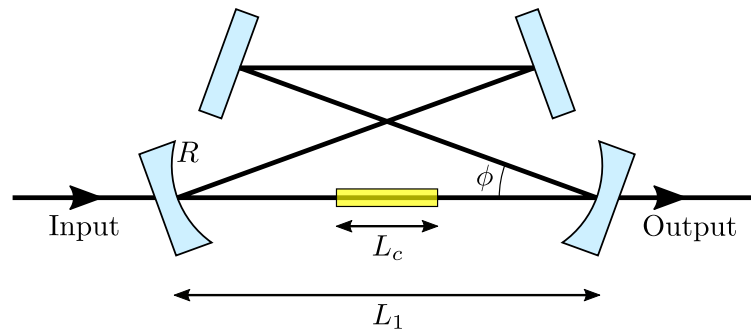


Figure 4.9: *Ring Cavity*. Ring cavity for second harmonic generation. The total length of the cavity is L . Reference [50] has a short discussion on why it is best to couple light into the mirror shown as opposed to one of the flat mirrors.

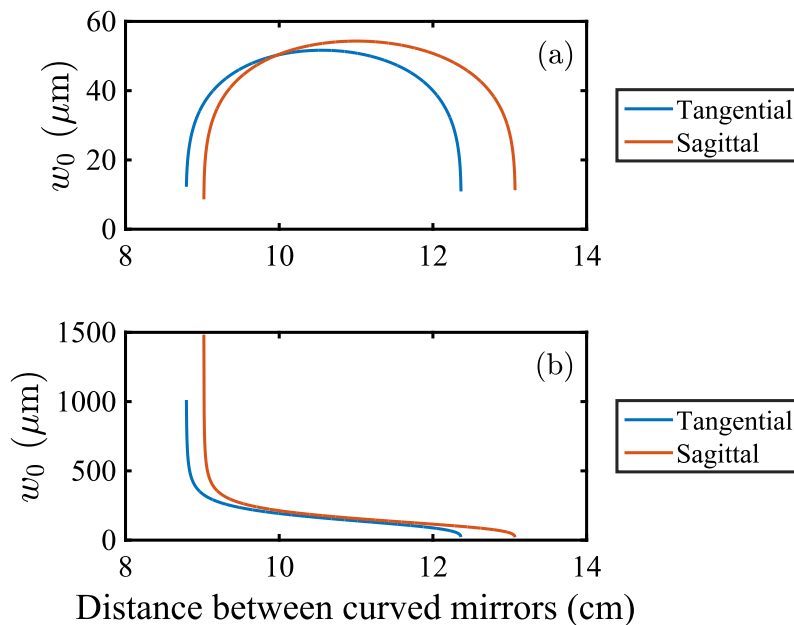


Figure 4.10: *Waists of Stable Ring Cavities*. (a) As the distance between the curved mirrors is varied (assuming the total cavity length doesn't change), only certain distances allow a stable cavity to be formed. Because the fundamental beam is being coupled into the leg between the two curved mirrors, the curved mirror distance that has the same waist for both tangential and sagittal planes is chosen. (b) The waist between the two plane mirrors is shown for interest.

between the plane mirrors for the tangential and sagittal planes. In order to achieve good mode matching the tangential and sagittal waist in the crystal should be as close in size as possible.

Figure 4.11 shows the dimensions of the optimal ring cavity according to Matlab. The waist is loosened from the optimal Boyd-Kleinman waist of $25.4 \mu\text{m}$ to $50.2 \mu\text{m}$ in an attempt to stymie thermal effects. Reference [56] discusses how, inside a cavity, near-optimal efficiency can still be achieved even if the waist inside the crystal is loosened.

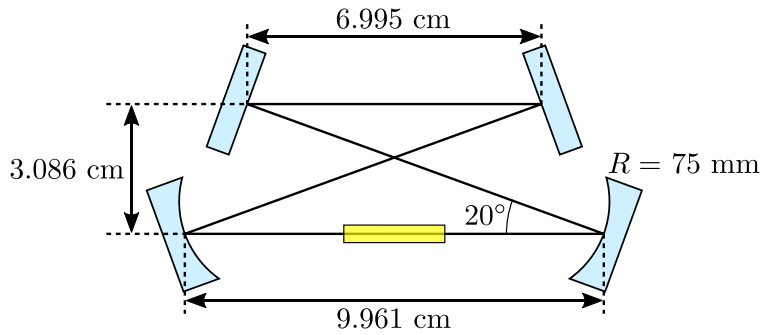


Figure 4.11: *Ring Cavity Dimensions.*

4.3.3 Impedance Matching and SHG Cavity Enhancement

Similar to how impedances need to be matched in electronics to reduce reflections, there is an optimal transmission coefficient of input mirror that that maximizes the amount of light that can be coupled into the cavity. For a cavity containing an SHG crystal, the maximum transmission can be found by using [61]

$$\sqrt{\epsilon} = \frac{T\sqrt{E_{\text{NL}}P_{\text{in}}}}{\left[1 - \sqrt{(1-T)(1-L_0)(1-\sqrt{\epsilon E_{\text{NL}}P_{\text{in}}})}\right]^2}, \quad (4.26)$$

where $\epsilon = \frac{P_{\text{out}}}{P_{\text{in}}}$, the output power over the input power to the cavity, T is the transmission of the input mirror, L_0 is the total loss in the cavity excluding the power converted to the second harmonic, and $E_{\text{NL}} = P_2/P_1^2$, the single pass efficiency of the crystal. Equation 4.26 can be solved for the optimal transmission coefficient:

$$T = \frac{L_0}{2} + \sqrt{\frac{L_0^2}{4} + E_{\text{NL}}P_{\text{in}}}. \quad (4.27)$$

If there were no SHG crystal in the cavity, or if the single pass efficiency was very low, the optimal transmission is $T = L_0$. For a ring cavity, the total loss is

$$L_0 = 1 - R_1 R_2 R_3 R_{\text{cav}} \quad (4.28)$$

where R_1 , R_2 , and R_3 are the reflectances of the three mirrors in the cavity other than the input coupler, and R_{cav} is any other losses in the cavity other than power lost to the SHG process. Each cavity mirror has a reflectance of $>99.9\%$ and the loss from the crystal, stated earlier, is 2% , so the total loss calculated by equation 4.28 is

$$L_0 = 1 - (0.999)(0.999)(0.999)(1 - 0.02) = 0.0229. \quad (4.29)$$

In order to get an idea of how the efficiency varies with T_{in} , equation 4.26 was solved numerically for various input powers, a single pass efficiency of $E_{NL} = 0.0027$, and a total cavity loss of $L_0 = 0.0229$.

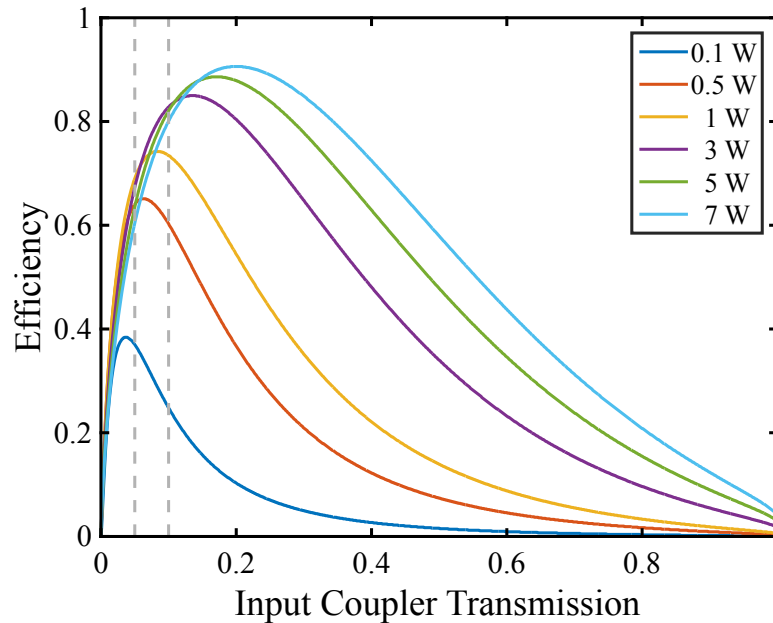


Figure 4.12: *Optimal Input Coupler Transmission*. Optimal transmissions for various fundamental beam input powers. The vertical dotted grey lines are meant to be visual guides and are at $T = 0.05$ and $T = 0.1$.

From figure 4.12, the optimal transmissions for various input powers can be seen. It was decided to buy input couplers with transmissions of 0.05 and 0.1 in order to see close to optimal efficiencies for a range of input powers.

4.3.4 Mode Matching

In order to couple the optimal amount of light into a cavity, in addition to impedance matching, the input beam needs to have a waist that is the same size and in the same position as the cavity waist. To do this, the input beam must be sent through the appropriate lens or lenses to maximally overlap the cavity mode. A Matlab program was written to assist with this that propagates a gaussian beam through any given set of optical elements. Using this program the focal lengths and spacings of lenses are varied until the waist size and position match that of the cavity.

The amount of the input beam that is overlapped with the cavity mode can be quantified by the ‘mode matching coefficient’, m . If the cavity is on resonance, the reflected beam’s intensity is given by [62]:

$$\frac{I_r}{I_{in}} = \frac{m}{R_{in}} \frac{(R_{in} - |g|)^2}{(1 - |g|)^2} + (1 - m)R_{in}, \quad (4.30)$$

where $\frac{I_r}{I_{in}}$ is the measured fraction of the input beam that is reflected, R_{in} is the reflection coefficient of the input mirror, and $|g| = \sqrt{R_{in}R_{out}R_{cav}}$. Using this equation, it is possible to indirectly measure how well the cavity is mode matched. In order to do this, three things need to be measured:

1. $\frac{I_r}{I_{in}}$ is measured from the input beam reflected off of the input mirror while the cavity is on resonance.
2. R_{in} is the reflectance of the input mirror. Ideally this would also account for the reflection off of the back surface of the mirror.
3. By measuring the finesse, $|g|$ can be calculated using $F = \frac{\pi\sqrt{|g|}}{1-|g|}$.

When the cavity was aligned and the temperature was optimized for maximum second harmonic generation, $\frac{I_r}{I_{in}}$ was measured by looking at the reflection dips and was found to be 0.239. The input coupler reflectance, R_{in} was measured by shining a beam through the input coupler and seeing how

much was transmitted. It was found to be $R_{\text{in}} = 0.9476$. The finesse of the cavity was measured by looking at the ratio of the free spectral range to the FWHM of the peaks. It was found that $F = 65.5$, meaning $|g| = 0.9532$. When these numbers are used in equation 4.30, the result is that $m = 0.76$, meaning that 76% of the input light is coupling into the cavity. Equation 4.26 can be used to calculate the efficiency of the cavity for the measured transmission ($T = 1 - R_{\text{in}} = 0.0524$) and a certain input power P_{in} . The output power was measured to be 10 mW with 65.5 mW of input power, giving an efficiency of 15.3%. When these parameters are used in equation 4.26, the predicted efficiency is 14.6%.

Thermal issues become a problem at higher and higher input powers, but 1.5 W of 527.5 nm light can routinely be generated from 6 W of input power, an efficiency of 25%. Perhaps in the future more can be done to optimize the efficiency of the SHG cavity. For example, the waist in the crystal could be loosened further to try to alleviate thermal issues. Also, a redesign of the cavity could take into account any self focusing that might be occurring in the PPKTP crystal.

4.4 Cryostat

At room temperature the phonon vibrations widen the homogeneous linewidth significantly. In order to suppress these phonon vibrations and therefore narrow the linewidth of the ${}^7F_0 \rightarrow {}^5D_1$ transition, it is necessary to cool the crystal down to liquid helium temperatures. To do this, the crystal is housed in an ST-100 liquid helium continuous flow optical cryostat from Janis. The cryostat has four viewports near the cold finger so there is plenty of optical access. The cryostat is pumped down with a HiCube 80 Eco turbo pumping station from Pfeiffer Vacuum. It takes about a day to pump down the cryostat. At room temperature the pressure stays between 10^{-4} and 10^{-5} mbar, but after it is cooled to 5 K the pressure drops to around 10^{-8} mbar. The cryostat itself and pump require almost no maintenance. The pressure gauge however needs to be cleaned every few years. The instructions for cleaning the pressure gauge can be found on the YavuzLab wiki page¹.

¹https://wiki.physics.wisc.edu/yavuz/index.php/Main_Page

Chapter 5

Rabi Flopping on a Magnetic Dipole Transition

5.1 Rabi Flopping

After building up the laser system described in chapter 4 and performing some rudimentary spectral hole burning experiments (see chapter 6), the next goal was to demonstrate a coherent response from the ${}^7F_0 \rightarrow {}^5D_1$ transition. This is interesting for several reasons. The first is that Rabi oscillations have never been observed before on magnetic dipole transitions at optical frequencies. Although this reason alone is enough justification for an experiment to be performed, there are yet more interesting things that can be accomplished. The large density of atoms being coherently driven create a macroscopic magnetization. The extraordinary thing about this magnetization is that it is oscillating at the optical frequency of the ${}^7F_0 \rightarrow {}^5D_1$ transition (568.7 THz). A large magnetization implies a large susceptibility, which in turn modifies the permeability of a material (as discussed in chapter 1). Modifying the permeability of a material in the optical regime is a major hurdle to creating a negative index. As will be discussed, creating a negative permeability is still a ways off. However, using the scheme detailed in chapter 3, a very measurable intensity of left-handed light could be created using the magnetization created by driving the ${}^7F_0 \rightarrow {}^5D_1$ transition.

Qualitatively, Rabi oscillations are the oscillations of wavefunction amplitude of either the ground or excited state, when a resonant laser drives a two-level system. A plot of excited state amplitude vs time will look sinusoidal. Microscopically what is going on is *not* that individual atoms are getting excited until the whole population is excited, and then de-excited until the whole population is back in the ground state. It's that each atom's wavefunction begins in the ground

state, evolves through a superposition state where there is some probability of it being in either the ground or excited state, and finally ends up completely in the excited state, then evolves back to the ground state in a similar way and continues until the process decoheres. The situation where each atom is in a superposition of ground and excited state is what creates the magnetization. When the laser is on resonance, the maximum magnetization is created when the probability of the atom being in the ground state is equal to the probability of it being in the excited state. As will be discussed in section 5.4, the off diagonal density matrix elements are what determines the magnitude of the magnetization.

If the atoms begin in the ground state at $t = 0$ and the laser is exactly on resonance, the probabilities for finding the electron in the upper and lower states are:

$$|a_g|^2 = \cos^2 \frac{\Omega t}{2} \quad (5.1)$$

$$|a_e|^2 = \sin^2 \frac{\Omega t}{2}, \quad (5.2)$$

where a_g and a_e are the amplitudes of the ground and excited state wavefunctions, respectively. The frequency of the Rabi oscillations are determined by

$$\Omega = \frac{\mu B}{\hbar}, \quad (5.3)$$

where Ω is the angular frequency of the oscillation measured, μ is the magnetic dipole moment of the transition, and B is the magnitude of the electromagnetic wave's magnetic field. Rabi flopping occurs at a faster frequency if either the transition has a stronger dipole moment, or the magnetic field is stronger. Because the dipole moment depends on the transition and not anything that is able to be controlled, the only way to see a faster signal is to increase the laser power driving the transition.

5.2 Procedure

Several obstacles needed to be overcome before any Rabi oscillations could be seen. First and foremost was the issue that plagues almost every experiment involving lasers: sufficient power. Although the conversion efficiency of the SHG cavity was successfully predicted at low powers, at

higher powers all bets are off. It is much more of an art than a science to get an appreciable amount of doubled light out with input powers greater than one watt due to thermal issues affecting the cavity. With some practice 1.5 W of green light could be generated.

After the SHG cavity, the beam is split with a beamcube and each path is passed through an 80 MHz AOM. The purpose of the AOM is for timing control. The linewidth of the laser is around 50 kHz and is locked to a ULE cavity peak that is centered on the 1.6 GHz wide inhomogeneous width, so no precise frequency control is needed to ensure the laser is resonant. The beams are focused down to a $\sim 400 \mu\text{m}$ diameter through the AOMs in order to get a rise time of $\sim 40 \text{ ns}$. After the AOMs, each beam is sent into a fiber in order to clean up its spatial profile before being shined into the cryostat. The maximum laser power seen at the crystal was around 300 mW. The RF generators powering the AOMs, the oscilloscopes collecting data, the pulse generator, and the cryostat's temperature controller are all controlled with Matlab via GPIB or serial cables.

The beam's intensity inside the crystal has a gaussian profile. Therefore every point along the transverse dimension of the beam will cause Rabi oscillations with a slightly different frequency. This means that the probe beam sent in to sample the population should ideally be much smaller than the Rabi beam so as to only sample a relatively flat section of the intensity profile. The longitudinal intensity profile also will oscillate the atoms at different frequencies but as long as the Rayleigh range of the beam is longer than the crystal those effects are negligible. Making sure that the probe beam was aligned with the Rabi beam was a little bit of a trick because the probe and Rabi beam were counter propagating. The setup and alignment procedure is shown and described in figure 5.1. In order to ensure the beams are the same frequency, the RF generator powering one of the AOMs was slowly adjusted until the fringes in the interference pattern, indicated in figure 5.1, stopped shifting.

The decay rate from the 5D_1 level is $33 \mu\text{s}$, so all measurements had to be taken within this time in order to observe any coherent effects. This introduced some technical challenges involving detector gain and bandwidth issues. Because the lifetime of the $^7F_0 \rightarrow ^5D_1$ transition is relatively long, it doesn't take much laser power to saturate it and therefore appreciably change the populations in the ground and excited state.

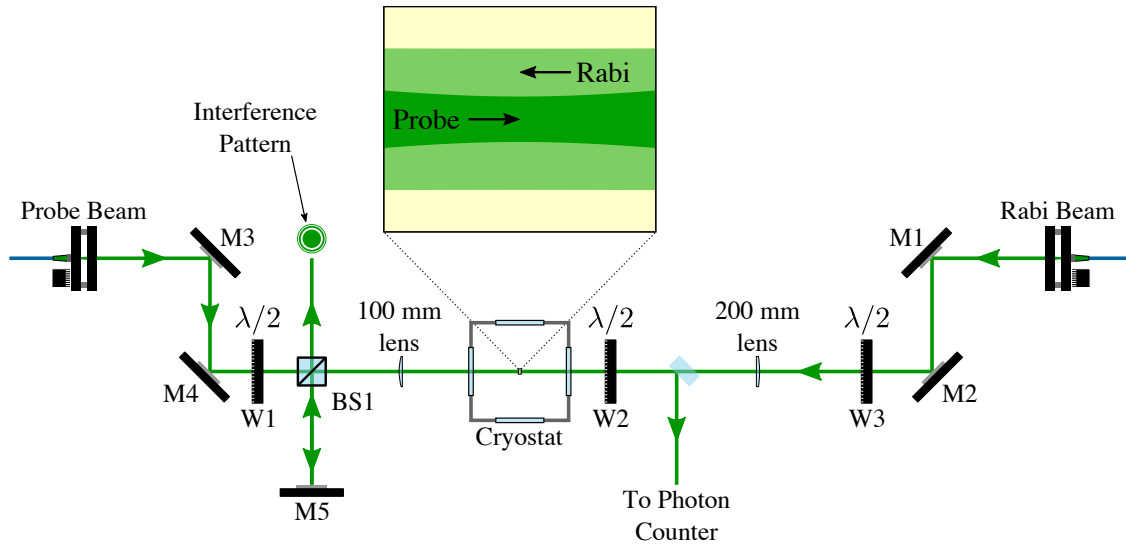


Figure 5.1: *Alignment Scheme*. Scheme used to align the probe to the center of the Rabi beam. While the cryostat is at room temperature, mirrors M1 and M2 were used to walk the Rabi beam through the crystal (shown to scale in cryostat). M5 was then adjusted so that the Rabi beam is exactly retroreflected on itself. Lastly M3 and M4 were used to walk the probe beam on top of the Rabi beam. The beams were considered aligned when a centered bullseye interference pattern was seen out of the unused beamsplitter port as shown. The Rabi beam was focused to a waist size of $56 \mu\text{m}$ and the probe beam was focused to a waist of $18 \mu\text{m}$. To-scale beam profiles are shown in the inset. The polarization was optimized once the cryostat was cooled down to 5 K. First W1 was rotated to maximize fluorescence in the crystal from the probe beam, then W2 was rotated to optimize the reflected signal off the pickoff. Finally, W3 was rotated to maximize fluorescence in the crystal from the Rabi beam.

First, a Stanford Research Systems current preamplifier was used to amplify a photodiode, but when the gain was high enough to get a good signal, the bandwidth was nowhere near what was required to see the fast pulses from the AOMs. Another issue was that even though care was taken to try to block reflections, signal from the Rabi beam got to the detector and contaminated our measurements. Eventually a photon counter was used, which has both a huge gain and huge

bandwidth. The photon counter outputs a 5 V TTL pulse with a 10 ns width every time a photon is detected, allowing probe powers at the picowatt level to be detected. With the photon counter it also became clear that some other fluorescence was contaminating our signal. It was close to the wavelength of the 527.5 nm signal because it was completely blocked along with the probe with the longpass colored glass filter used to see the fluorescence from the 5D_0 level and it didn't go away with green interference filters close to 527.5 nm. We suspect it was decay from the 5D_1 level to some of the higher 7F levels that have transition wavelengths between 533 nm and 542 nm. This fluorescence should be able to indicate any Rabi flopping, but because it wasn't exactly understood, and because it would be sampling from everywhere along the gaussian beam profile it was ignored and only the probe beam signal was used. It was determined that this fluorescence died out in around $10 \mu\text{s}$. For this reason the probe pulse was delayed $15 \mu\text{s}$ after the Rabi pulse. A diagram showing our timing sequence is shown in figure 5.2

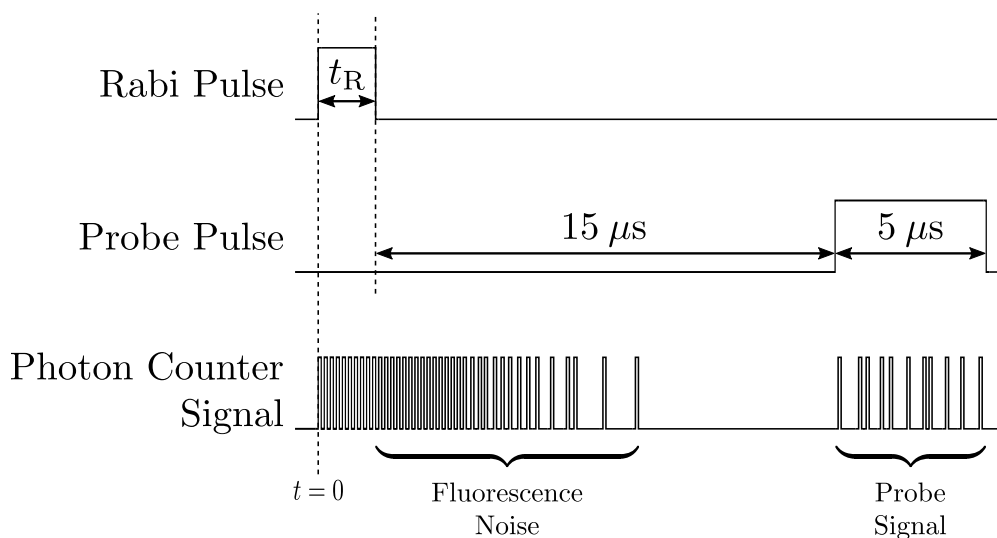


Figure 5.2: *Pulse Sequence*. Pulse Sequence used to measure Rabi oscillations. The Rabi pulse length, t_R , is varied between 0 and $2 \mu\text{s}$ throughout the experiment. The probe pulse is always $5 \mu\text{s}$ and always begins $15 \mu\text{s}$ after the Rabi pulse ends. In the ideal case it would be possible to measure the probe immediately after the Rabi pulse ends, but there is a significant amount of noise due to decay to higher 7F levels.

No spectral hole burning was done so the laser was interacting with as many atoms as it could ‘reach’ within the inhomogeneous broadening. This also means that the dipole moment that was measured was some sort of average of all the combinations of hyperfine ground state to excited state transitions. Future improvements to this procedure are discussed in chapter 6.

5.3 Magnetic Dipole Moment

In order to determine the dipole moment of the transition, Rabi curves were taken with many different Rabi pulse intensities.

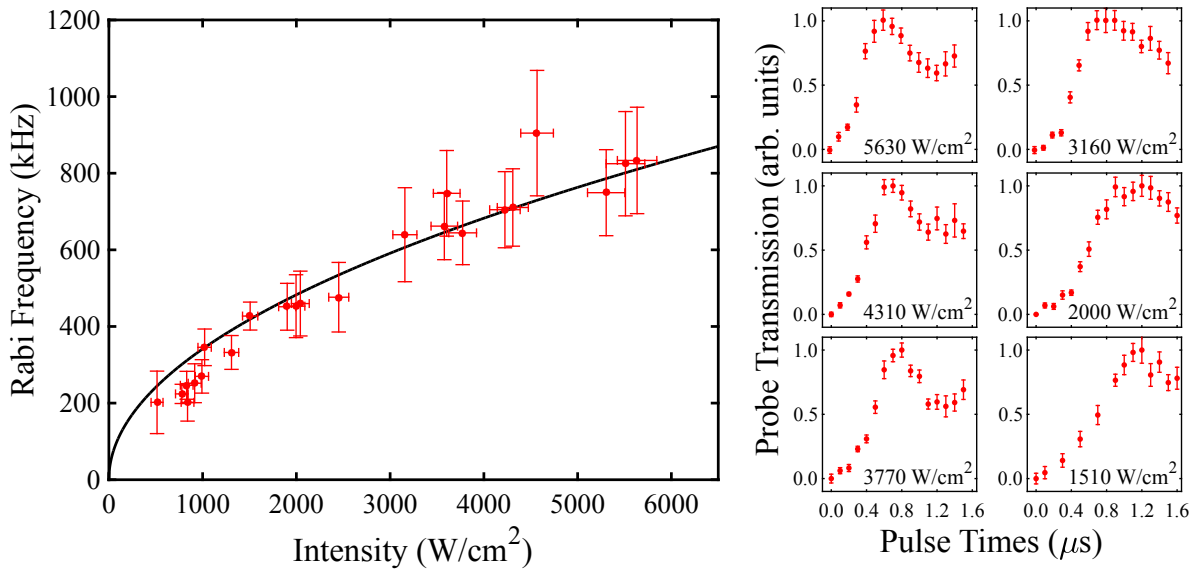


Figure 5.3: *Rabi Oscillation Data*. Rabi Oscillations for different intensities are shown on the right. How the frequency of the Rabi oscillation varies with intensity is shown on the left. The dipole moment was determined by the best fit line to this data.

In order to use equation 5.3, the magnetic field can be calculated by using

$$I = \frac{c}{2n\mu_0} B^2, \quad (5.4)$$

which can be solved for B and plugged into equation 5.3:

$$f = \frac{\mu}{2\pi\hbar} \sqrt{\frac{2n\mu_0 I}{c}}, \quad (5.5)$$

so the frequency is proportional to the square root of intensity. This can be seen in figure 5.3. The intensity of a gaussian beam is $I = 2P/\pi w^2$ where the power was measured on a calibrated photodiode, and the waist w was $56 \mu\text{m}$ for all runs. The frequency was determined by the peak time in each individual Rabi curve, where $f = 1/2t_{\text{peak}}$. Explanation of the error bars can be found in appendix B.

The magnetic dipole moment of the ${}^7F_0 \rightarrow {}^5D_1$ transition is measured to be

$$\mu = (0.063 \pm 0.005)\mu_{\text{B}}. \quad (5.6)$$

This number is 34% lower than the dipole moment calculated in equation 2.22. The reason for this is unknown. One hypothesis is that the mixing coefficients in equations 2.14 and 2.15 are inaccurate.

5.4 Simulations

What the procedure in section 5.2 measures is the populations of the ground and excited state, corresponding to the diagonal elements of the density matrix. What is even more interesting is the off-diagonal elements, because that is what determines the extent to which the atoms were magnetized. In order to infer the off-diagonal elements, a density matrix simulation was run that numerically solved the Liouville equation of motion for the density matrix with a phenomenological decay term added [63]:

$$\dot{\rho} = \frac{1}{i\hbar}[\hat{H}, \rho] - \frac{1}{2}\{\hat{\Gamma}, \rho\}, \quad (5.7)$$

where $\{\hat{\Gamma}, \rho\} = \Gamma\rho + \rho\Gamma$. The simulation assumed the measured value of the dipole moment, $0.063\mu_{\text{B}}$, and accounted for all six hyperfine levels and the 5D_0 level (meaning ρ was a 7×7 matrix). The inhomogeneous broadening was accounted for by sampling 40,000 atoms of each isotope, distributed evenly between -0.5 GHz and +0.5 GHz relative to an unshifted atom. The levels that were included in the simulation along with the relevant level spacings, detunings, and decay rates are labeled in figure 5.4.

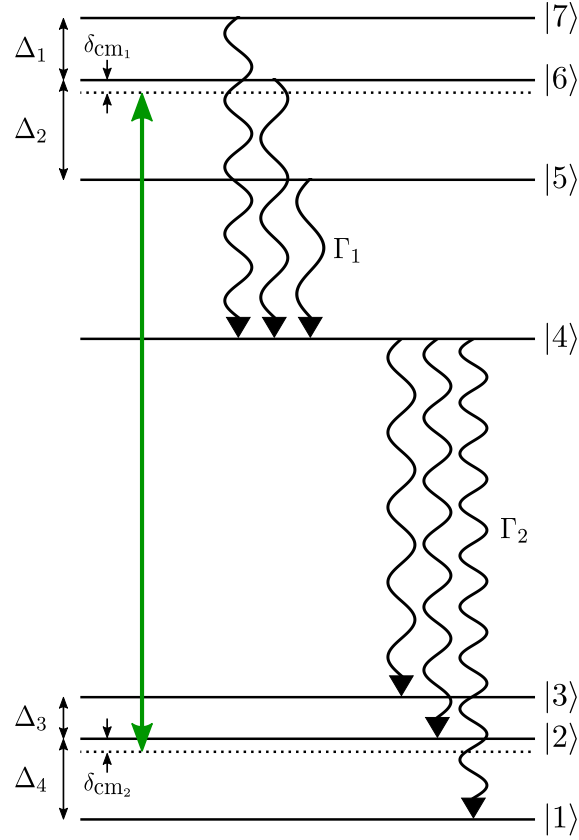


Figure 5.4: *Rabi Flopping Simulation Energy Levels*. $\Delta_1 = 114$ MHz, $\Delta_2 = 183$ MHz, $\Delta_3 = 76.4$ MHz, $\Delta_4 = 148.1$ MHz, $\delta_{cm_1} = 23$ MHz, $\delta_{cm_2} = 24$ MHz, $\Gamma_1 = 30.3$ s $^{-1}$, $\Gamma_2 = 621$ s $^{-1}$

The hamiltonian for this simulation looks like this:

$$\begin{pmatrix} \hbar\omega_1 & 0 & 0 & 0 & -\mu_{15}B & -\mu_{16}B & -\mu_{17}B \\ 0 & \hbar\omega_2 & 0 & 0 & -\mu_{25}B & -\mu_{26}B & -\mu_{27}B \\ 0 & 0 & \hbar\omega_3 & 0 & -\mu_{35}B & -\mu_{36}B & -\mu_{37}B \\ 0 & 0 & 0 & \hbar\omega_4 & 0 & 0 & 0 \\ -\mu_{51}B & -\mu_{52}B & -\mu_{53}B & 0 & \hbar\omega_5 & 0 & 0 \\ -\mu_{61}B & -\mu_{62}B & -\mu_{63}B & 0 & 0 & \hbar\omega_6 & 0 \\ -\mu_{71}B & -\mu_{72}B & -\mu_{73}B & 0 & 0 & 0 & \hbar\omega_7 \end{pmatrix}, \quad (5.8)$$

where each B is really assumed to be $\frac{B}{2}(e^{i\omega_0 t} + e^{-i\omega_0 t})$. Equation 5.8 can be transformed to the interaction picture using

$$U = \begin{pmatrix} e^{i\omega_1 t} & 0 & 0 & 0 & 0 & 0 & 0 \\ 0 & e^{i\omega_2 t} & 0 & 0 & 0 & 0 & 0 \\ 0 & 0 & e^{i\omega_3 t} & 0 & 0 & 0 & 0 \\ 0 & 0 & 0 & e^{i\omega_4 t} & 0 & 0 & 0 \\ 0 & 0 & 0 & 0 & e^{i\omega_5 t} & 0 & 0 \\ 0 & 0 & 0 & 0 & 0 & e^{i\omega_6 t} & 0 \\ 0 & 0 & 0 & 0 & 0 & 0 & e^{i\omega_7 t} \end{pmatrix} \quad (5.9)$$

and the unitary transformation

$$\hat{H} = U H U^\dagger + i\hbar U \frac{dU^\dagger}{dt}. \quad (5.10)$$

After making this transformation all of the diagonal elements will be zero and each off diagonal element will be multiplied by $(e^{i\omega_0 t} + e^{-i\omega_0 t})e^{i(\omega_i - \omega_j)t}$, where i and j refer to whatever two levels are relevant to that particular off diagonal element H_{ij} . Once these exponential terms are multiplied out, there should be a term that oscillates on the order of 2ω and a term that oscillates on the order of a detuning. The terms that rotate at $\sim 2\omega$ can be set to zero because their fast rotation will average to zero. This is the rotating wave approximation. The final hamiltonian is this:

$$\begin{pmatrix} 0 & 0 & 0 & 0 & -\frac{\Omega_{15}}{2}e^{-i\Delta_{15}t} & -\frac{\Omega_{16}}{2}e^{-i\Delta_{16}t} & -\frac{\Omega_{17}}{2}e^{-i\Delta_{17}t} \\ 0 & 0 & 0 & 0 & -\frac{\Omega_{25}}{2}e^{-i\Delta_{25}t} & -\frac{\Omega_{26}}{2}e^{-i\Delta_{26}t} & -\frac{\Omega_{27}}{2}e^{-i\Delta_{27}t} \\ 0 & 0 & 0 & 0 & -\frac{\Omega_{35}}{2}e^{-i\Delta_{35}t} & -\frac{\Omega_{36}}{2}e^{-i\Delta_{36}t} & -\frac{\Omega_{37}}{2}e^{-i\Delta_{37}t} \\ 0 & 0 & 0 & 0 & 0 & 0 & 0 \\ -\frac{\Omega_{51}}{2}e^{i\Delta_{51}t} & -\frac{\Omega_{52}}{2}e^{i\Delta_{52}t} & -\frac{\Omega_{53}}{2}e^{i\Delta_{53}t} & 0 & 0 & 0 & 0 \\ -\frac{\Omega_{61}}{2}e^{i\Delta_{61}t} & -\frac{\Omega_{62}}{2}e^{i\Delta_{62}t} & -\frac{\Omega_{63}}{2}e^{i\Delta_{63}t} & 0 & 0 & 0 & 0 \\ -\frac{\Omega_{71}}{2}e^{i\Delta_{71}t} & -\frac{\Omega_{72}}{2}e^{i\Delta_{72}t} & -\frac{\Omega_{73}}{2}e^{i\Delta_{73}t} & 0 & 0 & 0 & 0 \end{pmatrix}, \quad (5.11)$$

where $\Delta_{ij} = \Delta_{ji}$, and each detuning can be defined as:

$$\begin{aligned}
\Delta_{51} &= (\Delta_2 - \delta_{cm_1}) - (\Delta_4 - \delta_{cm_2}) + \Delta_0 \\
\Delta_{61} &= -\delta_{cm_1} - (\Delta_4 - \delta_{cm_2}) + \Delta_0 \\
\Delta_{71} &= -(\Delta_1 + \delta_{cm_1}) - (\Delta_4 - \delta_{cm_2}) + \Delta_0 \\
\Delta_{52} &= (\Delta_2 - \delta_{cm_1}) - (-\delta_{cm_2}) + \Delta_0 \\
\Delta_{62} &= -\delta_{cm_1} - (-\delta_{cm_2}) + \Delta_0 \\
\Delta_{72} &= -(\Delta_1 + \delta_{cm_1}) - (-\delta_{cm_2}) + \Delta_0 \\
\Delta_{53} &= (\Delta_2 - \delta_{cm_1}) - (-\Delta_3 + \delta_{cm_2}) + \Delta_0 \\
\Delta_{63} &= -\delta_{cm_1} - (-\Delta_3 + \delta_{cm_2}) + \Delta_0 \\
\Delta_{73} &= -(\Delta_1 + \delta_{cm_1}) - (-\Delta_3 + \delta_{cm_2}) + \Delta_0 .
\end{aligned}$$

All of the frequency spacings are labeled in figure 5.4, and Δ_0 is the overall shift of the ground level and the excited level. Each different Δ_0 represents a different atom within the inhomogeneous broadening.

The decay can be accounted for using the matrix

$$\begin{pmatrix}
0 & 0 & 0 & 0 & 0 & 0 & 0 \\
0 & 0 & 0 & 0 & 0 & 0 & 0 \\
0 & 0 & 0 & 0 & 0 & 0 & 0 \\
0 & 0 & 0 & \Gamma_2 & 0 & 0 & 0 \\
0 & 0 & 0 & 0 & \Gamma_1 & 0 & 0 \\
0 & 0 & 0 & 0 & 0 & \Gamma_1 & 0 \\
0 & 0 & 0 & 0 & 0 & 0 & \Gamma_1
\end{pmatrix} . \tag{5.12}$$

The upper three levels all decay to the 5D_0 and from there decay evenly to the 7F_0 levels. The system is solved by plugging the Hamiltonian (equation 5.11) and the decay matrix (equation 5.12) into equation 5.7 and using a 4th order Runge-Kutta method as described in appendix C. The results of the figures are shown in figure 5.5.

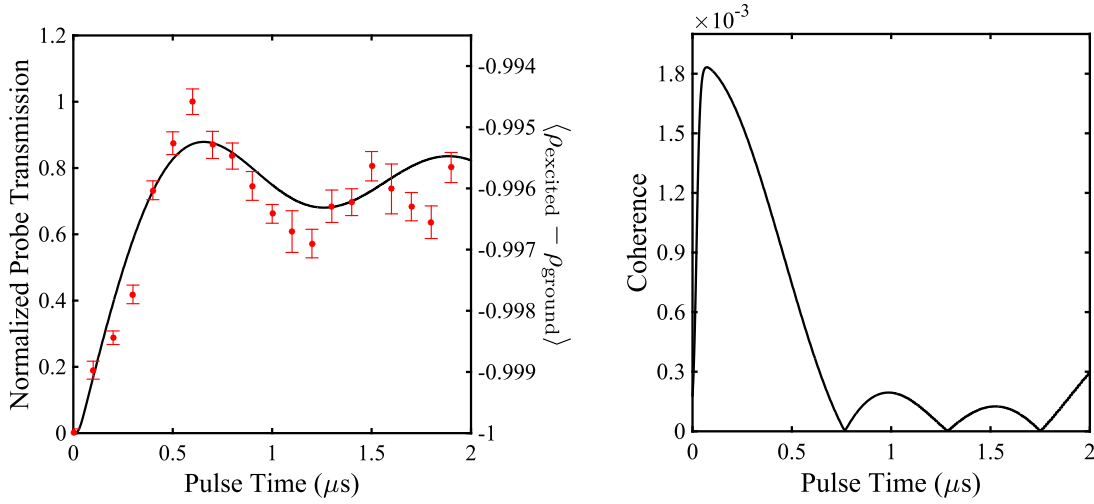


Figure 5.5: *Simulation Results*. The diagonal matrix elements are plotted in the left graph and the off diagonal elements are plotted in the right graph. The maximum coherence achieved is 1.83×10^{-3} .

The fact that the contrast and the time of maximum probe transmission agree with each other allow the coherence to be confidently inferred. The reason that the population difference never gets above zero is because all the atoms are accounted for when determining the population and the atoms outside of the linewidth of the laser are hardly effected and therefore remain in the ground state.

5.5 Magnetization, Susceptibility, and Comments on Negative Index

5.5.1 Magnetization

In order to see the significance of these results, they need to be looked at in terms of magnetization and susceptibility. Magnetization is a dipole moment per volume is calculated from

$$M = N\mu\langle\hat{\rho}_{\text{off-diagonal}}\rangle, \quad (5.13)$$

where N is the density, μ is the dipole moment, and $\langle\hat{\rho}_{\text{off-diagonal}}\rangle$ is the ensemble-averaged coherence. The dipole moment and maximum coherence were found in the previous section. The density can be calculated as follows. The Y_2SiO_5 crystal is doped with 0.1% europium. The molar

mass of each element is

$$\begin{aligned} \text{Y} &= 88.9 \frac{\text{g}}{\text{mol}} \\ \text{Si} &= 28.09 \frac{\text{g}}{\text{mol}} \\ \text{O} &= 16 \frac{\text{g}}{\text{mol}} \end{aligned}$$

giving a total molar mass of

$$2(88.9) + (28.09) + 5(16) = 285.89 \frac{\text{g}}{\text{mol}}. \quad (5.14)$$

Scientific Materials quotes the density of YSO as 4.44 g/cm^3 . Using this and the total mass from 5.14 the density can be calculated:

$$\begin{aligned} N &= \left(6.022 \times 10^{23} \frac{\#}{\text{mol}} \right) \times \left(\frac{1 \text{ mol}}{285.9 \text{ g}} \right) \times \\ &\quad \left(4.44 \frac{\text{g}}{\text{cm}^3} \right) \times \underbrace{(0.001)}_{\substack{\text{Eu}^{3+} \\ \text{concentration}}} \times \left(\frac{100 \text{ cm}}{1 \text{ m}} \right)^3 = 9.35 \times 10^{24} \text{ m}^{-3}. \end{aligned} \quad (5.15)$$

The maximum magnetization, from equation 5.13, is found to be

$$\begin{aligned} M &= (9.35 \times 10^{24} \text{ m}^{-3})(0.063) \left(9.274 \times 10^{-24} \frac{\text{J}}{\text{T}} \right) (1.83 \times 10^{-3}) \\ M &= 0.01 \frac{\text{A}}{\text{m}}. \end{aligned} \quad (5.16)$$

The magnetization produced by this interaction is small compared to permanent magnets, which can have a magnetization of hundreds of thousands to one million amps per meter. A good comparison is that it has the same magnetization of a one cm^2 loop of wire with 1 mA of current oscillating back and forth. This is not out of the ordinary in electronics where the current might be oscillating back and forth at kilohertz or megahertz frequencies. The remarkable thing about this magnetization is that it is oscillating at the optical frequency of the ${}^7F_0 \rightarrow {}^5D_1$ transition, 568.7 terahertz.

5.5.2 Susceptibility

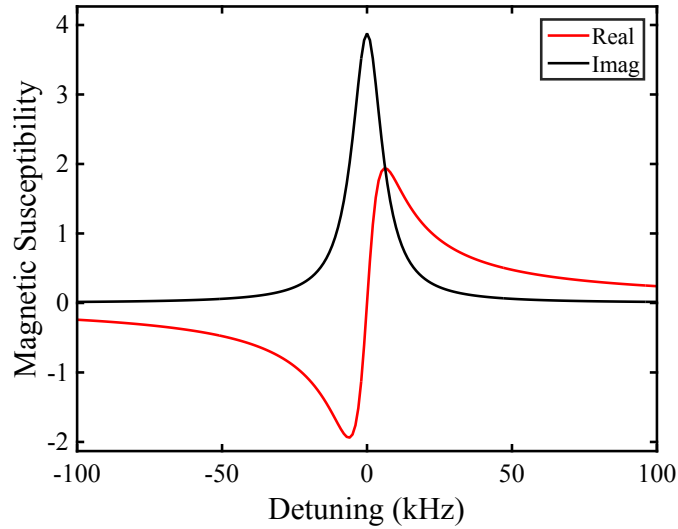


Figure 5.6: *Susceptibility of Homogeneous Broadening.*

The susceptibility of a magnetic dipole transition is given by equation 1.17 but is repeated here for convenience:

$$\chi_M = \frac{N\mu_0\mu^2}{\hbar(\Delta\omega - i\gamma)}, \quad (5.17)$$

where N is the density, μ_0 is the permeability of free space, μ is the magnetic dipole moment of the transition, $\Delta\omega$ is the detuning from resonance, and γ is the total linewidth of the transition, determined in equation 2.13. The homogeneous susceptibility is plotted in figure 5.6. The measured absorption in figure 2.8 can be fit to an equation of the following form:

$$A = e \left(-\frac{A}{\pi g (f - f_0)^2 + g^2} \right), \quad (5.18)$$

where A is a fitting parameter to get the correct amplitude, f is the laser frequency in hertz, f_0 is the center frequency of the transition, and the FWHM in hertz is $2g$. This equation accounts for any saturation that might be happening. From the fit to equation 5.18, the FWHM is found to be 1.6 GHz.

The total susceptibility of the ${}^7F_0 \rightarrow {}^5D_1$ transition is found then by convolving equation 5.17 with the equation for the normalized inhomogeneous lineshape:

$$A = -\frac{1}{\pi g} \frac{g^2}{(\omega - \omega_0)^2 + g^2}, \quad (5.19)$$

where ω is an angular frequency and $g = 2\pi \times (0.8 \times 10^9)$ rad/s. The result of the convolution is shown in figure 5.7. It can be seen that the real part of χ_M , which is the part that goes into equation

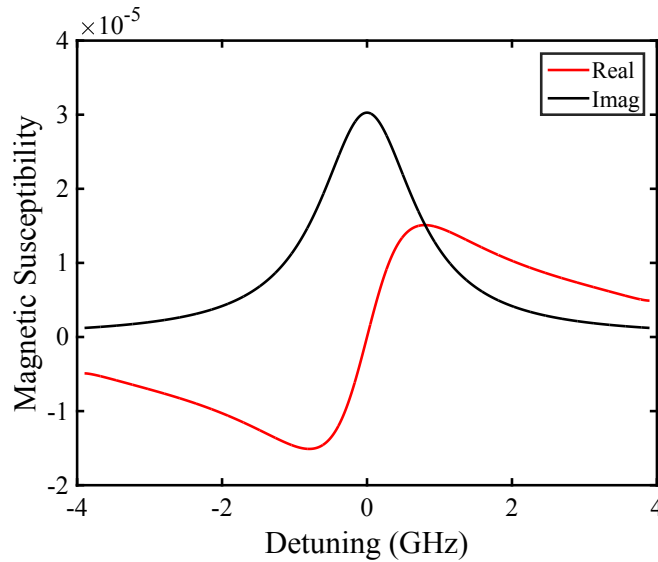


Figure 5.7: *Magnetic Susceptibility*. Susceptibility of the ${}^7F_0 \rightarrow {}^5D_1$ transition.

1.19b, is far from the negative value that is needed in order to achieve a negative permeability.

When Larry Alegria from Scientific Materials was asked in an email about the error bars on the dopant concentration of the YSO crystal, he replied that the “amount of error is difficult to say since there are not established standards”. The meaning of this is unclear, but raises our suspicions about the actual density of europium in the crystal. The measured absorption (figure 2.8) can be compared with Beer’s Law:

$$\frac{I}{I_0} = e^{-2\frac{\omega}{c} \text{Im}[n]L}, \quad (5.20)$$

where

$$n = \sqrt{\epsilon\mu} \quad (5.21)$$

$$n = \sqrt{1 + \chi_E} \sqrt{1 + \chi_M} \quad (5.22)$$

$$n \approx n_0 \left(1 + \frac{1}{2} \chi_M \right), \quad (5.23)$$

and so

$$\text{Im}[n] = \text{Im} \left[\frac{n_0}{2} \chi_M \right], \quad (5.24)$$

where $n_0 = 1.8$ and χ_M is the susceptibility shown in figure 5.7. If the density was a factor of four larger, the measured and predicted peak absorptions would match precisely. Because of this, and the seemingly large uncertainty that Scientific Materials might have in the density, it is not unreasonable to assume the density is higher than the request value. The susceptibilities shown in figures 5.6 and 5.7 have been corrected to assume this higher density. If this density correction is valid, the maximum magnetization inferred in equation 5.16 could be a factor of four higher.

5.5.3 Left-Handed Waves

As seen in the previous section, this experiment is a long way from producing a true negative permeability and therefore a true negative index. Finding a stronger dipole moment, or using a crystal doped with a higher percentage of europium are examples of ways to increase the susceptibility. However, our recently proposed scheme, detailed in chapter 3, *would* be able generate a detectable amount of left-handed light with this amount of magnetization.

If the magnetization generated in the Rabi flopping experiment is assumed to be the limiting factor, the intensity of left-handed waves generated can be calculated using equations 3.3, 5.4, and 5.13 as follows. First the magnitude of the B -field can be found:

$$B = \frac{\mu_0 M}{2}, \quad (5.25)$$

and then find the corresponding intensity:

$$\begin{aligned}
 I &= \frac{c}{2n\mu_0} B^2 \\
 I &= \frac{c}{2n\mu_0} \left(\frac{\mu_0 M}{2} \right)^2 \\
 I &= \frac{\mu_0 c}{8n} M^2. \tag{5.26}
 \end{aligned}$$

As an added confirmation, the polarization required by equation 3.5 can be found:

$$P = M \frac{n^2 + 1}{2cn} \tag{5.27}$$

and plugged into equation 3.2:

$$\begin{aligned}
 E &= \frac{P}{\epsilon_0(n^2 + 1)} \\
 E &= \frac{M}{2cn\epsilon_0}. \tag{5.28}
 \end{aligned}$$

Finally, this can be plugged into the intensity equation:

$$\begin{aligned}
 I &= \frac{cn\epsilon_0}{2} E^2 \\
 I &= \frac{cn\epsilon_0}{2} \left(\frac{M}{2cn\epsilon_0} \right)^2 \\
 I &= \frac{1}{8cn\epsilon_0} M^2 \\
 I &= \frac{\mu_0 c}{8n} M^2, \tag{5.29}
 \end{aligned}$$

where in the last line the fact that $c = 1/\epsilon_0\mu_0$ is used. The intensity of an electromagnetic wave should not depend on whether the E - or B -field is used to calculate it, so the fact that equations 5.26 and 5.29 match is not surprising, but is reassuring.

If it is assumed that $M = 0.01$ A/m and $n = 1.8$, a polarization of 3.93×10^{-11} C/m² is required in order to drive a left-handed wave. That resulting left-handed wave would have an intensity of 261.6 nW/cm². Although this is a very small intensity, it is measurable. With a good experimental design and with the use of photon counters, an extraordinarily small amount of left-handed light should still be detectable.

Chapter 6

Future Improvements and Experiments

6.1 Spectral Hole Burning

The Rabi signals shown in figure 5.3 dephase very quickly, only allowing observation of one cycle or so. This is partly due to the fact that the experiment was performed on an inhomogeneous linewidth. Since the hyperfine level spacings of the ${}^7F_0 \rightarrow {}^5D_1$ transition (shown in figure 2.7) are less than the inhomogeneous linewidth, a laser that is resonant with one ground to excited state transition is resonant with all combinations of ground to excited state transition.

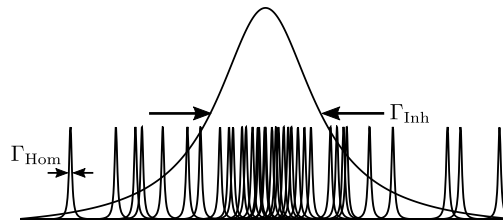


Figure 6.1: *Inhomogeneous Linewidth vs Homogeneous Linewidth.* The inhomogeneous linewidth is comprised of a bunch of homogeneous linewidths that have been shifted different amounts by the inhomogeneous electric field in the crystal. For the ${}^7F_0 \rightarrow {}^5D_1$ transition, $\Gamma_{\text{Inh}} = 2\pi \times 1.6 \text{ GHz}$ and $\Gamma_{\text{Hom}} = 2\pi \times 6.2 \text{ kHz}$.

Spectral hole burning is a way to select a single class of ion from an inhomogeneous broadening. Good descriptions of spectral hole burning are given in references [58], [64], and [29]. For simplicity, assume there are two ground states and two excited states. The situation is illustrated in figure 6.2. If a weak probe beam scans over the hyperfine structure without disrupting any of the populations, the absorption spectrum should look flat because at every frequency the laser will be

resonant with some atom in the inhomogeneous broadening. If a ‘pump’ laser that is resonant with the lower ground state and lower excited state is shined on the sample, eventually all of the atoms are pumped out of the lower ground level and end up in the upper ground level.

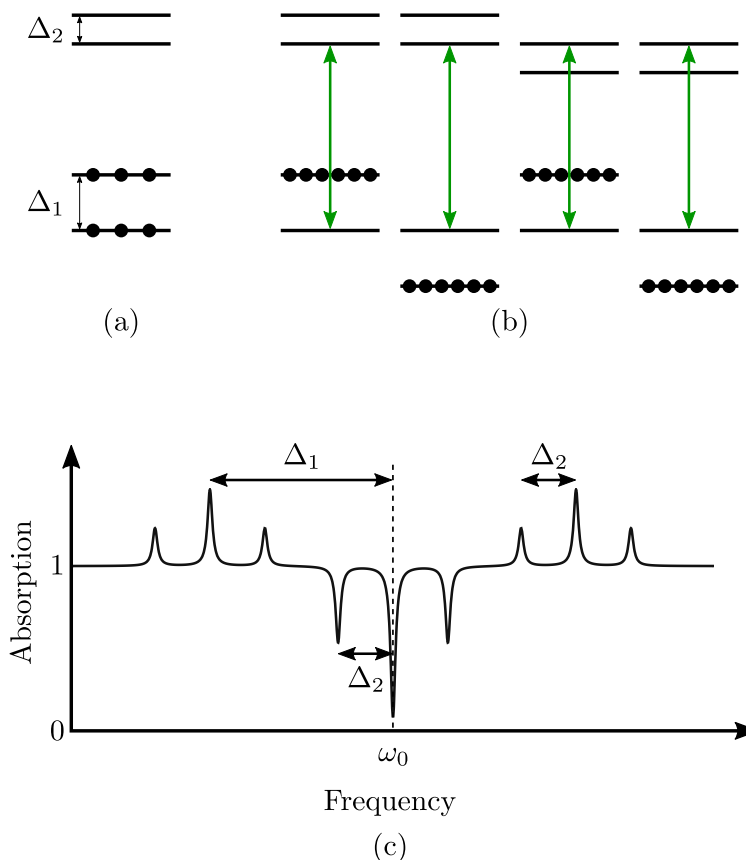


Figure 6.2: *Simplified Spectral Hole Burning*. (a) The atoms begin evenly distributed between the hyperfine levels. (b) A laser with frequency ω_0 , resonant with all combinations of ground and excited state, pumps each atom into one hyperfine level. (c) When a weak probe is scanned over the entire inhomogeneous broadening, a series of holes and antiholes are observed.

But since the inhomogeneous broadening is much wider than the hyperfine levels, every combination of ground to excited state is resonant and each of these resonant atoms is pumped into a single ground hyperfine level. This situation is illustrated in figure 6.2(b). Now when a weak probe is scanned over the inhomogeneous broadening, there is a region of decreased absorption (a

‘spectral hole’) at ω_0 where all of the atoms have been pumped to the other hyperfine level. Additionally, there are areas of increased absorption (‘antiholes’) where population has accumulated in the hyperfine level not resonant with the pump laser. Figure 6.2(c) shows the hole and antiholes produced by pumping the atom shown in (a) and (b). In the ideal case the spectral hole could be as narrow as twice the homogeneous linewidth.

In reality, the ${}^7F_0 \rightarrow {}^5D_1$ transition has three ground states and three excited states, so if a spectral hole is created like the one shown in figure 6.2, there are many holes and antiholes. All of the possible spectral holes are shown in figure 6.3. This was generated using Matlab and assumed that each transition is equally likely. In reality there is a distribution of dipole matrix elements between each ground and excited state, so the relative heights between the holes and antiholes could be significantly different.

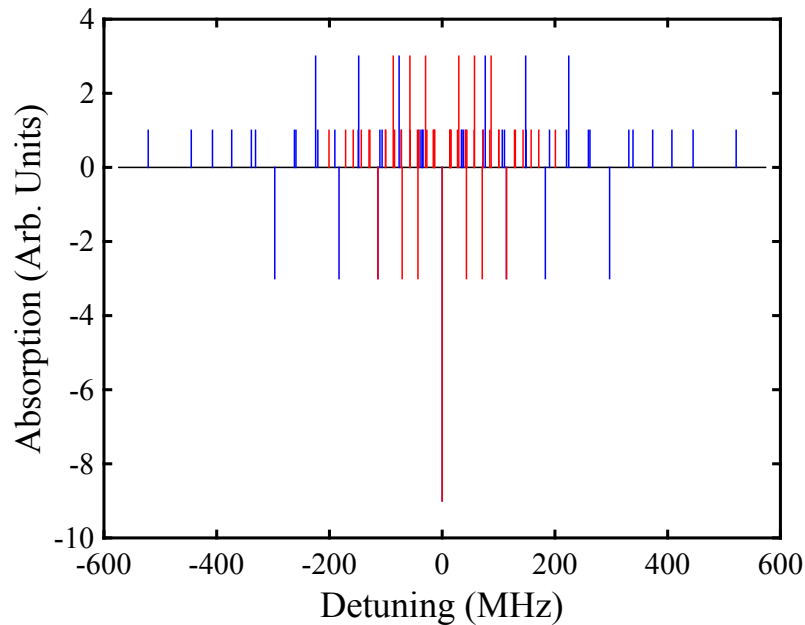


Figure 6.3: *All Possible Spectral Holes and Antiholes.* This is all of the possible spectral holes and antiholes from burning at a single frequency within the ${}^7F_0 \rightarrow {}^5D_1$ transition. Some holes and antiholes are very closely spaced and therefore there are many more features present than are actually visible in this illustration. The blue lines are the spectral features due to Eu-153 and the red are due to Eu-151.

The fact that spectral hole burning is possible can be exploited to work with a single class of ion. This process is illustrated in figure 6.4. References [64] and [29] have more details on the exact pulse sequences used to backburn a peak in order to perform an experiment on a single ion class.

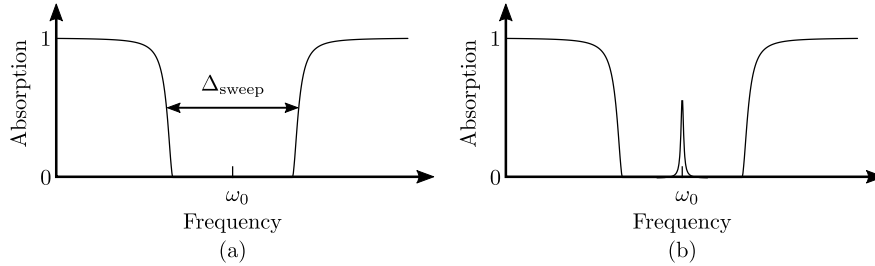


Figure 6.4: *Spectral Pit with Backburned Peak*. (a) First a laser with a center frequency ω_0 is swept over a range Δ_{sweep} in order to clear out all ions in the vicinity of the hyperfine level of interest. (b) An antihole is ‘backburned’ into the spectral pit by briefly shining lasers resonant with the other two hyperfine levels.

Another noteworthy item is that a significant narrowing of the spectral hole linewidth of the ${}^7F_0 \rightarrow {}^5D_0$ transition occurs when a strong magnetic field (~ 0.1 T) is applied [27]. We have observed spectral hole narrowing on the ${}^7F_0 \rightarrow {}^5D_1$ transition in the presence of strong rare-earth magnets with a field on the order of 0.1 T, although our understanding is limited. The current thought is that each hyperfine level is split slightly due to the Earth’s magnetic field. If Earth’s field is not cancelled, this splitting is just seen as a widening of spectral features due to an inability to resolve the split levels. By applying a strong magnetic field, the hyperfine levels split further, allowing a single narrow spectral hole to be observed. This has the disadvantage though of increasing the number of levels involved from three ground levels and three excited levels to six ground levels and six excited levels. If this is true a similar spectral hole narrowing should be observed with a magnetic field that acts to cancel out the Earth’s field. Reference [65] also discusses how spectral hole width depends on an external magnetic field.

Preliminary spectral hole burning experiments have been done, some results are shown in figures 6.5, 6.6, and 6.7. However, there is still a lot of work to be done quantifying our techniques;

knowing what intensities and what burn times produce what size spectral holes, perfecting pulse sequences to get a single narrow ion class, and understanding fully the impact an external magnetic field has on the ions.

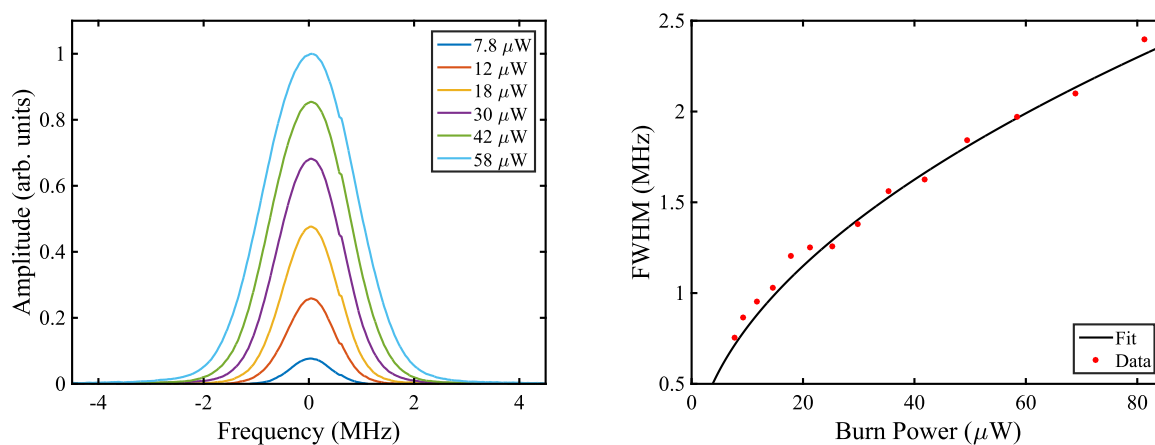


Figure 6.5: *Spectral Holes with Varying Burn Powers.* For a fixed pulse time and beam size, several different powers are used to burn a spectral hole. It is seen that $\text{FWHM} \propto \sqrt{I}$, consistent with reference [58].

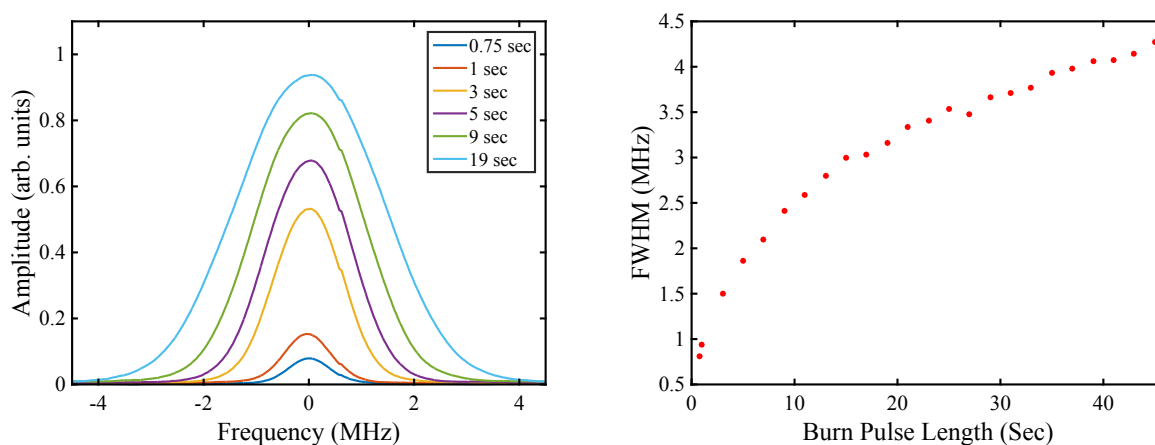


Figure 6.6: *Spectral Holes with Varying Burn Times.* For a fixed pulse power and beam size, several different pulse times are used to burn a spectral hole.

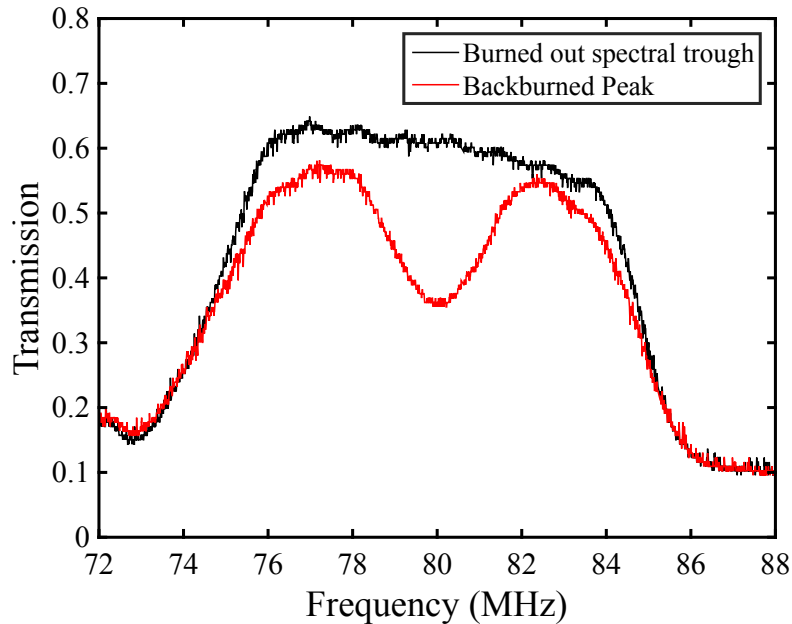


Figure 6.7: *Backburned Peak Data*. An example of a spectral pit with a backburned peak. This data shows transmission as opposed to absorption because what is actually measured in the lab is how much probe beam gets through the crystal.

6.2 Inhomogeneous Linewidth Suppression

If the inhomogeneous linewidth could be narrowed, all else staying the same, the effective density of the atoms could be dramatically increased because the laser could interact with more atoms at once. One way our group has proposed to do this is detailed in reference [66]. In short, with appropriately spaced energy levels, it would be possible to shift the inhomogeneously broadened atoms back into a nearly-homogeneous linewidth by exploiting the Stark shift.

This idea was preceded by experiments done by Cohen-Tannoudji where similar ideas are used to narrow the linewidth of a Doppler broadened emission spectrum [67][68]. Our idea is an extension of this where the coherence due to excitation from the ground level is studied. In this scheme, a four-level system interacts with two fields and is shown in figure 6.8. The two lasers used are a probe beam (E_P) and an intense beam (E_S) used to Stark shift the ground level, $|1\rangle$.

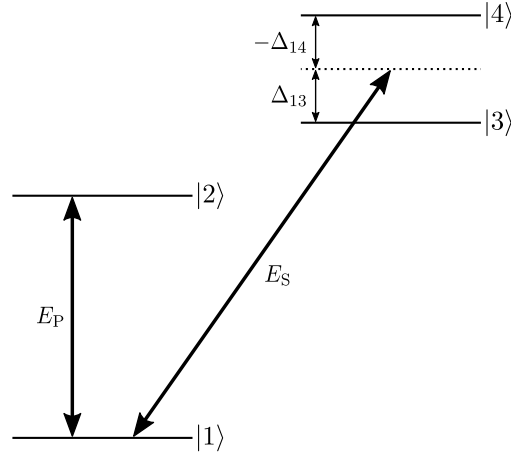


Figure 6.8: *Inhomogeneous Linewidth Suppression Scheme Level Diagram.*

The $|1\rangle \rightarrow |2\rangle$ transition is inhomogeneously broadened and a laser that connects level $|1\rangle$ to the two upper levels, $|3\rangle$ and $|4\rangle$, utilizes the Stark shift to narrow this broadening. The Rabi frequency of each laser is defined as $\Omega_{ij} = \frac{d_{ij}E}{\hbar}$ and detunings are defined to be positive when the laser is tuned above the relevant transition. The subscripts ij refer to the ground and excited levels, and d_{ij} is the electric dipole matrix element of the transition. Since the Stark laser, E_S , interacts with both $|3\rangle$ and $|4\rangle$, the ground level is shifted by an amount

$$\delta_{\text{Stark}} = \frac{|\Omega_{13}|^2}{4\Delta_{13}} + \frac{|\Omega_{14}|^2}{4\Delta_{14}}, \quad (6.1)$$

where the detunings Δ_{13} and Δ_{14} are labeled in figure 6.8. Equation 6.1 is valid in the perturbative limit that most of the population remains in the ground state. To simplify the simulations, it is assumed that $d_{13} = d_{14}$ and therefore that $\Omega_{13} = \Omega_{14} \equiv \Omega_S$.

The inhomogeneous broadening will be discussed in terms of Doppler broadening here, but this scheme applies equally well to inhomogeneous broadenings in other situations, such as strain broadening in rare-earth doped crystals. The frequency of the Stark laser is chosen so that when the atoms have zero velocity, $|\Delta_{13}| = |\Delta_{14}| \equiv \Delta_S$, and therefore according to equation 6.1, the ground level is unchanged ($\delta_{\text{Stark}} = 0$). When an atom is moving with a speed v along the propagation direction of the probe beam, the atom sees the probe beam's frequency shifted by an amount $k_p v$, where k_p is the wavenumber. If the Stark laser, with a wavenumber k_S , propagates

in the same direction as the probe laser, the atoms see a frequency shift of $k_S v$ and equation 6.1 becomes

$$\delta_{\text{Stark}} = \frac{|\Omega_S|^2}{4(\Delta_S + k_S v)} + \frac{|\Omega_S|^2}{4(-\Delta_S + k_S v)}. \quad (6.2)$$

If $|k_S v| \ll \Delta_S$ this becomes

$$\delta_{\text{Stark}} \approx -\frac{|\Omega_S|^2}{2\Delta_S} k_S v. \quad (6.3)$$

In order for this stark shift to exactly compensate the Doppler shift seen by the $|1\rangle \rightarrow |2\rangle$ transition, it must be the case that

$$\delta_{\text{Stark}} = -k_P v. \quad (6.4)$$

This can be plugged into equation 6.3 and the result is

$$\frac{k_P}{k_S} = \frac{|\Omega_S|^2}{2\Delta_S^2}. \quad (6.5)$$

Although equation 6.5 shows that it is possible to cancel the doppler shift in the perturbative limit, further investigation requires numerical methods. The reason for this is the high intensity of Stark laser required to carry out an experiment. If the probe and Stark beams are assumed to be in the optical region of the spectrum, it will be the case that k_P is on the same order of magnitude as k_S . If this is the case, it must also be the case that Ω_S is on the same order of magnitude as Δ_S . This would result in significant population transfer to levels $|3\rangle$ and $|4\rangle$ and the perturbative limit would no longer be valid.

6.2.1 Simulations

In order to simulate the system shown in figure 6.8, the density matrix equation of motion, equation 5.7, was solved numerically. The hamiltonian of the system, using the rotating wave approximation and the interaction picture, is

$$H = \hbar \begin{pmatrix} 0 & -\frac{\Omega_P}{2} & -\frac{\Omega_{31}}{2} & -\frac{\Omega_{41}}{2} \\ -\frac{\Omega_P}{2} & \delta_{12} & 0 & 0 \\ -\frac{\Omega_{13}}{2} & 0 & \Delta_{13} & 0 \\ -\frac{\Omega_{14}}{2} & 0 & 0 & \Delta_{14} \end{pmatrix}, \quad (6.6)$$

where Ω_P is the Rabi frequency of the probe beam and $\Omega_{ij} = \Omega_{ji}$. The decay matrix, Γ is

$$\begin{pmatrix} 0 & 0 & 0 & 0 \\ 0 & \Gamma_1 & 0 & 0 \\ 0 & 0 & \Gamma_2 & 0 \\ 0 & 0 & 0 & \Gamma_3 \end{pmatrix}. \quad (6.7)$$

It is assumed that $\Gamma_1 = \Gamma_2 = \Gamma_3 \equiv \Gamma$. The decay rate was set at $\Gamma = 2\pi \times 5$ MHz and the probe intensity was set at $\Omega_P = \Gamma/100$. The simulation was run assuming all of the population began in state $|1\rangle$. The coherence of the $|1\rangle \rightarrow |2\rangle$ transition is shown in figure 6.9a with no inhomogeneous broadening applied. An inhomogeneous broadening of $\Delta\omega_{\text{Doppler}} = 2\pi \times 250$ MHz is then imposed

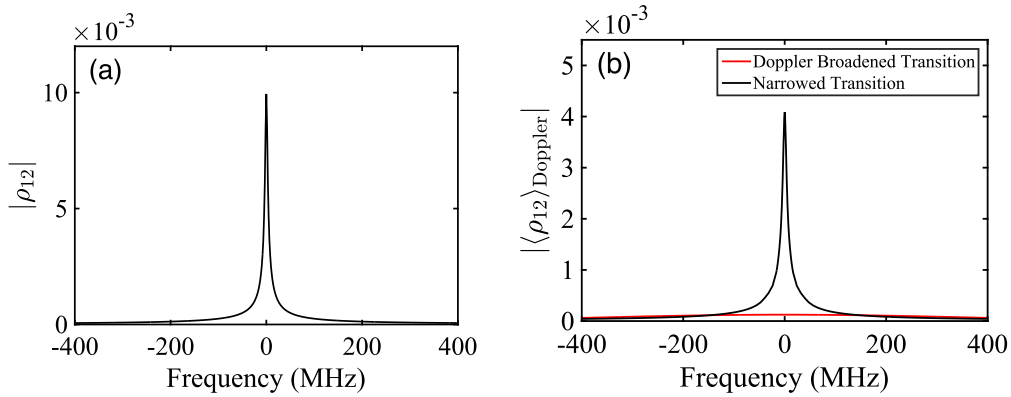


Figure 6.9: *Suppression of Inhomogeneous Linewidth.* (a) The $|1\rangle \rightarrow |2\rangle$ transition with no broadening applied. The peak coherence is 1×10^{-2} . (b) The $|1\rangle \rightarrow |2\rangle$ transition after it is inhomogeneously broadened (red line) and after the Stark laser is turned on (black line). The peak coherence of the broadened line is 1.25×10^{-4} and is restored to 4.1×10^{-3} after the Stark laser is turned on.

on the transition (shown by the red line in 6.9b). As the line is broadened, the coherence drops almost an order of magnitude to 1.25×10^{-4} . After the line is broadened, applying the Stark laser restores the coherence to 4.1×10^{-3} .

Next it is interesting to find the optimal intensity of the Stark laser. The simulation assumes that levels $|3\rangle$ and $|4\rangle$ are separated by 2000Γ , meaning $\Delta_S = 1000\Gamma$. It is also assumed that $k_S = 4k_P$.

From equation 6.5 this means that in order to get perfect suppression

$$\begin{aligned}\frac{\Omega_S^2}{2\Delta_S^2} &= \frac{k_P}{k_S} \\ \Omega_S^2 &= 2\Delta_S^2 \frac{k_P}{k_S} \\ \Omega_S &= \frac{\Delta_S}{\sqrt{2}} \\ \Omega_S &= 707\Gamma.\end{aligned}\tag{6.8}$$

As the Rabi frequency of the Stark laser was varied it was found that the actual optimal coherence

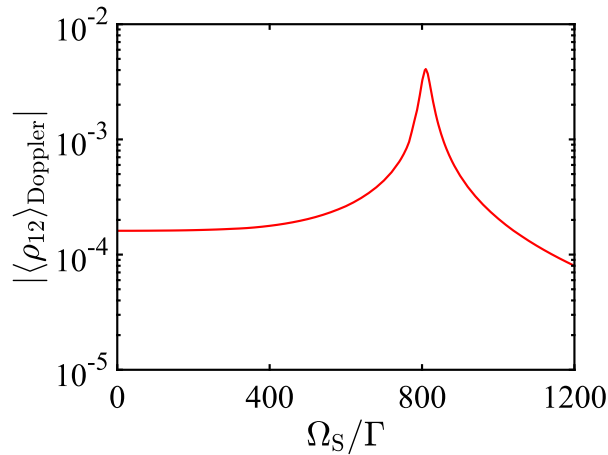


Figure 6.10: *Optimal Stark Laser Strength*. The peak value of the restored coherence as the Stark laser Rabi frequency is increased. The highest coherence achieved occurs when $\Omega_S = 810\Gamma$. For other values of Ω_S the Doppler shift is either over- or under-compensated for. The simulation in figure 6.9b used this peak value of Ω_S .

occurred when $\Omega_S = 810\Gamma$, as seen in figure 6.10. The discrepancy between these two numbers is most likely due to a breakdown of the perturbative approximation used to get equation 6.5.

Lastly, the optimal ratio of k_P/k_S is determined. The result is shown in figure 6.11. In order to find the optimal ratio of wavenumbers, the ratio of k_S/k_P was varied and for each value of k_S/k_P , a plot like the one shown in figure 6.10 was generated to get the optimal value of Ω_S . After the

optimal Rabi Frequency for the Stark laser was determined, the peak coherence of the probe beam on resonance was found. As shown in figure 6.11, the optimal wavenumber ratio is $k_S/k_P = 4$.

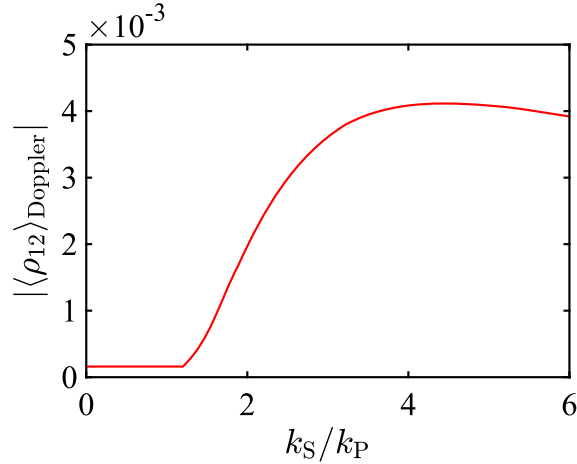


Figure 6.11: *Optimal k_S/k_P Ratio.*

6.3 Electromagnetically Induced Transparency

After spectral hole burning is thoroughly understood and narrow populations can be created, an exciting experiment to do will be to see electromagnetically induced transparency (EIT) on the ${}^7F_0 \rightarrow {}^5D_1$ transition. EIT has been performed by several groups on transitions in rare-earth doped crystals, but never on a magnetic dipole transition [69][70][71][72].

Qualitatively, EIT is when a three level system interacts with two laser beams in such a way that the medium is transparent to both beams. In certain situations, in the frequency region where transparency occurs the real part of the susceptibility can have a very steep slope allowing for slow and stopped light experiments. EIT is possible with several different level schemes, but only the so-called Λ -scheme will be discussed here. A Λ -scheme is comprised of two ground levels, each of which is connected to the same excited state. In order to achieve this in a europium ion, three laser beams are needed; two to create the Λ -scheme and one as a repump to pump population back out of the third unused ground level, as shown in figure 6.12. It is important to note that because the ordering of the hyperfine levels of the 5D_1 level are not known, the repump laser needs to be

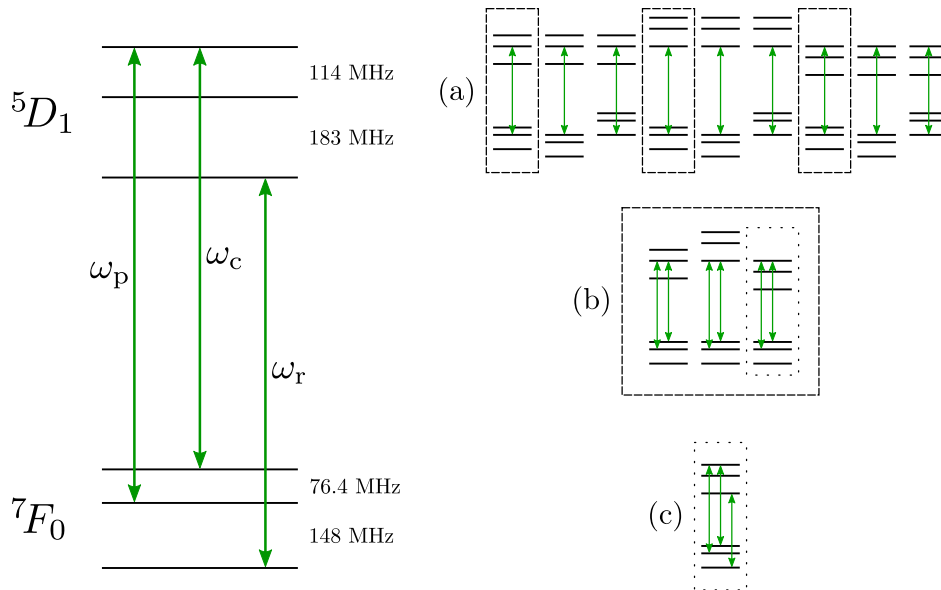


Figure 6.12: *EIT Laser Scheme*. The proposed EIT Λ -scheme and repump beam configuration is shown on the left. The three beams are labeled the probe (ω_p), control (ω_c), and repump (ω_r). (a) If one laser is shined into the inhomogeneous broadening, it is resonant with every combination of ground to excited state transitions. (b) If the ground states of the Λ -scheme are chosen to be the upper two hyperfine ground states, the ions in the dashed boxes are all still resonant. (c) If the first two lasers pump all of the population into the third yet-unused ground state, it is possible now to select a single ion class by pumping with a laser that connects the third ground state to one of the unused excited states.

chosen carefully. The ordering could be what is shown in figure 6.12 or it could be that the upper splitting is 183 MHz and the lower splitting is 114 MHz. What is known however, is that the total spacing between the top level and the bottom level is 297 MHz. Because of this, it is possible to use the top and bottom levels of the 5D_1 level for the excited level in the Λ -scheme and the upper level that the repump connects to. Due to the AOMs we have, it is more convenient to use the scheme shown in figure 6.12 than to switch the excited states of the Λ -scheme and repump beam.

Chapter 7

Conclusion

Although considerable work went into what is presented here, it is only a small step in experimentally seeing left-handed light. There are still many exciting both short term and long term experiments to be done.

To our knowledge, the ordering of the 5D_1 hyperfine levels is still unknown and would be a good thing to determine and document. Along with this, measuring precisely the relative transition probabilities of each hyperfine ground to excited state would be useful. Knowing the strength of each transition would help guide choosing a Λ -scheme for EIT and would increase accuracy of future simulations. Both the ordering of the levels and the transition strengths could be measured using the techniques explained in reference [29]. By using a laser scheme like the one shown in figure 6.12, it is possible to burn out wide spectral pits (10s of MHz) and repopulate narrow populations within the pit corresponding to certain repump laser transitions. By then observing the series of spectral pits, holes, and antiholes created throughout the inhomogeneous broadening, it is possible to deduce the ordering of the upper levels based on the spacing of the spectral features and three frequencies of light being used. Similarly, the relative heights of the holes and antiholes allows the relative transition probabilities to be determined. In order to perform this experiment it is necessary to be able to sweep a laser frequency over hundreds of megahertz to observe the various holes and antiholes. It is also necessary to have good control over the intensity of all three beams and understand how much power is needed to burn and scan in order to not get a distorted spectrum.

If the inhomogeneous linewidth of the ${}^7F_0 \rightarrow {}^5D_1$ transition could be suppressed using a scheme like the one described in chapter 6, it would be hugely beneficial. The susceptibility of the transition would be more on the order of the homogeneous susceptibility (figure 5.6), and a true negative permeability could be easily achieved. If this were the case, a negative index of refraction would be realizable in an atomic system. One of the biggest differences between the scheme described in chapter 6 and the rare-earth doped crystal being used is the fact that one is Doppler broadened due to atoms moving with different velocities and one is strain broadened due to inhomogeneities in the crystal. The conclusion that the Stark laser frequency needs to be four times the probe laser frequency is a direct consequence of the fact that the Doppler shift experienced depends on wavelength ($\Delta_{\text{Doppler}} = kv$). If the inhomogeneous linewidth is due instead to variations in the electric field in the crystal, there is no dependence on the wavelength of the probe light and perhaps strong suppression can be achieved using a Stark laser closer in frequency to the probe laser. Another point of interest is that if a magnetic dipole moment is used to suppress the linewidth, it would in fact not be due to the AC Stark shift, but rather the AC Zeeman shift.

The next steps towards the long term goal of creating left-handed waves include coming up with a way to incorporate a polarization and running simulations that account for more experimental parameters. The current idea for generating a polarization is to use any nonlinearities in the YSO host crystal, as described at the end of chapter 3. Measuring $\chi^{(3)}$ in the YSO crystal would be the first step to doing this. After determining the nonlinear susceptibility of the YSO crystal and knowing the dipole moment of the ${}^7F_0 \rightarrow {}^5D_1$ transition, it should be possible to run more accurate simulations and get a better idea of the amount left-handed light that can be created. Implementing the left-handed wave scheme experimentally will be challenging, but not impossible. In order to distinguish the driving fields from the generated left-handed light, as mentioned earlier, the plan would be to drive the left-handed light with a nonlinear polarization and magnetization. That way the driving fields could be at 1055 nm and the left-handed light could be at 527.5 nm. The relative amplitudes could be controlled by exploiting the magnetic response's dependence on polarization angle. It might be possible to use a CCD camera to observe any scattered light as

it propagates through the crystal in combination with detectors set up outside the crystal at the predicted angle of refraction in order to observe negative refraction, as simulated in chapter 3.

REFERENCES

- [1] V. Veselago, "The Electrodynamics of Substances with Simultaneously Negative Values of Epsilon and Mu," *Soviet Physics Uspekhi*, vol. 10, no. 4, 1968.
- [2] P. Milonni, *Fast Light, Slow Light and Left-Handed Light*. Institute of Physics Publishing, 2005.
- [3] J. Jackson, *Classical Electrodynamics*. John Wiley and Sons, Inc, 1999.
- [4] J. B. Pendry, A. J. Holden, D. J. Robbins, and W. J. Stewart, "Magnetism from Conductors and Enhanced Nonlinear Phenomena," *IEEE Transactions on Microwave Theory and Techniques*, vol. 47, no. 11, 1999.
- [5] M. O. Oktel and O. E. Müstecaplıolu, "Electromagnetically induced left-handedness in a dense gas of three-level atoms," *Physical Review A*, vol. 70, no. 5, 2004.
- [6] Q. Thommen and P. Mandel, "Electromagnetically Induced Left Handedness in Optically Excited Four-Level Atomic Media," *Physical Review Letters*, vol. 96, no. 5, 2006.
- [7] D. E. Sikes and D. D. Yavuz, "Negative refraction with low absorption using Raman transitions with magnetoelectric coupling," *Physical Review A*, vol. 82, no. 1, 2010.
- [8] D. E. Sikes and D. D. Yavuz, "Negative refraction using Raman transitions and chirality," *Physical Review A*, vol. 84, no. 5, 2011.
- [9] J. B. Pendry, "Negative Refraction Makes a Perfect Lens," *Physical Review Letters*, vol. 85, no. 18, 2000.
- [10] D. R. Smith, W. J. Padilla, D. C. Vier, S. C. Nemat-Nasser, and S. Schultz, "Composite Medium with Simultaneously Negative Permeability and Permittivity," *Physical Review Letters*, vol. 84, no. 18, 2000.
- [11] R. A. Shelby, D. R. Smith, S. C. Nemat-Nasser, and S. Schultz, "Microwave transmission through a two-dimensional, isotropic, left-handed metamaterial," *Applied Physics Letters*, vol. 78, no. 4, 2001.

- [12] A. A. Houck, J. B. Brock, and I. L. Chuang, "Experimental observations of a left-handed material that obeys Snell's law.," *Physical review letters*, vol. 90, no. 13, 2003.
- [13] S. Linden, C. Enkrich, M. Wegener, J. Zhou, T. Koschny, and C. M. Soukoulis, "Magnetic Response of Metamaterials at 100 Terahertz," *Science*, vol. 306, no. 5700, 2004.
- [14] J. Yao, Z. Liu, Y. Liu, Y. Wang, C. Sun, G. Bartal, A. M. Stacy, and X. Zhang, "Optical Negative Refraction in Bulk Metamaterials of Nanowires," *Science*, vol. 321, no. 5891, 2008.
- [15] A. Grbic and G. V. Eleftheriades, "Overcoming the Diffraction Limit with a Planar Left-Handed Transmission-Line Lens," *Physical Review Letters*, vol. 92, no. 11, 2004.
- [16] N. Fang, H. Lee, C. Sun, and X. Zhang, "SubDiffraction-Limited Optical Imaging with a Silver Superlens," *Science*, vol. 308, no. 5721, 2005.
- [17] J. B. Pendry, D. Schurig, and D. R. Smith, "Controlling Electromagnetic Fields," *Science*, vol. 312, no. 5781, 2006.
- [18] U. Leonhardt, "Optical Conformal Mapping," *Science*, vol. 312, no. 5781, 2006.
- [19] D. Schurig, J. J. Mock, B. J. Justice, S. A. Cummer, J. B. Pendry, A. F. Starr, and D. R. Smith, "Metamaterial Electromagnetic Cloak at Microwave Frequencies," *Science*, vol. 314, no. 5801, 2006.
- [20] J. Valentine, J. Li, T. Zentgraf, G. Bartal, and X. Zhang, "An optical cloak made of dielectrics," *Nature Materials*, vol. 8, no. 7, 2009.
- [21] G. Woodgate, *Elementary Atomic Structure*. Oxford University Press, 1983.
- [22] G. H. Dieke and H. M. Crosswhite, "The Spectra of the Doubly and Triply Ionized Rare Earths," *Applied Optics*, vol. 2, no. 7, 1963.
- [23] M. J. Weber and R. F. Schaufele, "Radiative and Nonradiative Transitions in the Fluorescence Decay of Eu^{3+} in SrTiO_3 ," *The Journal of Chemical Physics*, vol. 43, no. 5, 1965.
- [24] W. F. Krupke, "Optical Absorption and Fluorescence Intensities in Several Rare-Earth-Doped Y_2O_3 and LaF_3 Single Crystals," *Physical Review*, vol. 145, no. 1, 1966.
- [25] X. A. Shen and R. Kachru, "7F0 - 5D1 Transition in $\text{Eu}^{3+}:\text{Y}_2\text{SiO}_5$," *Journal of the Optical Society of America B*, vol. 11, no. 4, 1994.
- [26] A. J. Freeman and R. E. Watson, "Theoretical investigation of some magnetic and spectroscopic properties of rare-earth ions," *Physical Review*, vol. 127, no. 6, 1962.
- [27] Q. Chen, A. Troshyn, I. Ernsting, S. Kayser, S. Vasilyev, A. Nevsky, and S. Schiller, "Spectrally Narrow, Long-Term Stable Optical Frequency Reference Based on a $\text{Eu}^{3+}:\text{Y}_2\text{SiO}_5$ Crystal at Cryogenic Temperature," *Physical Review Letters*, vol. 107, no. 22, 2011.

- [28] C. W. Thiel, T. Böttger, and R. L. Cone, "Rare-earth-doped materials for applications in quantum information storage and signal processing," *Journal of Luminescence*, vol. 131, no. 3, 2011.
- [29] B. Lauritzen, N. Timoney, N. Gisin, M. Afzelius, H. de Riedmatten, Y. Sun, R. M. Macfarlane, and R. L. Cone, "Spectroscopic investigations of $\text{Eu}^{3+}:\text{Y}_2\text{SiO}_5$ for quantum memory applications," *Physical Review B*, vol. 85, no. 11, 2012.
- [30] M. Kasperczyk, S. Person, D. Ananias, L. D. Carlos, and L. Novotny, "Excitation of Magnetic Dipole Transitions at Optical Frequencies," *Physical Review Letters*, vol. 114, no. 16, 2015.
- [31] M. P. Wood and J. E. Lawler, "Aberration-corrected echelle spectrometer for measuring ultraviolet branching fractions of iron-group ions.," *Applied Optics*, vol. 51, no. 35, 2012.
- [32] M. P. Wood, *A New Echelle Spectrometer for Measuring UV Branching Fractions of FE-Group Ions*. PhD thesis, University of Wisconsin - Madison, 2014.
- [33] Z. J. Simmons, *Progress Toward a Negative Refractive Index in an Atomic System: Spectroscopy and Simulations of a Rare-Earth Doped Crystal*. PhD thesis, University of Wisconsin - Madison, 2015.
- [34] A. Ferrier, B. Tumino, and P. Goldner, "Variations in the oscillator strength of the $7F_0 \rightarrow 5D_0$ transition in $\text{Eu}^{3+}:\text{Y}_2\text{SiO}_5$ single crystals," *Journal of Luminescence*, vol. 170, 2016.
- [35] A. M. Stoneham, "Shapes of Inhomogeneously Broadened Resonance Lines in Solids," *Reviews of Modern Physics*, vol. 41, no. 1, 1969.
- [36] D. L. Orth, R. J. Mashl, and J. L. Skinner, "Optical lineshapes of impurities in crystals: a lattice model of inhomogeneous broadening by point defects," *Journal of Physics: Condensed Matter*, vol. 5, no. 16, 1993.
- [37] G. S. Ofelt, "Structure of the f_6 Configuration with Application to Rare-Earth Ions," *The Journal of Chemical Physics*, vol. 38, no. 9, 1963.
- [38] G. Dieke, *Spectra and Energy Levels of Rare Earth Ions in Crystals*. Interscience Publishers, 1968.
- [39] R. Cowan, *Theory of Atomic Structure and Spectra*. University of California Press, 1981.
- [40] R. Wybourne and K. Smentek, *Optical Spectroscopy of Lanthanides*. CRC Press, 2007.
- [41] D. D. Yavuz and N. R. Brewer, "Left-handed electromagnetic waves in materials with induced polarization and magnetization," *Physical Review A*, vol. 90, no. 6, 2014.
- [42] K. S. Yee, "Numerical Solution of Initial Boundary Value Problems Involving Maxwell's Equations in Isotropic Media," *IEEE Transactions on Antennas and Propagation*, vol. 14, no. 3, 1966.

- [43] G. Dolling, C. Enkrich, M. Wegener, C. M. Soukoulis, and S. Linden, "Simultaneous Negative Phase and Group Velocity of Light in a Metamaterial," *Science*, vol. 312, no. 5775, 2006.
- [44] R. Boyd, *Nonlinear Optics*. Elsevier, Inc, 2008.
- [45] H. Guillet de Chatellus and E. Freysz, "Measurement of the third-order susceptibility of glasses by EFISH of femtosecond pulses.," *Optics express*, vol. 9, no. 11, 2001.
- [46] K. Hakuta, L. Marmet, and B. P. Stoicheff, "Electric-Field-Induced Second-Harmonic Generation with Reduced Absorption in Atomic Hydrogen," *Physical Review Letters*, vol. 66, no. 5, 1991.
- [47] C. J. Hawthorn, K. P. Weber, and R. E. Scholten, "Littrow configuration tunable external cavity diode laser with fixed direction output beam," *Review of Scientific Instruments*, vol. 72, no. 12, 2001.
- [48] E. D. Black, "An introduction to Pound-Drever-Hall laser frequency stabilization," *American Journal of Physics*, vol. 69, no. 1, 2001.
- [49] T. W. Hansch and B. Couillaud, "Laser Frequency Stabilization by Polarization Spectroscopy of a Reflecting Reference Cavity," *Optics Communications*, vol. 35, no. 3, 1980.
- [50] M. Vainio, J. E. Bernard, and L. Marmet, "Cavity-enhanced optical frequency doubler based on transmission-mode HänschCouillaud locking," *Applied Physics B*, vol. 104, no. 4, 2011.
- [51] T. Y. Fan, C. E. Huang, B. Q. Hu, R. C. Eckardt, Y. X. Fan, R. L. Byer, and R. S. Feigelson, "Second harmonic generation and accurate index of refraction measurements in flux-grown KTiOPO_4 ," *Applied Optics*, vol. 26, no. 12, 1987.
- [52] G. D. Boyd and D. A. Kleinman, "Parametric Interaction of Focused Gaussian Light Beams," *Journal of Applied Physics*, vol. 39, no. 8, 1968.
- [53] S. C. Kumar, G. K. Samanta, and M. Ebrahim-Zadeh, "High-power, single-frequency, continuous-wave, second-harmonic-generation of ytterbium fiber laser in PPKTP and MgO:sPPLT ," *Optics Express*, vol. 17, no. 16, 2009.
- [54] F. J. Kontur, I. Dajani, Y. Lu, and R. J. Knize, "Frequency-doubling of a CW fiber laser using PPKTP, PPMgSLT, and PPMgLN," *Optics Express*, vol. 15, no. 20, 2007.
- [55] Z. Y. Ou, S. F. Pereira, E. S. Polzik, and H. J. Kimble, "85% efficiency for cw frequency doubling from 1.08 to 0.54 μm ," *Optics Letters*, vol. 17, no. 9, 1992.
- [56] R. Le Targat, J. J. Zondy, and P. Lemonde, "75%-Efficiency blue generation from an intra-cavity PPKTP frequency doubler," *Optics Communications*, vol. 247, no. 4-6, 2005.

- [57] Y. Zhang, N. Hayashi, H. Matsumori, R. Mitazaki, Y. Xue, Y. Okada-Shudo, M. Watanabe, and K. Kasai, "Generation of 1.2W green light using a resonant cavity-enhanced second-harmonic process with a periodically poled KTiOPO₄," *Optics Communications*, vol. 294, 2013.
- [58] A. Siegman, *Lasers*. University Science Books, 1986.
- [59] G. A. Massey and A. E. Siegman, "Reflection and Refraction of Gaussian Light Beams at Tilted Ellipsoidal Surfaces," *Applied Optics*, vol. 8, no. 5, 1969.
- [60] W. Yang, Y. Wang, Y. Zheng, and H. Lu, "Comparative study of the frequency-doubling performance on ring and linear cavity at short wavelength region," *Optics Express*, vol. 23, no. 15, 2015.
- [61] E. S. Polzik and H. J. Kimble, "Frequency doubling with KNbO₃ in an external cavity," *Optics Letters*, vol. 16, no. 18, 1991.
- [62] J. Miao, *Laser Cooling and Magneto-Optical Trapping of Holmium Atoms*. PhD thesis, University of Wisconsin - Madison, 2013.
- [63] M. Scully and M. Zubairy, *Quantum Optics*. Cambridge University Press, 1997.
- [64] M. Nilsson, L. Rippe, and S. Kröll, "Hole-burning techniques for isolation and study of individual hyperfine transitions in inhomogeneously broadened solids demonstrated in Pr³⁺:Y₂SiO₅," *Physical Review B*, vol. 70, no. 21, 2004.
- [65] N. B. Manson, M. J. Sellars, P. T. H. Fisk, and R. S. Meltzer, "Hole burning of rare earth ions with kHz resolution," *Journal of Luminescence*, vol. 64, no. 1-6, 1995.
- [66] D. D. Yavuz, N. R. Brewer, J. A. Miles, and Z. J. Simmons, "Suppression of inhomogeneous broadening using the ac Stark shift," *Physical Review A*, vol. 88, no. 6, 2013.
- [67] C. Cohen-Tannoudji, F. Hoffbeck, and S. Reynaud, "Compensating Doppler Broadening with Light-Shifts," *Optics Communications*, vol. 27, no. 1, 1978.
- [68] S. Reynaud, M. Himbert, J. Dupont-Roc, H. Stroke, and C. Cohen-Tannoudji, "Experimental Evidence for Compensation of Doppler Broadening by Light Shifts," *Physical Review Letters*, vol. 42, no. 12, 1979.
- [69] K. Xia, R. Kolesov, Y. Wang, P. Siyushev, R. Reuter, T. Kornher, N. Kukharchyk, A. D. Wieck, B. Villa, S. Yang, and J. Wrachtrup, "All-Optical Preparation of Coherent Dark States of a Single Rare Earth Ion Spin in a Crystal," *Physical Review Letters*, vol. 115, no. 9, 2015.
- [70] B. S. Ham, P. R. Hemmer, and M. S. Shahriar, "Efficient electromagnetically induced transparency in a rare-earth doped crystal," *Optics Communications*, vol. 144, no. 4-6, 1997.

- [71] P. Goldner, O. Guillot-Noël, F. Beaudoux, Y. Le Du, J. Lejay, T. Chanelière, J. L. Le Gouët, L. Rippe, A. Amari, A. Walther, and S. Kröll, “Long coherence lifetime and electromagnetically induced transparency in a highly-spin-concentrated solid,” *Physical Review A*, vol. 79, no. 3, 2009.
- [72] A. V. Turukhin, V. S. Sudarshanam, M. S. Shahriar, J. A. Musser, B. S. Ham, and P. R. Hemmer, “Observation of Ultraslow and Stored Light Pulses in a Solid,” *Physical Review Letters*, vol. 88, no. 2, 2001.
- [73] D. Robinson and P. Bevington, *Data Reduction and Error Analysis*. McGraw-Hill Education, 2002.
- [74] T. Okoshi, K. Kikuchi, and A. Nakayama, “Novel method for high resolution measurement of laser output spectrum,” *Electronics Letters*, vol. 16, no. 16, 1980.
- [75] D. Steck, “*Quantum and Atom Optics* available online at <http://steck.us/teaching> (revision 0.12.0, 16 may 2017).”
- [76] P. Horak and W. H. Loh, “On the delayed self-heterodyne interferometric technique for determining the linewidth of fiber lasers,” *Optics Express*, vol. 14, no. 9, 2006.
- [77] K. Kikuchi and T. Okoshi, “Dependence of semiconductor laser linewidth on measurement time: evidence of predominance of $1/f$ noise,” *Electronics Letters*, vol. 21, no. 22, 1985.

Appendix A: Second Harmonic Generation

A.1 Wave Equation

This derivation will follow the third edition of Boyd's *Nonlinear Optics* [44]. First start with Maxwell's equations assuming no free charge and no free current ($\rho = \mathbf{J} = 0$), a non-magnetic material, and that $\tilde{\mathbf{B}} = \mu_0 \tilde{\mathbf{H}}$ (the quantities with tildes over them indicate that they are rapidly oscillating):

$$\nabla \cdot \tilde{\mathbf{D}} = 0 \quad (\text{A.1})$$

$$\nabla \cdot \tilde{\mathbf{B}} = 0 \quad (\text{A.2})$$

$$\nabla \times \tilde{\mathbf{E}} = -\frac{\partial \tilde{\mathbf{B}}}{\partial t} \quad (\text{A.3})$$

$$\nabla \times \tilde{\mathbf{H}} = \frac{\partial \tilde{\mathbf{D}}}{\partial t}. \quad (\text{A.4})$$

The electric displacement $\tilde{\mathbf{D}}$ can be written as $\tilde{\mathbf{D}} = \epsilon_0 \tilde{\mathbf{E}} + \tilde{\mathbf{P}}$, where the polarization, $\tilde{\mathbf{P}}$, depends nonlinearly on the electric field. Next, equations A.3 and A.4 can be written only in terms of $\tilde{\mathbf{H}}$ and $\tilde{\mathbf{E}}$:

$$\nabla \times \tilde{\mathbf{E}} = -\mu_0 \frac{\partial \tilde{\mathbf{H}}}{\partial t} \quad (\text{A.5})$$

$$\nabla \times \tilde{\mathbf{H}} = \frac{\partial (\epsilon_0 \tilde{\mathbf{E}} + \tilde{\mathbf{P}})}{\partial t}. \quad (\text{A.6})$$

These equations can then be solved to get a wave equation for $\tilde{\mathbf{E}}$ by taking the curl of both sides of equation A.5 and using the vector identity $\nabla \times \nabla \times \mathbf{E} = \nabla(\nabla \cdot \mathbf{E}) - \nabla^2 \mathbf{E}$. The result is

$$\nabla^2 \tilde{\mathbf{E}} - \frac{1}{c} \frac{\partial^2 \tilde{\mathbf{E}}}{\partial t^2} = \frac{1}{\epsilon_0 c^2} \frac{\partial^2 \tilde{\mathbf{P}}}{\partial t^2} \quad (\text{A.7})$$

or, equivalently,

$$\nabla^2 \tilde{\mathbf{E}} - \frac{1}{\epsilon_0 c^2} \frac{\partial^2 \tilde{\mathbf{D}}}{\partial t^2} = 0. \quad (\text{A.8})$$

The electric displacement can be written as a sum of linear and nonlinear terms:

$$\tilde{\mathbf{D}} = \tilde{\mathbf{D}}^{(1)} + \tilde{\mathbf{P}}^{(\text{NL})}, \quad (\text{A.9})$$

where

$$\tilde{\mathbf{D}}^{(1)} = \epsilon_0 \tilde{\mathbf{E}} + \tilde{\mathbf{P}}^{(1)}. \quad (\text{A.10})$$

Using these definitions equation A.7 can be written

$$\nabla^2 \tilde{\mathbf{E}} - \frac{1}{\epsilon_0 c^2} \frac{\partial^2 \tilde{\mathbf{D}}^{(1)}}{\partial t^2} = \frac{1}{\epsilon_0 c^2} \frac{\partial^2 \tilde{\mathbf{P}}^{(\text{NL})}}{\partial t^2}. \quad (\text{A.11})$$

For a lossless, dispersionless medium $\tilde{\mathbf{D}}^{(1)} = \epsilon_0 \epsilon^{(1)} \cdot \tilde{\mathbf{E}}$ where $\epsilon^{(1)}$ is the dielectric tensor. If the medium is isotropic then $\epsilon^{(1)}$ turns into a scalar and equation A.11 is

$$-\nabla^2 \tilde{\mathbf{E}} + \frac{\epsilon^{(1)}}{c^2} \frac{\partial^2 \tilde{\mathbf{E}}}{\partial t^2} = -\frac{1}{\epsilon_0 c^2} \frac{\partial^2 \tilde{\mathbf{P}}^{(\text{NL})}}{\partial t^2}. \quad (\text{A.12})$$

If the right hand of equation A.12 is zero, the solutions are waves that travel at a speed $\frac{c}{n}$ where $n^2 = \epsilon^{(1)}$. When the right side is nonzero, the nonlinear polarization is a source term which generates new frequencies. In a dispersive medium, each frequency component will experience a different $\epsilon^{(1)}$ and each frequency component must be considered separately by writing each quantity as a sum:

$$\tilde{\mathbf{E}}(\mathbf{r}, t) = \sum_n \tilde{\mathbf{E}}_n(\mathbf{r}, t) \quad (\text{A.13})$$

$$\tilde{\mathbf{D}}^{(1)}(\mathbf{r}, t) = \sum_n \tilde{\mathbf{D}}_n^{(1)}(\mathbf{r}, t) \quad (\text{A.14})$$

$$\tilde{\mathbf{P}}^{(\text{NL})}(\mathbf{r}, t) = \sum_n \tilde{\mathbf{P}}_n^{(\text{NL})}(\mathbf{r}, t). \quad (\text{A.15})$$

Each component of the electric field can be written as

$$\tilde{\mathbf{E}}(\mathbf{r}, t) = \tilde{\mathbf{E}}(\mathbf{r}) e^{-i\omega_n t} + \tilde{\mathbf{E}}^*(\mathbf{r}) e^{i\omega_n t}. \quad (\text{A.16})$$

The same can be done for $\tilde{\mathbf{D}}$ and $\tilde{\mathbf{P}}$. If the medium is dissipative, $\epsilon^{(1)}$ would be complex. In order to simplify the situation, dissipation will be neglected here and the electric displacement can be written

$$\tilde{\mathbf{D}}_n^{(1)}(\mathbf{r}, t) = \epsilon_0 \epsilon^{(1)}(\mathbf{r}, t) \cdot \tilde{\mathbf{E}}_n(\mathbf{r}, t). \quad (\text{A.17})$$

A new wave equation (equation A.12) can be written for each component of the field:

$$\nabla^2 \tilde{\mathbf{E}}_n - \frac{\epsilon^{(1)}(\omega_n)}{c^2} \frac{\partial^2 \tilde{\mathbf{E}}_n}{\partial t^2} = \frac{1}{\epsilon_0 c^2} \frac{\partial^2 \tilde{\mathbf{P}}_n^{(\text{NL})}}{\partial t^2}. \quad (\text{A.18})$$

A.2 Second Harmonic Generation

Equation A.18 can now be applied to the case of second harmonic generation. For simplicity, only plane waves with only z dependence will be assumed. The laplacian, ∇^2 , in the wave equation can then be replaced by $\frac{\partial^2}{\partial z^2}$. The slowly varying envelope approximation can also be made¹. The fundamental electric field will be $\tilde{E}_1(z, t)$ and the second harmonic electric field will be $\tilde{E}_2(z, t)$, so the total electric field can be written $\tilde{E}(z, t) = \tilde{E}_1(z, t) + \tilde{E}_2(z, t)$ where

$$\tilde{E}_j(z, t) = E_j(z)e^{-i\omega_j t} + E_j^*(z)e^{i\omega_j t} \quad (\text{A.19})$$

and

$$E_j(z) = A_j(z)e^{ik_j z}, \quad (\text{A.20})$$

$$k_j = \frac{n_j \omega_j}{c}, \quad (\text{A.21})$$

$$n_j = \sqrt{\epsilon^{(1)}(\omega_j)}, \quad (\text{A.22})$$

and A_j is the amplitude of the electric field. Each frequency component of the electric field will obey the wave equation separately:

$$\frac{\partial^2 \tilde{E}_j}{\partial z^2} - \frac{\epsilon^{(1)}(\omega_j)}{c^2} \frac{\partial^2 \tilde{E}_j}{\partial t^2} = \frac{1}{\epsilon_0 c^2} \frac{\partial^2 \tilde{P}_j}{\partial t^2}, \quad (\text{A.23})$$

where

$$\tilde{P}^{(\text{NL})} = \tilde{P}_1(z, t) + \tilde{P}_2(z, t) \quad (\text{A.24})$$

and

$$\tilde{P}_j(z, t) = P_j(z)e^{-i\omega_j t} + P_j^*(z)e^{i\omega_j t}. \quad (\text{A.25})$$

The polarizations, calculated elsewhere (see [44]), are found to be

$$P_1(z) = 4\epsilon_0 d_{\text{eff}} E_2 E_1^* = 4\epsilon_0 d_{\text{eff}} A_2 A_1^* e^{i(k_2 - k_1)z}, \quad (\text{A.26})$$

$$P_2(z) = 2\epsilon_0 d_{\text{eff}} E_1^2 = 2\epsilon_0 d_{\text{eff}} A_1^2 e^{2ik_1 z}. \quad (\text{A.27})$$

¹The slowly varying envelope approximation is valid when $\left| \frac{\partial^2 A_i}{\partial z^2} \right| \ll k_i \left| \frac{\partial A_i}{\partial z} \right|$

For second harmonic generation $\omega_2 = 2\omega_1$. Equation A.23 can first be solved by using only the ω_1 frequency components of \tilde{E} and \tilde{P} :

$$\tilde{E}_1(z, t) = A_1(z)e^{i(k_1 z - \omega_1 t)} + A_1^*(z)e^{-i(k_1 z - \omega_1 t)}, \quad (\text{A.28})$$

$$\tilde{P}_1(z, t) = 4\epsilon_0 d_{\text{eff}} A_2 A_1^* e^{i((k_2 - k_1)z - \omega_1 t)} + 4\epsilon_0 d_{\text{eff}} A_2^* A_1 e^{-i((k_2 - k_1)z - \omega_1 t)}, \quad (\text{A.29})$$

and then again by using the only the ω_2 components of \tilde{E} and \tilde{P} :

$$\tilde{E}_2(z, t) = A_2(z)e^{i(k_2 z - \omega_2 t)} + A_2^*(z)e^{-i(k_2 z - \omega_2 t)}, \quad (\text{A.30})$$

$$\tilde{P}_2(z, t) = 2\epsilon_0 d_{\text{eff}} A_1^2 e^{i(2k_1 z - \omega_2 t)} + 2\epsilon_0 d_{\text{eff}} A_1^2 e^{-i(2k_1 z - \omega_2 t)}. \quad (\text{A.31})$$

The details of the math are not shown here, but after making the approximations listed at the beginning of the section the following ‘coupled amplitude equations’ are found:

$$\frac{dA_1}{dz} = \frac{2i\omega_1^2 d_{\text{eff}}}{k_1 c^2} A_2 A_1^* e^{-i\Delta k z}, \quad (\text{A.32})$$

$$\frac{dA_2}{dz} = \frac{i\omega_2^2 d_{\text{eff}}}{k_2 c^2} A_1^2 e^{i\Delta k z}, \quad (\text{A.33})$$

where the wave vector mismatch is

$$\Delta k = 2k_1 - k_2. \quad (\text{A.34})$$

Appendix B: Error Analysis

B.1 Error Bars on f vs I plot

A good reference for the error analysis described here is reference [73]. If f is a function of x , y , and z , the uncertainty in f can be calculated from

$$\Delta f = \sqrt{\left(\frac{\partial f}{\partial x} \Delta x\right)^2 + \left(\frac{\partial f}{\partial y} \Delta y\right)^2 + \left(\frac{\partial f}{\partial z} \Delta z\right)^2} \quad (\text{B.1})$$

where Δx , Δy , and Δz are either the uncertainty of the measure made or are themselves calculated from an equation analogous to equation B.1.

In the case of the square root plot in figure 5.3, the actual measurements were the time of peak transmission of the Rabi curve, and the power of the beam based off of a calibrated photodiode. Each frequency was calculated using

$$f = \frac{1}{2t_{\text{peak}}}, \quad (\text{B.2})$$

where t_{peak} is the time where the first maximum transmission occurs in a Rabi cycle. The vertical error bars are given by the uncertainty in the frequency which is calculated from

$$\Delta f = \sqrt{\left(\frac{\partial f}{\partial t_{\text{peak}}} \Delta t_{\text{peak}}\right)^2} \quad (\text{B.3})$$

$$\Delta f = \sqrt{\left(\frac{-1}{2t_{\text{peak}}^2} \Delta t_{\text{peak}}\right)^2} \quad (\text{B.4})$$

$$\Delta f = \frac{\Delta t_{\text{peak}}}{2t_{\text{peak}}^2}, \quad (\text{B.5})$$

where the uncertainty in the peak time, Δt_{peak} was determined by my discretion due to the fact that there is no analytic formula to fit the Rabi curve to and the fact that there was only one Rabi curve for a given laser power.

The intensity, I , of the beam was calculated using

$$I = \frac{2P}{\pi w_0^2}, \quad (\text{B.6})$$

where P is the power of the beam and w_0 is beam waist. The uncertainty in I , and therefore the horizontal error bars, can be calculated from

$$\Delta I = \sqrt{\left(\frac{\partial I}{\partial P} \Delta P\right)^2 + \left(\frac{\partial I}{\partial w_0} \Delta w_0\right)^2}, \quad (\text{B.7})$$

where

$$\frac{\partial I}{\partial P} = \frac{2}{\pi w_0^2} = \frac{I}{P}, \quad (\text{B.8})$$

$$\frac{\partial I}{\partial w_0} = -\frac{4P}{\pi w_0^3} = -\frac{2I}{w_0}. \quad (\text{B.9})$$

Equation B.7 can be written as

$$\Delta I = I \sqrt{\left(\frac{\Delta P}{P}\right)^2 + \left(\frac{2\Delta w_0}{w_0}\right)^2}, \quad (\text{B.10})$$

where ΔP is determined by the error in the slope of the power vs voltage fit of the photodiode (figure B.1) and Δw_0 is $1 \mu\text{m}$ as given by the beam profiler's specs. The uncertainty of the slope, m , of a linear best fit line is calculated using

$$\Delta m = \sqrt{\frac{\sum (y_i - y)^2}{(N - 2) \sum (x_i - \bar{x})^2}}, \quad (\text{B.11})$$

where y_i is the measured value of the dependent variable, y is the calculated value based on the fitting parameters, x_i is the measured value of the independent variable, \bar{x} is the mean of all measured x_i values, and N is the total number of data points. The photodiode calibration data is shown in figure B.1 with a best fit line. Using a least squares fit and equation B.11, the conversion from photodiode voltage to optical power was found to be

$$m = (0.1401 \pm 0.0011) \frac{\text{W}}{\text{V}}. \quad (\text{B.12})$$

In previous experiments it was determined that the photodiodes signal was linear over many orders of magnitude of optical power. Because of this, we are confident that this calibration is still valid for optical powers of 100s of mWs.

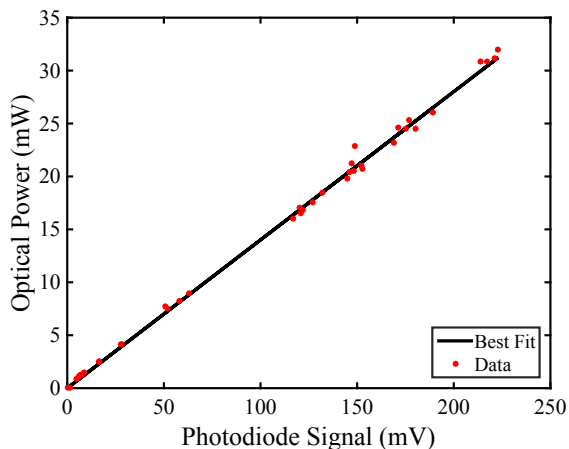


Figure B.1: *Photodiode Calibration Plot.*

B.2 Uncertainty in Magnetic Dipole Moment

The Rabi frequency is related to intensity through equation 5.5, repeated here for convenience:

$$f = \frac{\mu}{2\pi\hbar} \sqrt{\frac{2n\mu_0 I}{c}}. \quad (\text{B.13})$$

In order to get a value for μ , the dipole moment, a least squares fit was made to an f vs $\frac{1}{2\pi\hbar} \sqrt{\frac{2n\mu_0 I}{c}}$ plot, shown in figure B.2. This greatly simplifies finding the uncertainty of the dipole moment,

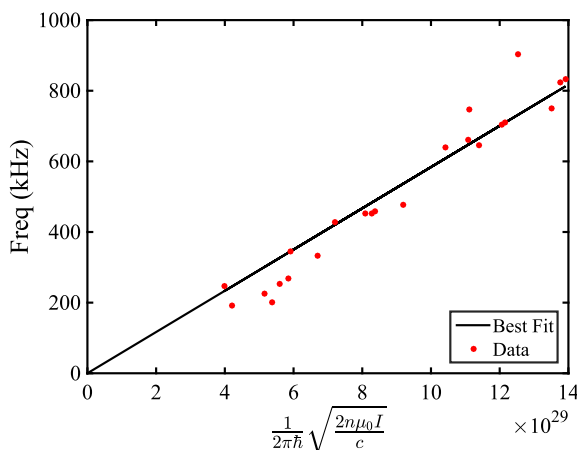


Figure B.2: *Linearized Data.* The slope of this plot is the dipole moment of the transition.

because it is now just the slope of this graph. Again, using a least-squares fit and equation B.11,

the value of the dipole moment is found to be

$$\mu = (0.063 \pm 0.005)\mu_{\text{B}} . \tag{B.14}$$

Appendix C: Numerically solving differential equations using a 4th order Runge-Kutta Method

The 4th order Runge-Kutta method outlined here was used to simulate left-handed waves created by external polarization and magnetization (chapter 3), second harmonic generation in a non-linear crystal (chapter 4), and many atomic systems, including the 7-level system to simulate our Rabi flopping result (chapter 5) and the 4 level system to study inhomogeneous linewidth suppression (chapter 6).

C.1 Runge-Kutta method

In general the Runge-Kutta method can solve N coupled first order differential equations in the form:

$$\begin{aligned} \dot{a}_1 &= F_1(t, a_1, a_2, \dots, a_N), \\ \dot{a}_2 &= F_2(t, a_1, a_2, \dots, a_N), \\ &\vdots \\ \dot{a}_N &= F_N(t, a_1, a_2, \dots, a_N). \end{aligned} \tag{C.1}$$

The goal is to solve these equations for $a_1(t)$, $a_2(t)$, \dots , $a_N(t)$. In order to generate the $a(t)$ functions, the following equations are used:

$$\begin{aligned} a_1^{(n+1)} &= a_1^n + \frac{K_{11} + 2K_{12} + 2K_{13} + K_{14}}{6}, \\ a_2^{(n+1)} &= a_2^n + \frac{K_{21} + 2K_{22} + 2K_{23} + K_{24}}{6}, \\ &\vdots \\ a_N^{(n+1)} &= a_N^n + \frac{K_{N1} + 2K_{N2} + 2K_{N3} + K_{N4}}{6}. \end{aligned} \tag{C.2}$$

The first subscript on a K matches the subscript on the a equation it is associated with, and the second subscript runs from 1 to 4 because it is a 4th order Runge-Kutta method. The K coefficients are calculated from

$$\begin{aligned}
K_{11} &= h \cdot F_1(t, a_1^n, a_2^n, \dots, a_N^n), \\
K_{21} &= h \cdot F_2(t, a_1^n, a_2^n, \dots, a_N^n), \\
&\vdots \\
K_{N1} &= h \cdot F_N(t, a_1^n, a_2^n, \dots, a_N^n),
\end{aligned} \tag{C.3}$$

$$\begin{aligned}
K_{12} &= h \cdot F_1\left(t + \frac{h}{2}, a_1^n + \frac{K_{11}}{2}, a_2^n + \frac{K_{21}}{2}, \dots, a_N^n + \frac{K_{N1}}{2}\right), \\
K_{22} &= h \cdot F_2\left(t + \frac{h}{2}, a_1^n + \frac{K_{11}}{2}, a_2^n + \frac{K_{21}}{2}, \dots, a_N^n + \frac{K_{N1}}{2}\right), \\
&\vdots \\
K_{N2} &= h \cdot F_N\left(t + \frac{h}{2}, a_1^n + \frac{K_{11}}{2}, a_2^n + \frac{K_{21}}{2}, \dots, a_N^n + \frac{K_{N1}}{2}\right),
\end{aligned} \tag{C.4}$$

$$\begin{aligned}
K_{13} &= h \cdot F_1\left(t + \frac{h}{2}, a_1^n + \frac{K_{12}}{2}, a_2^n + \frac{K_{22}}{2}, \dots, a_N^n + \frac{K_{N2}}{2}\right), \\
K_{23} &= h \cdot F_2\left(t + \frac{h}{2}, a_1^n + \frac{K_{12}}{2}, a_2^n + \frac{K_{22}}{2}, \dots, a_N^n + \frac{K_{N2}}{2}\right), \\
&\vdots \\
K_{N3} &= h \cdot F_N\left(t + \frac{h}{2}, a_1^n + \frac{K_{12}}{2}, a_2^n + \frac{K_{22}}{2}, \dots, a_N^n + \frac{K_{N2}}{2}\right),
\end{aligned} \tag{C.5}$$

$$\begin{aligned}
K_{14} &= h \cdot F_1(t + h, a_1^n + K_{13}, a_2^n + K_{23}, \dots, a_N^n + K_{N3}), \\
K_{24} &= h \cdot F_2(t + h, a_1^n + K_{13}, a_2^n + K_{23}, \dots, a_N^n + K_{N3}), \\
&\vdots \\
K_{N4} &= h \cdot F_N(t + h, a_1^n + K_{13}, a_2^n + K_{23}, \dots, a_N^n + K_{N3}),
\end{aligned} \tag{C.6}$$

where h is the time step size. Once all these K 's are known, they can be plugged into equation (C.2) to find the next step in $a(t)$. The K_{ij} notation is kind of confusing to look at, but writing it this way helps to convert everything to matrices. By writing everything in terms of matrices, it makes it easier to adapt this method to Matlab code.

For N_t time steps a matrix a can be written that has N rows and N_t columns. A column n can be calculated using (C.2):

$$a_n = \begin{bmatrix} a_1^n \\ a_2^n \\ \vdots \\ a_N^n \end{bmatrix}, \quad a_{n+1} = \begin{bmatrix} a_1^n + \frac{K_{11}+2K_{12}+2K_{13}+K_{14}}{6} \\ a_2^n + \frac{K_{21}+2K_{22}+2K_{23}+K_{24}}{6} \\ \vdots \\ a_N^n + \frac{K_{N1}+2K_{N2}+2K_{N3}+K_{N4}}{6} \end{bmatrix}. \quad (\text{C.7})$$

The rate equations (C.1) can also be written in a matrix form:

$$\begin{bmatrix} \dot{a}_1 \\ \dot{a}_2 \\ \vdots \\ \dot{a}_N \end{bmatrix} = \mathbf{F} \begin{bmatrix} t \\ a_1 \\ a_2 \\ \vdots \\ a_N \end{bmatrix}, \quad (\text{C.8})$$

where \mathbf{F} is a N by $N + 1$ matrix of coefficients of the variables t, a_1, a_2 , etc. For example, when solving the EIT problem using population rate equations (as opposed to using the density matrix), the matrix form of the rate equations would be

$$\begin{bmatrix} \dot{a}_1 \\ \dot{a}_2 \\ \dot{a}_3 \end{bmatrix} = \underbrace{\begin{bmatrix} 0 & 0 & 0 & i\frac{\Omega_p}{2} \\ 0 & 0 & -i\delta\omega & i\frac{\Omega_c}{2} \\ 0 & i\frac{\Omega_p}{2} & i\frac{\Omega_c}{2} & -(i\delta\omega + \frac{\Gamma}{2}) \end{bmatrix}}_{\text{F Matrix}} \begin{bmatrix} t \\ a_1 \\ a_2 \\ a_3 \end{bmatrix}. \quad (\text{C.9})$$

Using this \mathbf{F} matrix, for one step in time, each \mathbf{K} can be written out as follows:

$$\begin{aligned}
 K_{i1} = h \cdot F_i \begin{bmatrix} t \\ a_1 \\ a_2 \\ \vdots \\ a_N \end{bmatrix}, \quad K_{i2} = h \cdot F_i \begin{bmatrix} t + \frac{h}{2} \\ a_1 + \frac{K_{1,1}}{2} \\ a_2 + \frac{K_{2,1}}{2} \\ \vdots \\ a_N + \frac{K_{N,1}}{2} \end{bmatrix}, \\
 K_{i3} = h \cdot F_i \begin{bmatrix} t + \frac{h}{2} \\ a_1 + \frac{K_{1,2}}{2} \\ a_2 + \frac{K_{2,2}}{2} \\ \vdots \\ a_N + \frac{K_{N,2}}{2} \end{bmatrix}, \quad K_{i4} = h \cdot F_i \begin{bmatrix} t + h \\ a_1 + K_{1,3} \\ a_2 + K_{2,3} \\ \vdots \\ a_N + K_{N,3} \end{bmatrix}, \quad (\text{C.10})
 \end{aligned}$$

where i runs from 1 to N and F_i is the i^{th} row of the matrix \mathbf{F} . After all the K 's are found from cycling through all values of i , equation (C.2) can be used to find the a_{n+1} column of the a -matrix. After advancing through all N_t time steps, the rows of the a -matrix are the functions $a_1(t)$, $a_2(t)$, \dots , $a_N(t)$.

C.2 Solving the density matrix

A useful problem to solve using this Runge-Kutta method is the density matrix equation of motion:

$$\dot{\rho} = \frac{1}{i\hbar} [\hat{H}, \hat{\rho}] - \frac{1}{2} \{ \hat{\Gamma}, \hat{\rho} \}. \quad (\text{C.11})$$

The equation of motion for the ij component of the density matrix more explicitly written out is

$$\dot{\rho}_{ij} = \frac{1}{i\hbar} \sum_k (H_{ik} \rho_{kj} - \rho_{ik} H_{kj}) - \frac{1}{2} \sum_k (\Gamma_{ik} \rho_{kj} + \rho_{ik} \Gamma_{kj}), \quad (\text{C.12})$$

where i , j , and k run from 1 to N (the number of levels). From this equation it can be seen that there are N^2 equations to solve. The Runge-Kutta method above can be used, but finding a matrix \mathbf{F} needs to be done carefully.

First define the a vector from equation (C.7) with the components in increasing $ijth$ order. For example, the n^{th} column of the three level problem would be

$$a_n = \left[\rho_{11} \quad \rho_{12} \quad \rho_{13} \quad \rho_{21} \quad \rho_{22} \quad \rho_{23} \quad \rho_{31} \quad \rho_{32} \quad \rho_{33} \right]^T. \quad (\text{C.13})$$

In general:

$$a_n = \left[\rho_{11} \quad \rho_{12} \quad \cdots \quad \rho_{1N} \quad \rho_{21} \quad \rho_{22} \quad \cdots \quad \rho_{2N} \quad \cdots \quad \rho_{N1} \quad \rho_{N2} \quad \cdots \quad \rho_{NN} \right]^T. \quad (\text{C.14})$$

Each row of \mathbf{F} corresponds to a rate equation, so using equation (C.12), the coefficient of each ρ_{ij} can be found for every equation $\dot{\rho}_{ij}$ and a matrix \mathbf{F} can be constructed. To do this using Matlab, the following procedure can be used. First gather like terms of ρ in the rate equation (the sum over k is assumed):

$$\dot{\rho}_{ij} = \left(\frac{1}{i\hbar} H_{ik} - \frac{1}{2} \Gamma_{ik} \right) \rho_{kj} + \left(-\frac{1}{i\hbar} H_{kj} - \frac{1}{2} \Gamma_{kj} \right) \rho_{ik}. \quad (\text{C.15})$$

Now an $N \times N$ matrix, \mathbf{p} , can be calculated for each value of ij by cycling through values of k :

$$\begin{aligned} p_{kj} &= \left(\frac{1}{i\hbar} H_{ik} - \frac{1}{2} \Gamma_{ik} \right), \\ p_{ik} &= \left(-\frac{1}{i\hbar} H_{kj} - \frac{1}{2} \Gamma_{kj} \right). \end{aligned} \quad (\text{C.16})$$

Once \mathbf{p} is found, it can be reshaped into a $1 \times N^2$ matrix by transposing it and using Matlab's 'reshape' function. The three level problem should look like this

$$\left[t \quad p_{11} \quad p_{12} \quad p_{13} \quad p_{21} \quad p_{22} \quad p_{23} \quad p_{31} \quad p_{32} \quad p_{33} \right]. \quad (\text{C.17})$$

It can then be put into the corresponding row of the \mathbf{F} matrix. The t is put in for generality in the case of the rate equations having explicit t dependence.

Appendix D: Self-Heterodyne Method for Determining Laser Linewidth

The linewidth of the laser is a useful thing to know for several reasons. For example, it is good to know how wide the laser linewidth is compared to any atomic transitions involved in a given experiment. Also, the amount of light that can be coupled into a cavity is dependent on the laser linewidth. Lastly, if the characteristics of the laser linewidth are known, monitoring the linewidth can help troubleshoot problems, such as if the laser diode goes bad. A relatively easy way to measure the linewidth of a laser is using the so-called self-heterodyne measurement [74]. A diagram of the setup is shown and described in figure D.1.

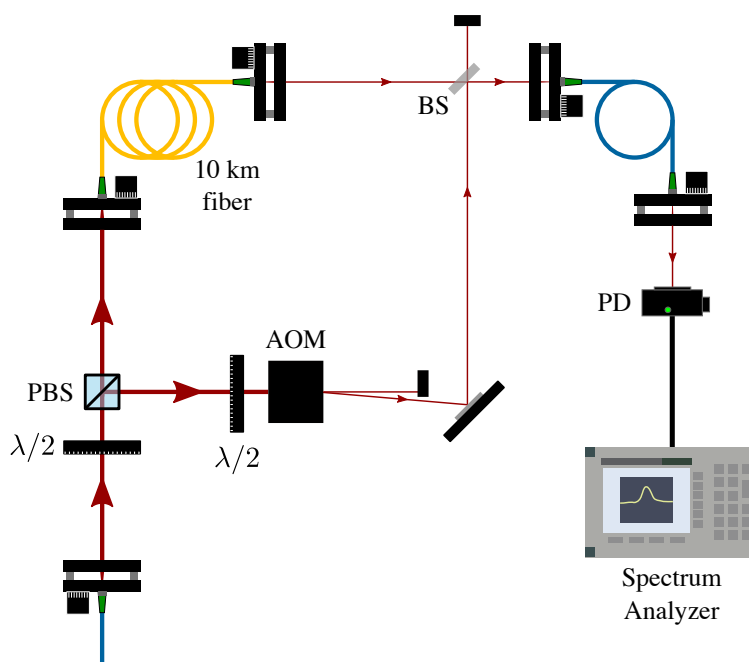


Figure D.1: *Self-Heterodyne Interferometer*. A laser is first split with a polarizing beam splitter (PBS). One path is sent into a 10 km long fiber and the other path is sent through an acousto-optic modulator (AOM) and that shifts the frequency. The paths are then recombined on a non-polarizing beamsplitter, coupled into a fiber, and shined on a photodiode. The photodiode signal is observed on a spectrum analyzer.

The basic idea is that the laser is beat against an uncorrelated version of itself. The light coming out of the laser can be thought of as a sine wave with a varying frequency. If the two legs of the interferometer were exactly equal, there would be a delta function-like peak at 110 MHz (the frequency the AOM operates at) on the spectrum analyzer. One leg, however, travels through the 10 km fiber and is delayed by a time t_{delay} compared to the the AOM leg. By the time the light that entered the fiber gets to the photodiode, the laser frequency has fluctuated so that a signal corresponding to the 110 MHz AOM shift plus the frequency fluctuation that occurred within the delay time will be registered on the spectrum analyzer. A more mathematical description of self-heterodyne detection can be found in references [75], [76], and [77].

In order to get the linewidth, the output of the spectrum analyzer first needs to be linearized using

$$P_{\text{Watts}} = 1 \text{ W} \cdot 10^{\frac{P_{\text{dBm}}}{10}} . \quad (\text{D.1})$$

Next a gaussian is fit to the linearized data. Only the center of the peak is gaussian, however, as is most obvious by looking at the spectrum analyzer output in dBm. On a log scale, a gaussian turns into an inverted parabola, and on the spectrum analyzer output, shown in figure D.2a, the signal begins to deviate from an inverted parabola around 0.25 MHz away from the center frequency of 110 MHz. This frequency range can then be used as an estimate of which section of the linearized data should be fit to a gaussian.

A laser's 'linewidth' is a halfway ambiguous measurement because it depends on the timescale on which the measurement takes place. For example, this measurement is sort of an 'instantaneous' linewidth that takes place in the amount of time it takes the spectrum analyzer to take a scan. In this case, the FWHM of the laser spectrum will be half as wide as the FWHM of the spectrum analyzer signal if the spectrum is lorentzian and a factor of $\sqrt{2}$ narrower if the spectrum is gaussian [74]. The actual spectrum is somewhere between these two values and any linewidth we quote is simply the FWHM of the gaussian section of spectrum analyzer's output, as described above. It could be the case that over the course of minutes or hours the center frequency drifts. This slower drift is not accounted for in this self-heterodyne technique, but can be monitored with a wavemeter. The

ULE cavity that the laser is locked to narrows the linewidth but also minimizes any slow frequency drifts that might occur.

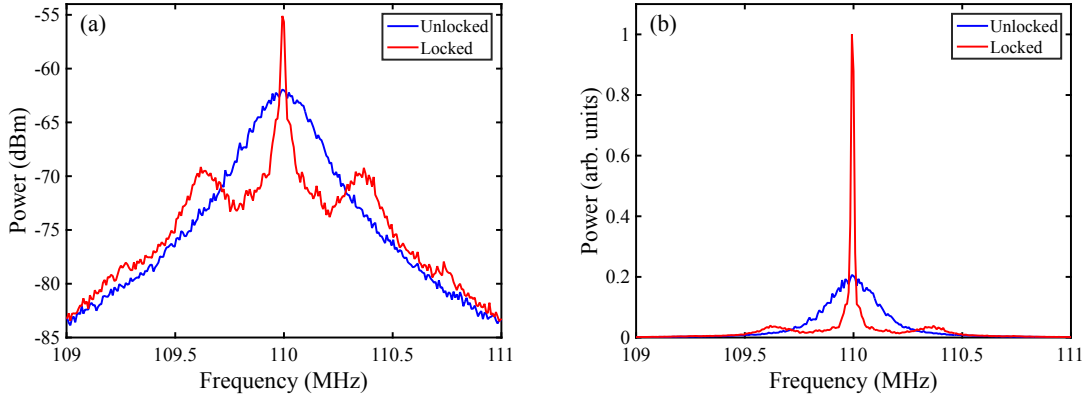


Figure D.2: *Linewidth Measurements.* (a) The output of the spectrum analyzer for both the unlocked and locked laser. (b) The normalized and linearized signals. The FWHMs of the unlocked and locked lasers are ~ 260 kHz and ~ 17 kHz, respectively.

In order to accurately measure the laser's linewidth, the delay time, t_{delay} , introduced by the 10 km fiber needs to be longer than the coherence length of the laser. The delay time the fiber introduces is

$$t_{\text{delay}} = \frac{nx}{c}, \quad (\text{D.2})$$

where n is the index of refraction of the fiber, x is the length of the fiber, and c is the speed of light. For $n = 1.447$ and $x = 10$ km, the delay time is $48.3 \mu\text{s}$. This means that linewidths narrower than $1/(48.3 \mu\text{s}) = 20.7$ kHz cannot be accurately measured. Figure D.2 shows the raw and linearized data from the spectrum analyzer while the laser is PDH locked to the ULE cavity and while it is unlocked. The unlocked laser's linewidth is 260 kHz which is certainly wide enough to be accurately measured. Once the laser is locked however, the linewidth is measured to be 17 kHz and side lobes appear on the signal, perhaps indicating it has a linewidth narrower than the interferometer can accurately measure.